
Adsorption of organic molecules on solid surfaces

A scanning tunneling microscopy study

Wei Xu

**Interdisciplinary Nanoscience Center (iNANO) and
Department of Physics and Astronomy
University of Aarhus, Denmark**

PhD thesis

May 2008

This thesis has been submitted to the Faculty of Science at the University of Aarhus in order to fulfill the requirements for obtaining a PhD degree in physics and nanoscience. The work has been carried out under the supervision of Professor Flemming Besenbacher at the Interdisciplinary Nanoscience Center (iNANO) and the Department of Physics and Astronomy from May 2004 to May 2008.

Contents

List of publications

1	Introduction	1
1.1	Motivation	2
1.2	Background review	3
1.3	Outline of the thesis	6
2	Experimental setup and DFT basics	9
2.1	Scanning tunneling microscopy	10
2.2	Density functional theory	12
2.3	Experimental methods	13
3	DNA bases and derivatives on Au(111)	15
3.1	Adenine on Au(111)	16
3.2	Thymine on Au(111)	23
3.3	Guanine on Au(111)	29
3.4	Cytosine on Au(111)	34
3.5	Cytosine+Guanine and Cytosine+Adenine on Au(111)	41
3.6	Guanine and K^+ on Au(111)	48
3.7	DNA base derivatives on Au(111)	53
4	Rosette assembly and its building blocks on Au(111)	59
4.1	The rosette system	60
4.2	CYA, DEB, BuCYA on Au(111)	61
4.3	Coadsorption of CYA and M on Au(111)	66
4.4	SV-21 and its derivative on Au(111)	73
4.5	Rosette assembly SV-22 on Au(111)	77
5	Molecular mould on Au(111) and Cu(110)	79
5.1	Aim of the project	80
5.2	DAT on Cu(110) and Au(111)	80
5.3	Lander A (with/without diaminopyridine functional groups) on Au(111)	84
5.4	Lander A caged by Ni-PTCDI matrix on Au(111)	87

6	NDCA on Ag(110)	91
6.1	Introduction	92
6.2	Results and discussion	92
6.3	Conclusion	96
7	Iridium(III) phosphorescent emitter on partly oxidized Cu(110)	97
7.1	Introduction	98
7.2	Results and discussion	98
7.3	Conclusion	101
8	H on HOPG	103
8.1	H dimer on graphite(0001) surface	104
8.2	Clustering of H atoms on graphite(0001) surface	110
8.3	H trimer on graphite(0001) surface	116
9	Summary and outlook	121
	Bibliography	125
	Acknowledgements	

List of publications

Papers included in the thesis

- [I] *Metastable structures and recombination pathways for atomic hydrogen on the graphite (0001) surface revealed by scanning tunneling microscopy*
L. Hornekær, Z. Sljivancanin, **W. Xu**, R. Otero, E. Rauls, I. Steensgaard, E. Lægsgaard, B. Hammer, F. Besenbacher, **Phys. Rev. Lett.** 96, 156104 (2006).
- [II] *Clustering of chemisorbed D atoms on the graphite (0001) surface due to preferential sticking*
L. Hornekær, E. Rauls, **W. Xu**, Z. Sljivancanin, R. Otero, T. Zecho, I. Steensgaard, E. Lægsgaard, B. Hammer, F. Besenbacher, **Phys. Rev. Lett.** 97, 186102 (2006).
- [III] *Dissociation of Iridium(III) phosphorescent emitters upon adsorption on Cu(110) revealed by scanning tunneling microscopy*
H. Gersen, R. Schaub, **W. Xu**, Md. K. Nazeeruddin, M. Graetzel, I. Stensgaard, E. Lægsgaard, T. R. Linderoth, F. Besenbacher, **Appl. Phys. Lett.** 89, 264102 (2006).
- [IV] *Cyanuric acid and melamine on Au(111): structure and energetics of hydrogen bonded networks*
W. Xu, M. Dong, H. Gersen, E. Rauls, S. Vazquez-Campos, M. Crego-Calama, D. N. Reinhoudt, I. Steensgaard, E. Lægsgaard, T. R. Linderoth, F. Besenbacher, **Small** 3, 858 (2007).
- [V] *Enhanced stability of large molecules vacuum-sublimated onto Au(111) achieved by incorporation of coordinated Au-atoms*
W. Xu, M. Dong, S. Vázquez-Campos, H. Gersen, E. Lægsgaard, I. Stensgaard, M. Crego-Calama, D. N. Reinhoudt, T. R. Linderoth, F. Besenbacher, **J. Am. Chem. Soc.** 129, 10624 (2007).
- [VI] *Self-organization of gold-containing hydrogen bonded rosette assemblies on graphite surface*
S. Vazquez-Campos, M. Peter, M. Dong, S. Xu, **W. Xu**, H. Gersen, H. Schoenherr, F. Besenbacher, M. Crego-Calama, D. N. Reinhoudt, **Langmuir** 23, 10294 (2007).

- [VII] *Long range orientation of metastable atomic hydrogen adsorbate clusters on the graphite(0001) surface*
L. Hornekaer, **W. Xu**, R. Otero, T. Zecho, I. Stensgaard, E. Lægsgaard, F. Besenbacher, **Chem. Phys. Lett.** 446, 237 (2007).
- [VIII] *Probing the hierarchy of Thymine-Thymine interactions in self-assembled structures by manipulation with scanning tunneling microscopy*
W. Xu, R. E. A. Kelly, R. Otero, M. Schöck, E. Lægsgaard, I. Stensgaard, L. N. Kantorovich, F. Besenbacher, **Small** 3, 2011 (2007).
(Highlighted in Materials Views 2008, Jan, A1-A8).
- [IX] *Extended one-dimensional supramolecular assembly on a stepped surface*
J. Schnadt, E. Rauls, **W. Xu**, R. T. Vang, J. Knudsen, E. Lægsgaard, Z. Li, B. Hammer, F. Besenbacher, **Phys. Rev. Lett.** 100, 046103 (2008).
(Selected for Virtual Journal of Nanoscale Science & Technology -- Feb 11, 2008).
- [X] *Elementary structural motifs in a random network of cytosine adsorbed on a gold(111) surface*
R. Otero, M. Schöck, R. E. A. Kelly, **W. Xu**, E. Lægsgaard, I. Stensgaard, L. N. Kantorovich, F. Besenbacher, **Science** 319, 312 (2008).
(Published online 13 Dec 2007 in Science Express Reports).
- [XI] *An investigation into the interactions between self-assembled adenine molecules and the Au(111) surface*
R. E. A. Kelly, **W. Xu**, M. Lukas, R. Otero, M. Mura, Y. Lee, E. Lægsgaard, I. Stensgaard, L. N. Kantorovich, F. Besenbacher, **Small**, Accepted, 2008.
- [XII] *Comparative UHV-STM study of the influence of alkyl side-chains on hydrogen bonded molecular surface nanostructures*
W. Xu, M. Dong, H. Gersen, E. Rauls, S. Vázquez-Campos, M. Crego-Calama, D. N. Reinhoudt, I. Stensgaard, E. Lægsgaard, T. R. Linderoth, F. Besenbacher, **Small**, Accepted, 2008.
- [XIII] *Specificity of Watson-Crick base pairing on a solid surface studied at the atomic scale*
R. Otero*, **W. Xu***, M. Lukas*, R. E. A. Kelly*, E. Lægsgaard, I. Stensgaard, J. Kjems, L. N. Kantorovich, F. Besenbacher, Submitted to **Nature**, 2008 (*authors contribute equally)
- [XIV] *Understanding the disorder of the DNA base cytosine on the Au(111) surface*
R. E. A. Kelly, M. Lukas, L. N. Kantorovich, R. Otero, **W. Xu**, M. Mura, E. Lægsgaard, I. Stensgaard, F. Besenbacher, Submitted to **J. Chem. Phys.**, 2008
- [XV] *Self-organization of gold-functionalized rosette complex on Au(111) surface studied by UHV-STM*
W. Xu, M. Dong, H. Gersen, S. Vázquez-Campos, E. Lægsgaard, I. Stensgaard, M. Crego-Calama, D. N. Reinhoudt, T. R. Linderoth, F. Besenbacher,
In manuscript.

- [XVI] *Prochiral guanine on Au(111): a dual-state entropically stabilized network*
W. Xu, R. E. A. Kelly, L. N. Kantorovich, H. Gersen, E. Lægsgaard, I. Stensgaard, F. Besenbacher, In manuscript.
- [XVII] *Size-controllable G-quartet-based nanoporous networks stabilized by both hydrogen bond and metal-ligand coordination via K*
W. Xu, M. Yu, R. Otero, E. Lægsgaard, I. Stensgaard, T. R. Linderoth, F. Besenbacher, In manuscript.
- [XVIII] *Novel rosette motifs formed by cyanuric acid and melamine on Au(111)*
W. Xu, M. Dong, H. Gersen, I. Steensgaard, E. Lægsgaard, T. R. Linderoth, F. Besenbacher, In manuscript.
- [XIX] *Probing the interactions between single Lander-type molecule and metal substrates by STM manipulation*
M. Yu*, **W. Xu***, Y. B. Jalal, E. Laegsgaard, I. Stensgaard, X. Bouju, A. Gourdon, C. Joachim, F. Besenbacher, T. R. Linderoth, In manuscript (*authors contribute equally).
- [XX] *Comparative UHV-STM studies of DNA bases and their derivatives on Au(111)*
W. Xu, M. F. Jacobsen, M. Yu, E. Laegsgaard, T. R. Linderoth, K. V. Gothelf, F. Besenbacher, In preparation.
- [XXI] *Supramolecular honeycomb network formed by coadsorption of modified guanine and cytosine molecules*
W. Xu, M. F. Jacobsen, M. Yu, E. Laegsgaard, T. R. Linderoth, K. V. Gothelf, F. Besenbacher, In preparation.
- [XXII] *Lander molecule caged and aligned by Ni-PTCDI metallosupramolecular matrix*
M. Yu, **W. Xu**, N. Kalashnyk, F. Masini, E. Laegsgaard, I. Stensgaard, X. Bouju, A. Gourdon, C. Joachim, F. Besenbacher, T. R. Linderoth, In preparation.
- [XXIII] *Supramolecular networks formed by Lander-type molecular moulds*
M. Yu, **W. Xu**, N. Kalashnyk, E. Laegsgaard, I. Stensgaard, X. Bouju, A. Gourdon, C. Joachim, F. Besenbacher, T. R. Linderoth, In preparation.

CHAPTER 1

Introduction

The aim of this introductory chapter is to motivate the work presented in this thesis. It includes a general introduction to the field and short review of the literature on adsorption of organic molecules at surfaces investigated by scanning tunneling microscopy. A brief outline of the topics studied in this thesis is given in the end.

1.1 Motivation

One of the ultimate goals of the rapidly developing field of nanotechnology is to engineer functionalized structures or even devices on surfaces in a controlled manner [1]. To do so two approaches are considered; the so-called ‘top down’ and ‘bottom up’ approaches (cf. Fig. 1.1). Within the former one, techniques such as advanced lithography by UV, X-ray radiation, and electron-beam writing allow creation of features in the sub-100 nm range, which are used for the production of computer chips, photonic crystals, etc. The major disadvantage is that the cost of production facilities scales exponentially with each shrinking step. As a result, developing ‘bottom up’ fabrication methods with their intrinsic self-directed growth would be a tremendous advantage [2]. Beyond this, it may be possible to gain functionality in the process [3].

The basic principle of the ‘bottom-up’ approach is to steer the assembly of atoms and molecules into desired structures on surfaces. Extensive knowledge on how to create desired nanostructures in supramolecular chemistry through self-assembly exists. This involves spontaneous association of supramolecular structures from molecular building blocks by non-covalent interactions (mainly hydrogen bonds, H-bonds) in solution [4]. However, this knowledge cannot directly be translated to guide the assembly of adsorbates on solid surfaces, since the understanding of the interactions of adsorbates with solid surfaces remains limited. Steric hindrance will play a crucial role in determining different surface molecular conformations when molecules from the gas or solution phases adsorb [5-7]. In order to use surfaces as templates for future ‘bottom-up’ fabrication, we need to understand the relevant factors that may influence self-assembled structures on solid surfaces. For example, the influence of the atomic lattice and the electronic effects of the substrate on non-covalent bonds, and in particular the lateral interactions between adsorbates and their coupling to the substrate will play a vital role in organizing structures on surfaces [8]. Furthermore, by combining such knowledge with supramolecular chemistry concepts, it will be possible to steer non-covalent interactions through the choice of substrates with proper symmetry, substrate potential corrugation, and chemical functionality. All of these can be used to tune the delicate balance of molecule-molecule interactions and molecule-substrate interactions to steer supramolecular assembly towards desired structures on surfaces.

Self-assembly has been widely investigated and receives increasing attention within the surface science and materials communities [9,10]. The invention of the scanning tunneling microscope (STM), in particular when working under ultrahigh vacuum (UHV) conditions, allows us not only to image the local supramolecular structures with molecular resolution, but also to manipulate individual adsorbates on surfaces. Due to these strengths of UHV-STM, this technique has become a powerful tool to study the adsorption geometry, *i.e.*, the registry of adsorbates on substrates, the conformations and dynamics of single molecules, and self-assembled supramolecular structures.

There are a number of studies on self-assembly of organic molecules, biologically relevant molecules, chiral or prochiral molecules, and even supramolecular compounds into two or three dimensional ordered structures by non-covalent interactions on solid surfaces under both ambient and UHV conditions. The advantage of performing the studies under ambient condition is that one can deal with relatively large compounds by depositing them from solution and then studying at the liquid/solid interface or in dry condition. Such studies have been attracting great attention recently [16-20,32-34]. However, under the ambient conditions high-resolution imaging of the self-assembled

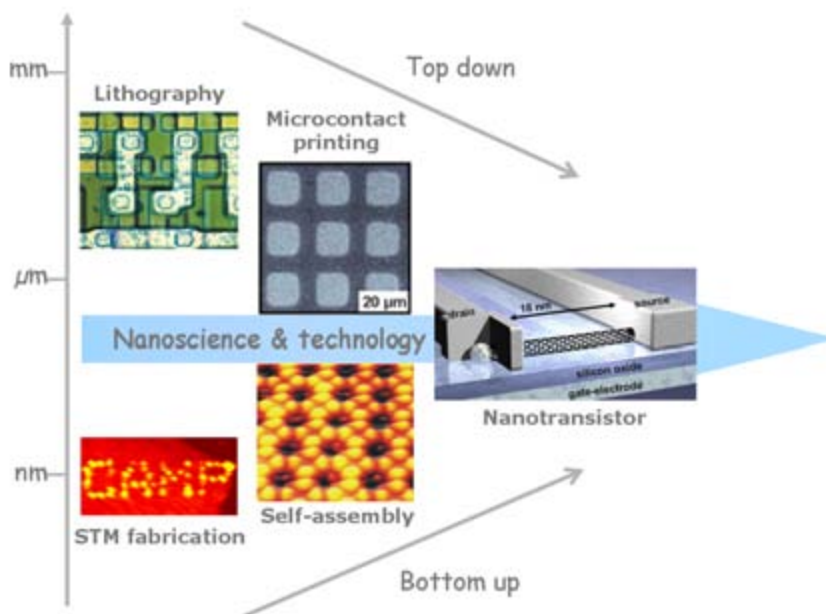


Figure 1.1: Two approaches to control matter at the nanoscale. For top-down fabrication, methods such as lithography, writing or stamping are used to define the desired features. The bottom-up techniques mainly make use of self-assembly for ordering of supramolecular architectures from individual atoms and molecules.

nanostructures is sometime hampered by the instability of the tip, the influence of solvent molecules, surface dynamic processes, etc. Thus, to study the fundamental molecule-molecule interactions or molecule-substrate interactions without any disturbance in the environment, a well-controlled UHV system is needed. However, the UHV-STM study is limited by the vacuum deposition methods. Normally, a simple thermal sublimation method is adopted to bring the molecules from solid phase to gas phase and adsorb on the surface subsequently. The drawback here is that it is difficult to deal with fragile compounds since they are labile to fragmentation during thermal sublimation or landing on the surface [35,36]. Most of the UHV-STM studies thus demonstrated fascinating results on relatively small and robust molecules. Recently, a pulsed doser has been developed to deposit molecules from liquid phase under UHV conditions to avoid possible thermal fragmentation [37].

1.2 Background review

The work presented in this thesis mainly consists of molecular adsorption studies covering the following topics: self-assembly of supramolecular nanostructures on surfaces (steered by H-bonding, van der Waals (vdW) interactions, metal coordination), investigation of molecular chirality and chiral recognition on surfaces, STM manipulation, etc. In the following several key topics will be briefly discussed to provide a general background for the studied systems.

1.2.1 Self-assembly

Self-assembly is a term used to describe processes in which a disordered system of pre-existing components forms an organized structure as a consequence of specific, local interactions among the components themselves, without external direction. This definition would apply for the structures in all length scales e.g. macroscopic object up to the universe and microscopic object down to human cells. Molecular self-assembly is a key concept in the context of supramolecular chemistry. It is defined as ‘spontaneous association of molecules under equilibrium conditions into stable, structurally well-defined aggregates joined by non-covalent bonds’. Three distinctive features can be singled out from this definition: i) The process is autonomous and without human intervention, in other words, the nanostructure builds itself. ii) The system undergoes thermodynamic equilibrium conditions and thus must lead to a lower Gibbs free energy in order for this process to take place. iii) It is joined by non-covalent interactions such as vdW forces, H-bonds, hydrophobic forces, π - π interactions, metal coordination, etc. with respect to more traditional covalent, ionic or metallic bonds. Molecular self-assembly is also crucial in biological systems e.g. the formation of double helical DNA structure through H-bonding of the complementary bases, and the assembly of proteins to form quaternary structures. Furthermore, molecular self-assembly is an important aspect of the emerging area of DNA nanotechnology, which uses the unique molecular recognition properties of DNA to create desired 2D or even 3D nanostructures in a well-controlled manner.

In this thesis we are discussing molecular self-assembly on surfaces, which is an even more complicated process. Atoms and/or molecules deposited on the substrates and nanostructures evolve as a result of multiple factors of surface dynamical processes, which is a non-equilibrium phenomenon and the growth scenario is steered by the competition of kinetics and thermodynamics. As pointed out in [1] the growth of molecular nanostructures at surfaces is mainly determined by the diffusivity of molecular adsorbates and deposition rate. If deposition is slower than diffusion, the adsorbates have enough time to explore the potential energy surface (of course the corrugation of the potential energy surface is also a limitation here) so that the system reaches a minimum energy configuration; that is, this occurs close to thermodynamic equilibrium conditions. On the other hand, if deposition is faster than diffusion, then usually metastable structures are kinetically trapped.

Normally, planar aromatic molecules would adopt flat geometry when adsorbed on inert substrates due to strong interaction between the aromatic π system and the metal substrate [1]. Hydrogen bonds are often used to steer the formation of supramolecular nanostructures due to the directionality and specificity of this class of interactions. For example, the PVBA and PEBA molecules have been systematically studied and coverage and annealing temperature dependent molecular structures on various single-crystals were reported [11-14]. To study molecular recognition process two-component systems are well studied. Such as studies on the biologically relevant molecule adenine and the mixture of adenine with amino acids were reported [7]. Such co-adsorption studies are another interesting direction of self-assembly. For example studies of self-intermixing C_{60} and subphthalocyanine on Ag(111) surface revealed how the stoichiometry plays a role on the mixture adsorption phase [15]. Also, well-ordered supramolecular networks can be formed by PTCDI and melamine through complementary hydrogen bonds [51]. Besides hydrogen bonds, other less specific interactions such as vdW forces and dipole-dipole interactions can also direct the formation of surface nanostructures. For example, it was demonstrated that dipole-dipole interactions between cyano-functionalized porphyrin molecules

adsorbed on Au(111) can steer the formation of different clusters and assemblies [2]. In the case of less directional vdW forces molecular geometry sometimes plays a role in organizing the self-assembled structures [168]. If the studied system includes multifunctional groups, all these possible intermolecular forces must be balanced against each other and against the molecule-substrate interactions [108,169,170]. It has been demonstrated that supramolecular networks can be tailored by applying metal-ligand interactions. In those cases open networks with controlled shape and size of the nanocavities can be formed through tuning the ratio of organic molecules and metal atoms or varying the pre-designed molecular building blocks [155-159]. In the Aarhus SPM group studies of self-assembly of organic molecules have also resulted in many achievements [21-25]. The cysteine molecule has been systematically studied to understand the molecular chirality on solid surfaces [26-30]. Large organic molecules such as HtBDC and lander molecules have been studied to understand the Lock and Key effect (that is the influence of the registry with the atomic lattice on the mobility of molecules) on solid surfaces [21,24,25,31]. These studies and many others have provided new insight into the physics and chemistry of adsorbates on solid surfaces. In this thesis self-assembly of small organic molecules e.g. NDCA and biologically relevant molecules e.g. DNA bases on metal surfaces will be described in detail.

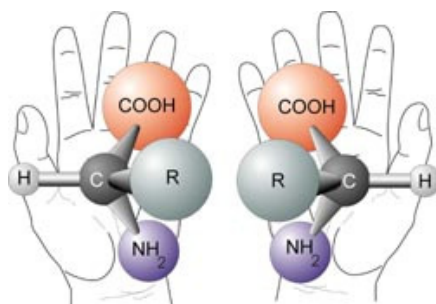


Figure 1.2: Two enantiomers of a generic amino acid.

1.2.2 Chirality

An object is called chiral if it cannot be superimposed on its mirror image (cf. Fig. 1.2). A chiral object and its mirror image are called enantiomers. A molecule is chiral if it contains a carbon atom which has four different substituents. Molecular chirality is abundant in biology such as amino acids and sugars are exclusively present as single enantiomers and thus many life processes are enantioselective and for example respond to only one chiral form of drugs. The origin of this homochirality in biology is still under debate. To gain fundamental insight into the discussion about chiral generation in nature and chiral recognition processes, a lot of attention has been given to molecular adsorption systems that show chiral phenomena on surfaces.

Generally, the chirality of a molecule can be transferred to the adsorption system (bring the molecule from gas phase to the surface) if the molecule is chiral in the gas phase. Such systems have been widely studied by STM to directly identify the molecular chirality and to study chiral recognition between amino acids and DNA bases [7,29,30,108-110]. Aside from truly chiral molecules, a large number of so-called prochiral molecules exist, which

are achiral in the gas phase, but become chiral once adsorbed on a surface with an associated loss of symmetry. Adsorption of such molecules always leads to equal amount of enantiomers on the surface either in homochiral domains or in heterochiral domains [7,111,112]. Another type of adsorption-induced chirality could occur for molecules that are even achiral. This is referred to as organizational chirality. In such case molecular adsorbates locally interact with each other in different manners resulting in two different arrangements that are chiral [168]. In this thesis analysis of chiral properties of the self-assembled surface nanostructures of DNA bases is performed.

1.2.3 STM manipulation

STM in particular with its ability to manipulate individual atoms and molecules has become a powerful tool not only to study the adsorption geometry, the conformational change, and dynamics of single molecules on solid surfaces, but also to build up nanostructures by individual atoms or molecular adsorbates in a controlled manner [97]. In the cases of simple adsorbates two main modes of STM manipulation are applied: vertical and lateral modes. In the lateral mode, the interaction between the tip and the sample is the driving force to move the adsorbate laterally on the surface. In the vertical mode, a voltage pulse is applied to transfer the adsorbate from the surface to the tip or vice versa depending on the polarity of the pulse. The pioneer works have been exemplified to show that using atomic manipulation methods custom-designed nanostructures can be achieved for example by moving a CO molecule on a Cu(111) surface [276] and positioning Fe and Co atoms on a Cu(111) surface [277,278].

Manipulation of large organic molecules has provided new insight into the physics and chemistry such as revealing the adsorption geometry and orientation with respect to the substrate (the so-called lock and key effect) [31], demonstrating the reconstruction of the terraces and step edges of Cu(110) by Lander-type molecular molding [21,23]. From a nanotechnology point of view manipulation of organic molecules has also displayed a broad range of applications. For example, it was recently shown that a Lander-type molecule can trap metal adatoms on the surface and form metallic clusters underneath [196]. Also, STM manipulation can serve as an engine to power a molecular wheel or nanocar on the surface [37,194].

Another possibility of STM manipulation is to create and break individual chemical bonds in a controlled manner by exciting particular vibration modes of the molecular adsorbates by inelastic tunneling [279]. In a later chapter of this thesis we will discuss how we can directly probe the hierarchy of bond-strengths involved in the surface self-assembly of multifunctional organic molecules with highly anisotropic interactions by STM manipulation. This is done by probing the different resistances that the bonds between neighboring molecules and supramolecules oppose to breaking under STM manipulation [68].

1.3 Outline of the thesis

The work presented in this thesis mainly deals with self-assembly of a variety of different adsorbates on solid surfaces ranging from the simplest atom, H, on the graphite surfaces over small organic and biologically relevant molecules to supramolecular complexes on metallic single-crystal surfaces. The studied systems are investigated by high-resolution

STM under UHV conditions. Some of the STM results are further supported by X-ray photoelectron spectroscopy (XPS), temperature programmed desorption (TPD), and density functional theory (DFT) calculations. **Chapter 2:** The experimental setup is described along with a brief description of the DFT method. **Chapter 3:** Adsorption of biologically relevant molecules DNA bases [guanine (G), cytosine (C), adenine (A), thymine (T)] on Au(111) has been carried out. Moreover, base complementarities have been studied by coadsorption of G+C and A+C on Au(111). Interaction between the G-quartet network and K^+ has also been studied. Further, results on DNA base derivatives will also be discussed at the end of the chapter. **Chapter 4:** Adsorption of the rosette supramolecular complex and its building blocks have been studied on Au(111). **Chapter 5:** Molecular molds (Lander type molecules) have been studied on Au(111) and Cu(110). **Chapter 6:** Adsorption of small organic molecule 2,6-NDCA on Ag(110) has been carried out. **Chapter 7:** Iridium(III) phosphorescent emitter molecule adsorbed on Cu(110) is investigated. **Chapter 8:** Adsorption of hydrogen atoms on graphite surfaces has been studied. Finally, the results are summarized in **Chapter 9.**

CHAPTER 2

Experimental setup and DFT basics

This chapter is devoted to a short description of experimental and theoretical methods underlying the work presented in this thesis. The emphasis is placed on our most important tool: The Scanning Tunneling Microscope (STM). In addition a brief section on density functional theory (DFT) is included.

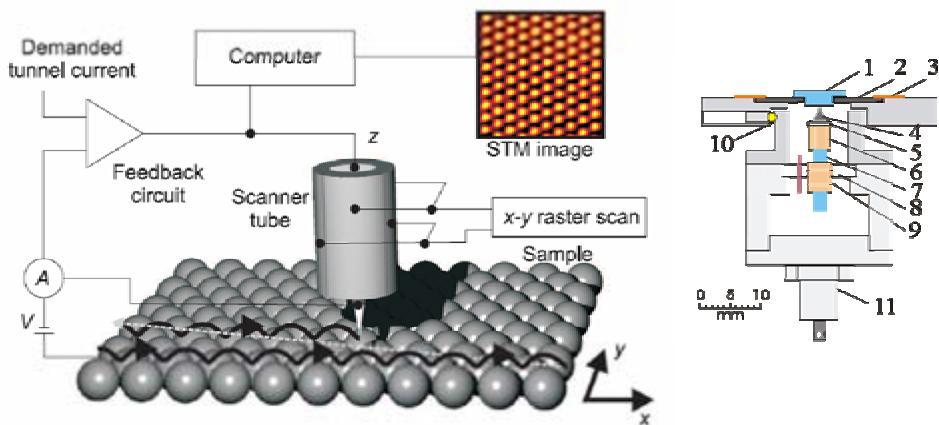


Figure 2.1: Left: The operating principle of a STM. Right: Schematic drawing of the Aarhus STM. See the text for details.

2.1 Scanning tunneling microscopy

The scanning tunneling microscope (STM) was developed in 1982 by Binnig and Rohrer [38], who both received the Nobel Prize for their development of the STM in 1986. The STM is a local probe with the unique capability of imaging and manipulating single atoms or molecules on conducting or semi-conducting surfaces. This capability gives a great advantage over the majority of standard surface science tools, and SPM has in general provided a tremendous amount of new insight into the physics, chemistry, molecular biology, medicine, etc. on solid surfaces. The basic principle of STM is indeed rather simple. STM exploits quantum mechanics, which allows electrons to ‘tunnel’ through a classically forbidden gap. This effect implies that if a sharp metallic tip is brought into such close proximity of the conducting surface, the wave functions of tip and the sample start to overlap. This typically occurs when the distance is less than 1 nm. Now if a bias voltage is applied between tip and sample, the tunnel current will be measured in nanoampere range, and this tunnel current strongly depends on the distance between tip and sample. If a positive bias voltage is applied to the sample, electrons will tunnel from the filled tip states into the empty sample states and vice versa. Usually STM images are recorded in *constant current mode*. In this mode a feedback loop is used to adjust the distance between tip and sample to keep the current constant at a predefined value while the tip is raster scanned across the surface. The principle of operation is illustrated in Fig. 2.1 (left).

2.1.1 Theory of STM

In order to understand the STM images, one needs to be able to calculate the tunneling current. However, this is a very complicated task, which requires knowledge of quantum mechanical states for both the tip and the sample. The formalism that is usually applied in theoretical calculations is that of Tersoff and Hamann [39]. They assumed to simplify

the tip and sample to be two non-interacting systems, and then in first-order perturbation theory the tunnel current is given by:

$$I = \frac{2e\pi}{\hbar} \sum_{\mu\nu} f(E_\mu)[1 - f(E_\nu + eV)] \times |M_{\mu\nu}|^2 \delta(E_\mu - E_\nu)$$

here $f(E)$ is the Fermi function, $M_{\mu\nu}$ is the tunneling matrix element between the tip states ψ_μ with energy E_μ and the sample states ψ_ν with energy E_ν . V is the bias voltage between the tip and the sample. Only elastic tunneling is taken into account as can be seen from the delta function.

The evaluation of tunneling matrix element $M_{\mu\nu}$ is the crucial point. Bardeen [40] showed that

$$M_{\mu\nu} = \frac{\hbar^2}{2m} \int d\vec{S} \cdot \vec{j}_{\mu\nu}$$

where $\vec{j}_{\mu\nu}$ is the current density operator and m is the electron mass. The integration is over any surface lying entirely within the vacuum gap region. Tersoff and Hamann then made the assumption that only s-wave tip states. For small bias voltage they get the following simple expression for the tunnel current:

$$I \propto V \sum_\nu |\psi_\nu(\vec{r}_t)|^2 \delta(E_\nu - E_f) = V \rho(\vec{r}_t, E_f)$$

it shows that the tunnel current is proportional to the bias voltage and the local density of states (LDOS) $\rho(\vec{r}_t, E_f)$ of the surface at the Fermi level evaluated at the centre of the tip apex (\vec{r}_t). So by using this approximation, the images obtained by STM in the constant current mode are images of contours of LDOS at Fermi level of the surface. Thus it is important to keep in mind that STM images are a convolution of the geometric and electronic structures of the surface.

Due to the surface wave functions decay exponentially into the vacuum gap, therefore the tunnel current depends exponentially on the tip-surface separation, which leads to the following relation between the tunnel current and the sample-tip distance s :

$$I \propto V \exp\left(-\frac{\sqrt{8m\phi}}{\hbar} s\right)$$

where ϕ is the work function and m is the electron mass. This exponential dependence of the tunneling current on tip-sample separation is indeed what enables the STM to obtain atomic resolution. For typical values of the work function, the tunneling current changes by a factor of 10 when the distance changes $\sim 1\text{\AA}$. For simple metal surfaces STM images will give a true topographic picture [41]. However, for adsorbates on the surface the situation is in general complicated [42,43], because the tip can tunnel different molecular orbitals for example HOMO or LUMO.

2.1.2 The Aarhus STM

To utilize the STM principle in real experiments one has to overcome huge barriers to ensure the positioning of the tip and sample within sub-Ångström precision. In the present

studies all experiments were carried out using the home-built Aarhus STM designed by Erik Lægsgaard *et al* [44].

A schematic drawing of Aarhus STM is shown in Fig. 2.1 (right). The sample (1) is placed in a tantalum holder (2), which may be removed from the STM, and which is normally held down on the STM top by springs (3). The top plate is thermally and electrically insulated from the STM body by three quartz balls (10). The top plate is mounted on a 0.6 kg Al block, which may be cooled to -160 °C or heated to 100 °C. The tip (4) is held by a macro holder (5), which is glued to the top of the scanner tube (6). The scanner tube is 4 mm long with an outer/inner diameter of 3.2/2.1 mm and is glued to the rod (7), which together with the piezo tube (9) forms a small inchworm motor used for coarse approach. The electrode of the tube is divided into three regions. In the tube two bearings are placed under the upper and the lower electrode with an extremely good fit to the rod (7). Applying a positive voltage to an electrode will clamp this electrode to the rod, whereas a negative voltage will free this electrode from the rod. A voltage applied to the center electrode will cause it to elongate or contract depending on the polarity of the voltage. With the right sequence of voltages applied to the three electrodes the rod will move up or down as the tube is fixed to the STM body by the macro ring (8). The motor may work in steps of down to 2 Å, but at full speed it moves around 2 mm/min. The scan range is up to ±1 µm when using antisymmetrical scan voltages of ±200 V. The Zener diode BZY93C75 (11) is used to counter heat the STM body during cooling.

2.2 Density functional theory

Density function theory (DFT) based calculation is a powerful tool for description of the ground state properties of complex many-body systems such as atomic or molecular adsorbates on solid surfaces. In this thesis DFT calculations have been applied to determine molecular adsorption geometries, self-assembled supramolecular structures in atomistic details, energy barriers, and atomic hydrogen recombination pathways on HOPG surface. All the calculations presented in this thesis were performed by theoreticians in the group of B. Hammer, University of Aarhus, and in the group of L. N. Kantorovich, King's College London. It should be pointed out that my own contribution to the theoretical studies thus lies entirely in the discussion and suggestions.

The basic idea in DFT is based on a theorem by Hohenberg and Kohn, which replaces the many-body wave-function Ψ with the electron density $n(\mathbf{r})$. Then the total external potential $v(\mathbf{r})$ (to within a constant) is a unique functional of $n(\mathbf{r})$ [45]. The Hamiltonian and thereby the total ground state energy E of the many-particle system can be expressed by the electron density and the sum of external fields $v(\mathbf{r})$

$$E = \int n(r)v(r)dr + \frac{1}{2} \iint \frac{n(r)n(r')}{|r-r'|} drdr' + G[n]$$

where the universal functional $G[n]$ is independent of $v(\mathbf{r})$.

Kohn and Sham split the functional $G[n]$ into two terms [46]:

$$G[n] \equiv T_s[n] + E_{xc}[n]$$

where $T_s[n]$ is the kinetic energy of non-interacting electron gas with density $n(\mathbf{r})$, and $E_{xc}[n]$ is the exchange and correlation energy of interacting electron gas with density $n(\mathbf{r})$.

By applying the variation principle of quantum mechanics, Kohn and Sham derived a set of single-electron Schrödinger equations:

$$\left\{ -\frac{1}{2}\nabla^2 + [\phi(r) + v_{xc}(r)] \right\} \psi_i(r) = \varepsilon_i \psi_i(r)$$

here the electron density is determined by single electron wavefunction $\psi_i(r)$

$$\sum_{i=1}^N |\psi_i(r)|^2 = n(r)$$

where N is the total number of electrons. The total electrostatic potential $\phi(r)$ is given by

$$\phi(r) = v(r) + \int \frac{n(r')}{|r-r'|} dr'$$

and the exchange and correlation contribution to the potential $v_{xc}(r)$ is given by the derivative of E_{xc}

$$v_{xc}(r) = \frac{\delta E_{xc}[n]}{\delta n(r)}$$

In DFT calculations the Kohn-Sham equations will be solved repeatedly by choosing a trial density $n(r)$, until self-consistency is reached. The total energy of the system is then given by:

$$E = \sum_{i=1}^N \varepsilon_i - \frac{1}{2} \iint \frac{n(r)n(r')}{|r-r'|} drdr' + E_{xc}[n] - \int v_{xc} n(r) d(r)$$

The only approximation which has to be made is in the parameterization of the exchange and correlation functional. Kohn and Sham used the local density approximation (LDA) in which the exchange and correlation energy is only a function of the density, which is a good approximation if the electron density varies slowly. The exchange and correlation energy $E_{xc}[n]$ is given by:

$$E_{xc}[n] = \int n(r) \varepsilon(n(r)) d(r)$$

However, LDA-based DFT calculations overestimate the binding energy for adsorbates on surfaces. For this reason other approximation such as generalized gradient approximation (GGA) has been introduced. In GGA the energy depends both on the electron density and the gradient of the electron density:

$$E_{xc}[n] = \int f(n(r), \nabla n(r)) d(r)$$

However, the GGA fails when the electron density varies too fast. So when DFT is applied to surface science studies other approximations have to be made.

2.3 Experimental methods

2.3.1 Adsorption of organic molecules on metal substrates

All STM experiments were performed in a UHV chamber (base pressure 3×10^{-10} Torr) equipped with the variable-temperature, fast-scanning Aarhus STM [47,48], a home-built molecular evaporator, and standard facilities for sample preparation. The Au(111), Cu(110), Ag(111), Ag(110) substrates were prepared by several cycles of 1.5 keV Ar^+ sputtering followed by annealing to 770-800 K for 15 min. Molecular powder was loaded into a glass crucible in the molecular evaporator. After a thorough degassing of the crucible, performed by keeping the crucible at temperatures slightly lower than the sublimation temperature for an extended period (~24 hours), molecules were deposited onto the clean metal substrate by thermal sublimation from the molecular evaporator, while the substrate was held at room temperature (RT). The STM experiments were carried out at low temperatures (100-150 K) to minimize the surface mobility of the deposited molecules and thereby stabilize the molecular nanostructures formed on the surface.

2.3.2 Adsorption of H atoms on HOPG surface

All experiments were performed using the home-built Aarhus STM under ultrahigh vacuum (UHV) at a base pressure below 3×10^{-10} Torr. HOPG samples were cleaved in air immediately prior to being inserted into the UHV chamber. In vacuum the samples were annealed to 1300 K by electron bombardment of the sample backside to desorb any hydrogen or oxygen bound at the surface and at step edges or defects. Atomic hydrogen dosing was performed using a hot (1600-2200 K) hydrogen atom beam source (HABS 40 from MBE Komponenten). The adsorption of hydrogen on the HOPG surface was confirmed by TPD experiments into a differentially pumped quadrupole mass spectrometer (QMS), equipped with a Fuelner cap cone with a 3 mm opening, which can be moved to within 1 mm of the sample surface. In the majority of the experiments, deuterium atoms were used to obtain a better signal-to-background ratio in the TPD experiments. All temperature measurements were performed by a type K thermocouple mounted on the backside of the HOPG sample.

CHAPTER 3

DNA bases and derivatives on Au(111)

In this chapter a systematic investigation of adsorption of DNA bases and its derivatives on Au(111) surface will be described. The project was inspired by the discovery of the fascinating DNA double helix structure fifty year ago, and base complementarity is thought to play a vital role in high-fidelity DNA replication process. However, the nature of the fundamental interactions driving this molecular recognition process for DNA replication is still being under debated. To simplify the studied system we have chosen the four single bases without a molecular backbone as a model system with the aim of getting fundamental understanding on the physiochemical interactions between the individual bases on surfaces and furthermore to study the base complementarity on surfaces. First, we investigated how individual bases adenine (A), thymine (T), guanine (G), cytosine (C) behave on the surface; as a result different self-assembled nanostructures formed by four bases will be detailed. Next, we investigated the molecular recognition process between complementary base pair C+G and non-complementary base pair C+A, which revealed that at slightly higher temperature than room temperature (RT) C could recognize its complementary partner G via forming Watson-Crick pair and eliminate its non-complementary partner A via phase separation. Meanwhile, the biologically relevant interaction between G-quartet network and K^+ has been studied and for the first time our high-resolution STM images reveal that K^+ could be incorporated into the existing G-quartet network, and by varying the dose of K^+ four different metallocsupramolecular networks were formed as a result of balancing between hydrogen bonds and metal ligand interactions. In the end of the chapter I will present some recent results on DNA base derivatives, which were synthesized in Prof. Kurt Gothelf's group from Center for DNA nanotechnology (CDNA).

3.1 Adenine on Au(111)

3.1.1 Introduction

The ability of molecules to self-assemble into larger nanoscale structures is an important research area due to its potential impact on future nanotechnological devices [1,33,49-52]. Many supramolecular structures can be formed by small organic molecules including all the DNA and RNA bases [7,53-70]. The self-assembly of these bases on surfaces may also have played an important role in the earliest appearance of life [71].

In spite of the great success that scanning probe methods have had in revealing the atomic-scale realm of matter, atomic resolution of molecular assemblies cannot be achieved since STM images, for example represent images of the local density of state at the Fermi level. Therefore, theoretical modelling is an essential step in interpreting such experimental scanning tunneling microscopy (STM) or atomic force microscopy (AFM) images. In most cases modelling of such systems is difficult due to commensurability problems arising from different periodicities of the surface potential and the gas-phase monolayer. The problem arises when one considers, within periodic boundary conditions, a monolayer of molecules and the surface explicitly. In general prohibitively expensive calculations involving large supercells are needed to address this problem. Usually, in self-assembled supramolecular nanostructures the inter-molecular interactions are expected to dominate when compared to the molecule-substrate interactions. Therefore, such self-assemblies are usually modelled in the gas phase.

However, this may not always be valid since the commensurability problem as well as the surface perturbation of the electronic structure of the adsorbed molecules may render their consideration in the gas phase approximate or even invalid. For instance, DNA bases adsorbed on the Au(111) [66,72] and adenine (A) on graphite surfaces lie flat at considerable distances from the surfaces [73], which demonstrates that the molecule-surface interactions are rather weak. On the other hand, A molecules are adsorbed in a strongly tilted manner on the corrugated Cu(110) surface [65,74], indicating much stronger molecule-surface interaction in this case. The case of the Ag-terminated Si(111) surface [64] is an intermediate case, since here the hydrogen bonding between the A molecules is balanced by their interactions with the surface leading to a flat self-assembled structure; this is not the most favourable structure in the gas phase and only becomes energetically favourable in the presence of the surface. Note that the essential point is not the absolute strength of the molecule-surface interaction, but the lateral corrugation of the surface potential.

From an interplay between STM imaging and DFT calculations, we address the balance between the molecule-surface and molecule-molecule interactions using self-assembled A structures on the Au(111) surface as a model system. Two A monolayer structures were observed by STM under ultrahigh vacuum (UHV) conditions, one of which is reported here for the first time. To interpret the structures at the atomistic level we use state-of-the-art density functional theory (DFT) calculations to show that the molecule-molecule interaction is affected very little by their interaction with the Au surface. This strongly suggests that the gas-phase analysis for most flat metal surfaces should be appropriate to obtain all the

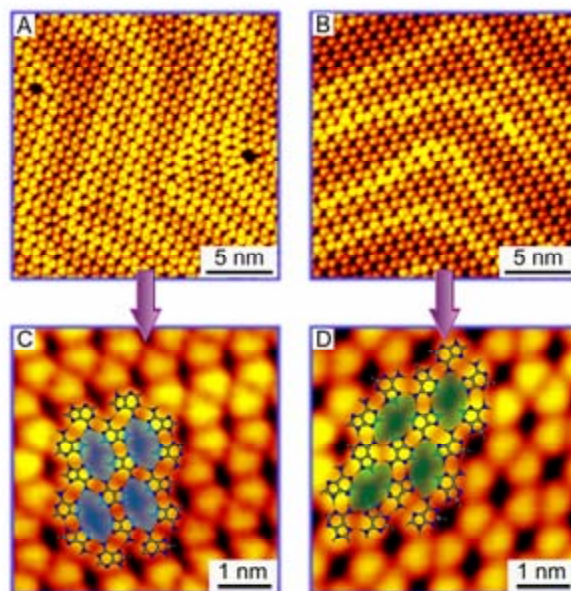


Figure 3.1: Experimental STM images and theoretical models for the adenine monolayers on the Au(111) surface. A and B show large areas of the two experimentally observed A monolayer structures, whereas C and D give close-up images with overlays of the theoretical models of A and B, respectively. Scanning conditions: $I_t = -0.5$ nA, $V_t = -1250$ mV.

energetically most favourable structures. These structures were obtained through a recently developed systematic approach based on a consideration of all possible A dimer connections between molecules in two dimensions [75], followed by detailed DFT calculations for specific cases. A comparison of the experimentally observed and theoretically deduced structures reveals the subtle role of the surface even in the case of a weak molecule-surface interaction, so that the structures which are most stable in the gas phase become less favourable on the surface and are actually not observed. At the same time, the observed structures, although not the most favourable in the gas phase, are accurately predicted by the gas-phase calculation.

3.1.2 Results and discussion

STM images recorded at 150K (Fig. 3.1A) show that the A molecules, upon deposition (at 370 K) onto a clean Au(111) surface held at room temperature, self-assemble into 2D well-ordered apparently non-chiral islands (phase I). This structure is consistent with the previously reported A monolayer structure observed on the Ag-terminated Si(111) surface [64]. Surprisingly, we also observe small areas of another, also non-chiral, self-assembled monolayer structure (phase II), which co-exists on the surface intermixed with phase I, usually at the elbow

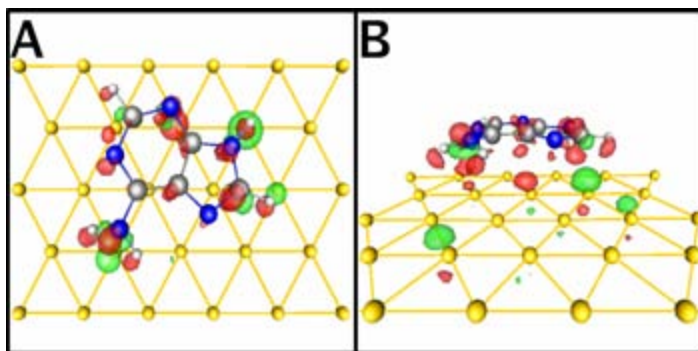


Figure 3.2: Top (A) and side (B) views of the difference density of the adenine on the Au (111) surface. Green contours correspond to positive electron density difference of $0.004 \text{ electrons}/\text{\AA}^3$ (i.e. charge excess regions), while the red contours correspond to the negative electron density difference of $-0.004 \text{ electrons}/\text{\AA}^3$ (charge depletion regions).

sites of the characteristic herringbone reconstruction of the clean Au(111) surface. After annealing to 370 K for 10 minutes, phase II (Fig. 3.1B), which has not been observed previously, has grown to become the dominating structure at the expense of phase I that vanished (Fig. 3.1B). Both structures form honeycomb networks where each A molecule is connected with three neighbours. However, as observed in the high-resolution STM images depicted in Figs. 3.1C and D and in particular in the gaps between the A molecules shown by ovals, we can conclude that the orientation of A molecules is different in the two structural phases. It is also seen from Figs. 3.1A and B that the adsorption of A molecules does not lift the herringbone reconstruction of the Au(111) surface, indicating that the molecule-substrate interaction is fairly weak, and that the growth of the 2D self-assembled islands is mainly controlled by molecule-molecule interactions.

To gain further insight into the experimentally observed A monolayer structures at the atomic level, *ab initio* DFT calculations were performed using the SIESTA method [76,77]. In our calculations full atomic relaxation was performed until the forces on the atoms were lower than $0.05 \text{ eV}/\text{\AA}$. When calculating stabilization energies, the basis set super-position error (BSSE) corrections were included [78]. This methodology has been extensively tested for various DNA and RNA base homopairs [79-81] and a large selection of heteropairs [82] by comparison with high-level quantum chemistry (QC) calculations [83-86]. We started our theoretical analyses by considering the interaction of a single A molecule and different A-A pairs with the Au(111) surface. The Au(111) surface was modelled using a 2 layer slab with the bottom layer atoms fixed in the bulk positions. We checked, using the slabs of up to 6 layers thick, that the 2-layer slab was sufficient for our purposes. To position the adenine molecule on the surface we chose a 5×5 extended super cell, which was checked to be big enough to avoid spurious interaction between the molecules across the surface. After relaxation a very small stabilization energy of around -0.1 eV was found for a single adenine molecule on the Au(111), in excellent agreement with recent plane-wave DFT calculations (-0.1 eV) [72]. Then the molecule was displaced and rotated by

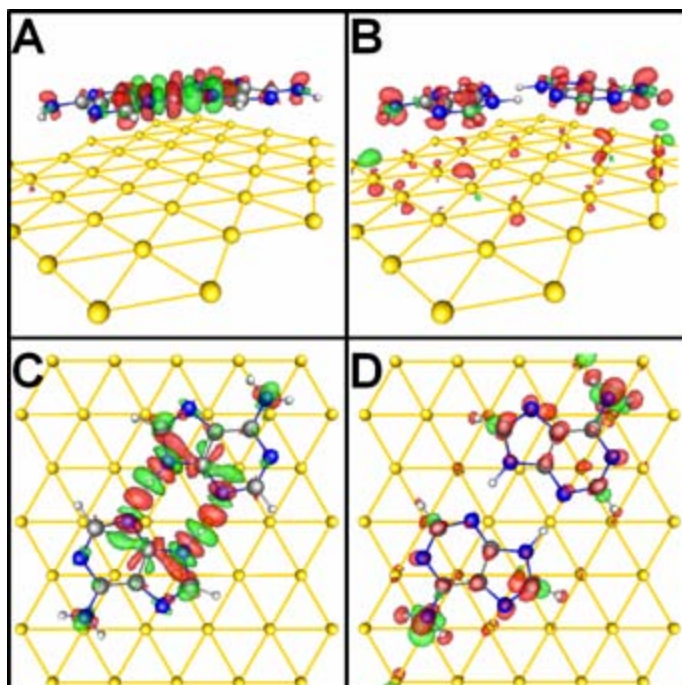


Figure 3.3: Side (A and B) and top (C and D) views of the difference density of the most stable adenine pair on the Au(111) surface. A and C correspond to the total density difference (between all three species) at the level of $0.01 \text{ electrons}/\text{\AA}^3$, whereas B and D show the partial density difference between the pair and the surface at $0.004 \text{ electrons}/\text{\AA}^3$. Colouring scheme is the same as in Fig. 3.2.

different random amounts and then allowed to relax again with very similar results. This result means that the potential energy surface is very smooth laterally, in agreement with similar calculations for guanine on Au(111) [66].

In all cases the A molecule was found to lie flat on the surface at the distance of about 3.5 \AA , in good agreement with other observations for weakly-bound π^* -systems lying flat on the fcc(111) metal surface [55-58,66,69]. An experimental study of adenine adsorption on Au(111) also suggests the planar geometry [87]. The planar adsorption geometry is facilitated by a partial charge transfer from the surface to the π^* -system of the hetero-aromatic molecule. The calculated charge difference density of the molecule on the surface (i.e. the electron density of the whole system minus the individual densities of all parts in the geometry of the whole system) also reveals small charge redistribution between molecule and surface (Fig. 3.2). The most notable charge redistribution is for the amino group, where the planarity is broken in favour of a pyramidal formation, indicating sp^3 hybridization, in agreement with the plane wave DFT calculations [69].

To investigate the influence of the gold surface on the ability of the molecules to form dimers and self-assembled monolayers, DFT calculations of the six most stable (in the gas phase) A pairs on the surface were performed using a 6×6 extended Au(111) supercell slab with two Au layers. All A dimers participating in

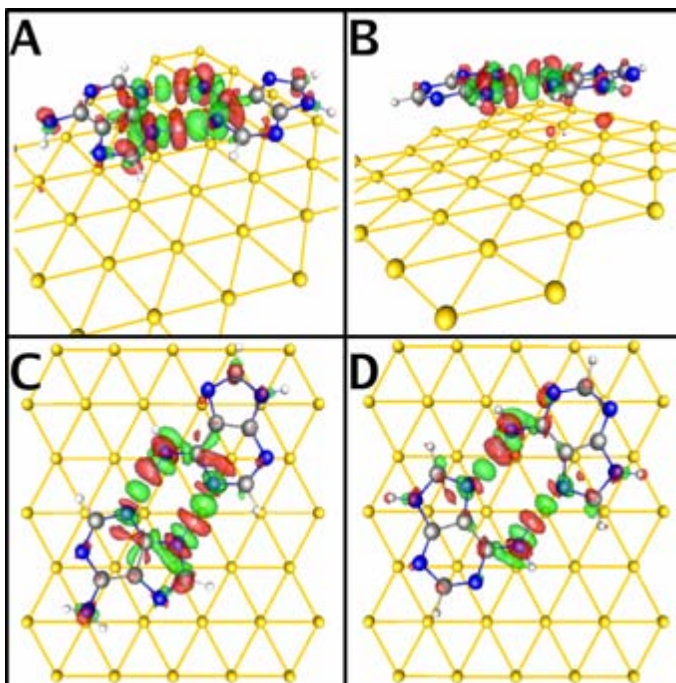


Figure 3.4: Side (A and B) and top (C and D) views of the total difference density (at the level of $0.01 \text{ electrons}/\text{\AA}^3$) of two adenine pairs (left panels) and (right panels) on the Au(111) surface, where amino group atoms are involved in the bonding. Colouring scheme is the same as in Fig. 3.2.

the monolayer structures responsible for the two observed phases (see below) were modeled on the Au(111) surface. The relaxed geometries (some of which are shown in Figs. 3.3 and 3.4) for all dimers and their flipped counterparts (B corresponds to the A flipped) were found to be planar and extremely similar to those in the gas phase. If the amino groups of the molecules do not participate in the hydrogen bonding, as is the case for the most favourable pair shown in Fig. 3.3, they remain in a sp^3 hybridized state with the pyramidal geometry. Note that the hydrogen atoms point downward towards the surface and the nitrogen point upwards.

From a detailed analysis of the calculations, we find that: (i) deformation energies of both the surface and the A dimers are negligible; (ii) A dimers adsorption energies are all very small, similar for different pairs and in all cases are almost exactly equal to twice the adsorption energy of a monomer reported above; (iii) energetics of A dimers and their flipped counterparts are practically identical, and are very close to that in the gas phase, and, finally, (iv) the total stabilization energies of all systems follow the same order as in the gas-phase. A small stability increase can be observed for all A pairs in which the amino group is involved in the hydrogen bonding. However, albeit systematic, this effect is within the precision of our calculations.

The obtained evidence of the weak effect of the surface on the ability of A molecules to form dimers via double hydrogen bonds is further corroborated by the charge density differences shown in Figs. 3.3A, C and Fig. 3.4 for selected pairs on the Au(111) surface. We find the characteristic “kebab” structure that shows regions of excess (green) and depletion (red) in the electron density along the donor-acceptor line for each hydrogen bond. Well-developed structures of these alternating regions along each bond, clearly seen in the figures, correspond to their high stability. If we compare these density differences with those obtained in the corresponding gas phase calculations (see Ref. [79]), we find that they are practically identical.

In spite of these similarities to the gas-phase situation, the charge density difference shown in Figs. 3.3 and 3.4 suggests that a certain density redistribution occurs due to interaction with the surface. In particular, there is some polarisation of the amino groups, clearly visible (see especially Figs. 3.3B and D where only the effect of the surface is shown). These results suggest that it is still necessary to be cautious when suggesting particular models for the two experimentally observed self-assembled A monolayer structures, as there is indeed a small influence of the surface.

Therefore, we have used the following approach for determining the appropriate atomistic models for the two A phases observed in the STM images: (i) systematically generate all possible gas-phase A monolayer structures by considering all possible A dimer connections leading to a hexagonal network; (ii) pre-select the ones which have suitable lattice vectors (within some error), are of the correct space symmetry, and have high stabilities; (iii) run full-scale SIESTA calculations on these structures and then (iv) make the final selection. By means of this approach two monolayer structures were identified to explain the observed assemblies and these are shown as overlays in Figs. 3.1C and D. The two structures have different orientation of the A molecules: in phase I A molecules are of the same chirality, whereas in phase II A molecules of both chiralities are present in equal amounts in the structure. The structure I is chiral, however, this may not be distinguishable in the STM image; the structure II is non-chiral in agreement with the observed chirality of this phase.

The two structures were found to have very similar gas-phase stabilities of -0.88 and -0.91 eV per molecule for phases I (Fig. 3.1C) and II (Fig. 3.1D), respectively. In fact, the existence of the thermodynamically more stable (in the gas phase) structure II is rather surprising and unexpected, because opposite to structure I, it does not contain the most stable A pair [79]. Thus, relying only on the most stable A pairs in constructing all monolayer possibilities [89] one would inevitably fail to identify these particular monolayer structures.

The transition between the two self-assembled monolayer structures can be explained as follows. Initially, the molecules which are deposited onto the surface would aggregate into the strongest base unit, namely the centrosymmetric dimer formation. These dimers would be free to join one another to form the monolayer phase I with homochiral domains. However, as the temperature is increased, a larger phase space is available to the molecules, which should facilitate the formation of phase II. Our SIESTA molecular dynamics (MD) simulations indicate that an individual molecule on a surface may flip at relatively low temperatures (400K). Hence, several processes may contribute to the formation of the heterochiral phase II: (i) mixing of molecules from neighbouring homochiral

islands of opposite chirality: the molecules detach from the islands edges and then diffuse across the surface; (ii) detached molecules flip and then attach again, and, (iii) detached molecules may desorb with subsequent adsorption of molecules of either chirality.

Actually, the two A monolayers that are observed and modelled here are not the most stable ones in the gas phase. Interestingly, the most stable gas-phase monolayer was used to explain the observed assemblies on the Cu(111), graphite and MoS₂ surfaces [55-63]. Since the calculation of the monolayers with the gold surface is too expensive to perform even for a single monolayer, as was explained above, we can only speculate here on the role of the Au(111) surface in picking up the particular structures. The observed effect of the surface is especially puzzling, as we have carefully proven, comparing geometry, energetics and the electron density of the A dimers in the gas phase and on the surface, that the effect of the latter on the A-A dimers must be very small. We tentatively suggest that the following factors may be in play here: (i) although interaction of a single A molecule and even of a A dimer with the Au surface is small, this may not be the case for large islands of A molecules observed in STM images: the accumulated strain due to mismatch may render some of the monolayers less preferable than the others; (ii) we have not taken into account the van der Waals (vdW) interaction between the molecules and the surface.

3.1.3 Conclusion

In summary, two adenine self-assembled monolayer structures, one of which is reported for the first time here, are experimentally observed by STM to co-exist on the Au(111) surface. Extensive calculations of adenine and its pairs with the Au(111) surface show that the interaction of one or two molecules with the flat metal surface, such as Au(111), is very weak. Moreover, the effect of the surface on the hydrogen bonding between molecules is also very small. However, observations of small redistribution of the electron density between the adenine molecules and the Au surface indicate that there might be some lateral registry with the underlying surface. This interaction perturbs the much stronger inter-molecular interactions binding the molecules together in the monolayer. The peculiar effect of this is that the most stable gas-phase monolayer [53,67,88,89] seems to be distorted so much on the surface that, to relieve the strain, another gas-phase monolayer, which has a different periodic pattern, becomes more energetically favourable, especially for islands larger than a certain size. Hence, although the gas-phase analysis of possible monolayer structures should still be considered as an essential step in the modelling of supramolecular assemblies on flat metal surfaces, care should be exercised in choosing possible configurations as models for the observed structures: one cannot exclusively rely on the order of stability of different gas-phase structures as these may be modified by the cumulative effect of the surface.

3.2 Thymine on Au(111)

The self-assembly of multifunctional molecules takes place in a hierarchical manner in which the stronger bonds steer the growth of smaller supramolecular structures composed of fewer molecules, whereas the weaker bonds direct the further aggregation of the supramolecules formed in the previous step. The characterization of the hierarchy of bond-strengths in self-assembled structures usually involves structural studies of the relative position and orientation of the functional groups, as a means of revealing their relative interaction strengths. From the interplay of variable-temperature scanning tunneling microscopy (STM) experiments and state-of-the-art density functional theory (DFT) calculations, here we show that using STM manipulation we can directly probe the hierarchy of bond-strengths involved in the surface self-assembly of multifunctional organic molecules with highly anisotropic interactions. This is done by probing the different resistances that the bonds between neighboring molecules and supramolecules oppose to breaking under STM manipulation. The method of selective intermolecular STM-induced bond breaking can offer unique possibilities to determine the position of the weaker bonds within a self-assembled organic monolayer, and can thus be used to help identifying particular features of the molecular architecture in the observed STM images.

3.2.1 Introduction

Our knowledge about molecular self-assembly on solid surfaces has increased significantly over the last few years [32], motivated by the large number of applications based on thin and ultra-thin self-assembled organic films in areas such as organic semiconductors [90], organic photovoltaic devices [91], nano-mechanical biosensors [92], etc. The molecular systems studied have been continuously growing in complexity, and one sub-area which has been studied extensively both experimentally and theoretically is self-assembled monolayers of molecules with several kinds of interacting functional groups, such as DNA bases or amino acids [7,30,66,93]. It is generally expected that for such molecules with multifunctional groups a hierarchical self-assembly process exists. During this process directional bonds (e.g. hydrogen bonds) determine the formation of supramolecular structures in the first place (at low surface coverages), while weaker interactions (e.g. van der Waals (vdW) interactions) become more important with increasing surface coverages, and then direct the subsequent self-assembly of the supramolecules formed initially. For this kind of experiment, STM has proven to be the technique of choice, since it allows a direct, real-space determination of the symmetry properties of the molecular network as well as of unit-mesh distances and angles at the atomic scale. However, to obtain further insight into the detailed molecular structures from the STM images, to address questions such as the molecular adsorption conformations and to distinguish the different interactions in self-assembled structures, comparison with advanced theoretical modeling of the STM images is requested [30,66,94-96].

In this work we have investigated by means of high-resolution scanning tunneling microscopy (STM) imaging and manipulation [97] the spontaneous assembly and STM-induced disassembly of one of the DNA base molecules, thymine (T), deposited on the Au(111) surface under ultrahigh vacuum (UHV) conditions. The Au(111) substrate was chosen as a noble inert substrate to minimize molecule-substrate interactions, thus

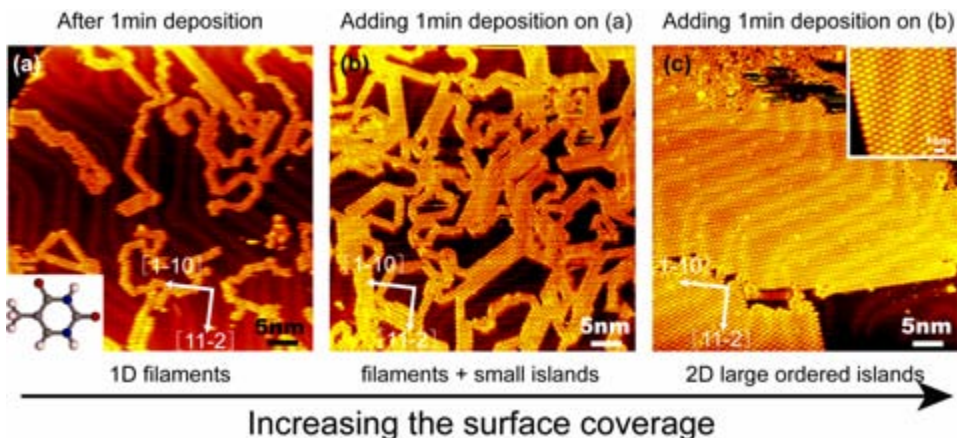


Figure 3.5: (a) STM image of several self-assembled 1D T filaments with random growth directions on the Au(111) surface at low surface coverage. The lower inset shows the chemical structure of a thymine molecule. (Tunneling conditions: $I_t = -0.23$ nA, $V_t = -1051$ mV). (b) STM image containing 1D T filaments and small islands corresponds to an increased surface coverage ($I_t = -0.61$ nA, $V_t = -1486$ mV). (c) STM image of extended 2D ordered T islands observed when the surface coverage is increased even further to ~ 0.3 – 0.4 ML ($I_t = -0.65$ nA, $V_t = -2102$ mV). The inset shows a zoom-in STM image of the 2D T island structure with high molecular resolution.

allowing the self-assembly process to be dominated by intermolecular interactions. Thymine is a prime example of the above-mentioned multifunctional organic molecule capable of forming strong hydrogen bonds through the carbonyl and imino groups, whereas the methyl group enables it to interact via weaker vdW interactions. The STM results reveal a two-step hierarchical self-assembly process in which initially hydrogen bonds steer the growth of 1D filaments of T molecules that subsequently (for higher coverages) self-assemble into 2D T islands via the weaker vdW interactions. This growth mode is confirmed by the state-of-the-art density functional theory (DFT) calculations, which also enable a clear identification of the 1D T filament structures. We furthermore show that by using STM manipulation we can directly probe the hierarchy of bond strengths involved in the surface self-assembly of T molecules with highly anisotropic interactions. This is done by probing the different resistances that the bonds between the neighboring T molecules and between the supramolecular T filaments oppose to breaking under STM manipulation. Our experimental results demonstrate that STM manipulation can be used to selectively break the weaker vdW bonds, resulting in the lateral disassembly of the weakly-bound 2D T islands into their constituent T filaments. These manipulation experiments support the hierarchical picture that results from a comparison between theory and STM images, and thus demonstrate the usefulness of STM manipulation to detect the “weakest link” in hierarchical self-assembled molecular structures, a hint that can be of the utmost relevance to identify molecular adsorption geometries from STM images.

3.2.2 Results and discussion

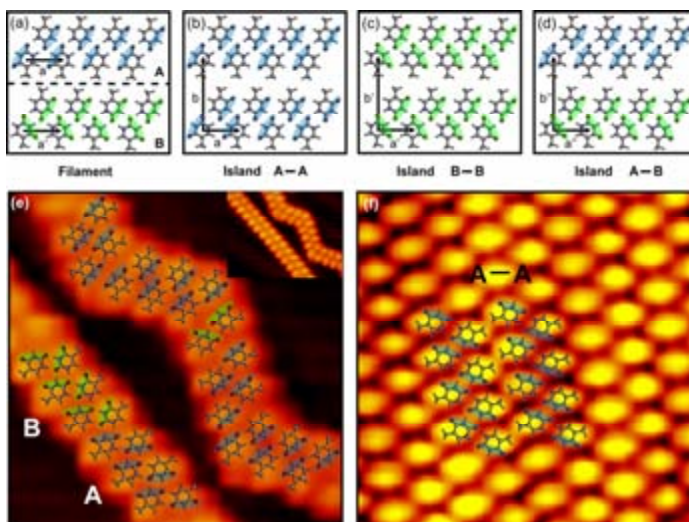


Figure 3.6: (a) DFT calculated most stable filament structures A and B with very similar lattice vectors \mathbf{a} and \mathbf{a}' . The colour coding is used to distinguish two different hydrogen bonded filament structures. (b), (c) and (d) show three possible models for the observed 2D islands as shown in (f). All three have very similar lattice vectors as shown in the figures. (e) Overlay of two calculated most stable filament structures A and B (as shown in (a)) on the STM image of a linear filament, and a theoretically proposed structure for a bent filament. The upper inset shows the zoom-in STM image of the T filaments with molecular resolution. (f) Comparison of the periodic A-A structure of 2D T island shown in Fig. 3.6(b) with the STM image.

As seen from Fig. 3.5a the STM images recorded at 120 K show that at low surface coverage (less than 0.1 ML) the T molecules, upon deposition (at 350 K) onto a clean Au(111) surface held at room temperature, self-assemble into 1D filaments. It is seen from Fig. 3.5a that the filaments grow along random directions on the surface, and the adsorption of T molecules does not lift the characteristic herringbone reconstruction of the clean Au(111) surface. These two findings suggest that the molecule-substrate interaction is fairly weak, and that growth of the 1D filaments is mainly controlled by molecule-molecule interactions. The weakness of the interaction between a T molecule and the gold surface was also confirmed by our DFT calculations (adsorption energy near 0.05 eV) as will be discussed below. Interestingly, upon a gradual increase in the coverage of the deposited T molecules up to 0.1~0.2 ML, a local ordering sets in and some of the T filaments start to attach to each other side by side and grow into small patches of T islands. However, all these structures can still be considered as consisting of mainly T filaments (Fig. 3.5b). As the coverage is increased even further (up to 0.3~0.4 ML), well-ordered 2D T islands nucleate and grow as the overall dominating structure on the surface. A few filaments can still be observed at the upper boundaries of the 2D islands (Fig. 3.5c). If instead of depositing the T molecules sequentially, we deposit the same coverage of T molecules continuously, we observe similar well-ordered 2D T islands. This growth mode is different from the growth mode of another DNA base molecule (cytosine), which initially also forms 1D filaments along random growth

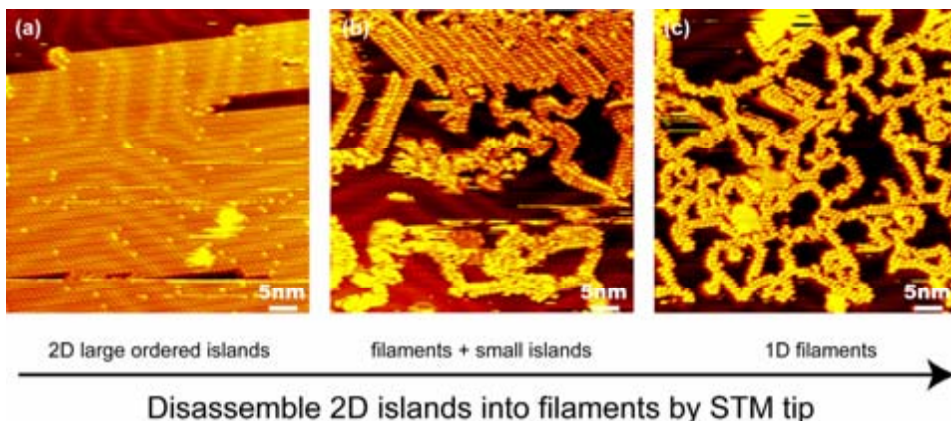


Figure 3.7: In-situ STM images (a) to (c) show that the 2D T islands can be decomposed into 1D T filaments by STM tip related manipulation. After giving a pulse on the right down corner of Fig. 3.7(a), a localized disturbed part (lower part) and unperturbed area (upper part) are found as shown in Fig. 3.7(b). After giving several pulses on Fig. 3.7(b), a homogeneous area of filamentary structure is found as shown in Fig. 3.7(c). It indicates that weak vdW interactions between parallel T filaments can easily be overcome. However, the stronger H-bonding which binds the filaments is not affected so much. Imaging conditions are the same for all three images: $I_t = -0.6$ nA, $V_t = -2102$ mV.

directions at low surface coverage, but we never observed the cytosine filaments to merge into 2D ordered structures even at a saturation surface coverage [69].

To gain further insight into the atomistic structure of the observed T filaments, we have carried out *ab initio* DFT calculations for a variety of different filament structures. To systematically construct all possible filament structures, it is convenient to first assume that linear T chains (see inset in Fig. 3.6e) are constructed by repeating just two molecules (thymine pairs [80]) periodically. Following this method, we find 9 possible chain structures, which were all fully relaxed using the DFT method. The two energetically most favorable chain structures (referred to as A and B in the following) with similar binding energies of 0.77 eV per molecule are shown in Fig. 3.6a. They consist of two rows of T molecules linked to each other by hydrogen bonds. The model B filament can be obtained from model A by flipping the molecules of one of the rows. The two lowest energy chain structures are found to have the same lattice vector of 6.8 \AA , which fits the experimentally observed linear T filament structures of $6.5 \pm 0.5 \text{ \AA}$ quite well. Fig. 3.6e shows a comparison of the two most stable calculated linear filament structures (marked A and B) with the filaments observed in the STM images at low coverage. An excellent agreement is found for either of them, since the T molecules have a symmetrical, featureless appearance in the STM images. Hence, we cannot distinguish between the two chain models A and B of T filaments in the STM images out of symmetry considerations. Furthermore, the two most stable filaments may also link to one another end-to-end (note that end-to-side connections as in the case of cytosine [69] are not possible in this case, since they are sterically hindered by the methyl groups). These connections can be systematically constructed by considering all possible ends of finite filaments and their stability estimated by the binding energies of the corresponding

T dimers involved in the link. Some links result in bent T filaments, while others keep the linearity of the filament structures (see the overlay in Fig. 3.6e).

Based on the different possibilities for which T molecules [80] bind into the chain structures discussed above and from the coverage-dependent phase transition from the 1D filaments to the 2D islands, we suggest that the 2D T islands are hierarchically made up by the most stable T filaments attached parallel to each other and bound together by vdW interactions between their methyl groups [98,99]. Since the two filament models (A and B) are very similar and filaments may mix in a linear structure, many 2D island structures exist. Examples of A-A, B-B, and A-B structures are shown in Figs. 3.6b, c and d, respectively. The binding energies of all these structures are expected to be very similar. As an example, we show in Fig. 3.6f that a good agreement exists between the model A-A of T islands and the observed STM image. Such a self-assembled monolayer of thymine molecules at the solid/liquid interface has also been proposed previously [100]. Therefore, we suggest that the 2D islands present on the surface are actually disordered in the sense that they contain various mixtures of T filaments joining end-to-end as well as side-by-side. The latter connections are stabilized by the vdW interactions between the methyl groups of T molecules in neighboring T filaments.

Since the T filaments are linked together by the fairly weak vdW interactions, which results in the formation of the 2D T islands, one could speculate that the islands might somehow be more easily disassembled into randomly distributed filaments than into monomeric T molecules or any other supramolecular portion of the ordered islands. This hypothesis can indeed be confirmed experimentally since we have succeeded in reversing the growth process and forming 1D filaments from 2D islands by perturbing the 2D island structures by the STM tip as shown in Figs. 3.7a to c, where the scanning temperature is kept at 100-120 K. During the scanning of the T islands we applied a voltage pulse, ramping the voltage from 1 V to 10 V in a few ms. Note that after STM manipulation (i.e. blowing apart the 2D islands), we only observed 1D filaments rather than random T fragments with different shapes and sizes. This observation implies that there are different interactions between T molecules that can be split into two types: (i) strong H-bonding which binds the molecules in filaments (ii) much weaker vdW interactions (at least one order of magnitude weaker than H-bonding) which bind filaments together. Although, at the moment the detailed mechanism causing the transition from the 2D islands into the 1D filaments is not clear; it might be caused by field-assisted manipulation [101], or by inelastic tunneling [102]. At the same time, it might also be that some T molecules desorb from the surface due to the voltage pulse [103], leading to a slightly lower coverage after the manipulation. However, regardless of the detailed mechanism actually in play, we demonstrated that this manipulation process is capable of breaking the 2D islands into separate filaments by targeting the fragile vdW interactions without disturbing the stronger hydrogen bonds that hold the filaments together.

3.2.3 Conclusion

In this study, the adsorption of T molecules on the Au(111) surface has been investigated at various coverages using STM imaging and manipulation. We have shown that the multiple functionalities with which thymine molecules are endowed allow them to interact through both strong multiple hydrogen bonds and weak vdW interactions. This leads to a kinetically hierarchical self-assembly in which 1D T filaments stabilized by

hydrogen bonds are formed initially at low coverages, after which the filaments, steered by the vdW interactions, self-assemble laterally into 2D T islands. We have shown that a high-voltage pulse applied during scanning leads to a disassembly of the ordered 2D islands into the same 1D filaments as obtained by depositing T molecules at low coverages. Notice that the assignment of the different interactions leading to 1D filaments and 2D islands is done on the basis of high-level theoretical calculations and predictions. However, similar conclusions could be obtained exclusively on the basis of the selectivity in the intermolecular bond-breaking mechanism. Thus, this technique of selective disassembly of hierarchical self-organized molecular structures into their higher-level supramolecular constituents might offer valuable new insights into the nature of the intermolecular interactions, and thus, in assigning orientations of molecules in the observed STM images.

3.3 Guanine on Au(111)

3.3.1 Introduction

The convergence of two scientific branches, design of low-dimensional systems on the nano-scale in condensed matter physics and the controlled growth of nucleotide sequence in molecular biology, has the potential to lead to new routes of directed self-assembly of molecular nanostructures at surfaces [104-107]. Among self-assembly processes stereochemistry often plays a crucial role in controlling molecular recognition and interaction, not only in nature but also in the field of molecular self-assembly at surfaces [29,30,108]. Chiral specificity is therefore of fundamental interest in molecular biology and surface science. Scanning Tunneling Microscopy (STM) is the technique of choice to locally probe chiral phenomena at surfaces at the single molecule level [33,49]. Significant insight has already been obtained from previous STM studies, where it has been shown that the chirality of adsorbed molecules can be determined [109], providing there is direct evidence for intermolecular chiral recognition between, for example, amino acids and DNA base molecules [7,30], and spontaneous assembly of adsorbates into extended enantiomerically pure islands [110]. Aside from truly chiral molecules, a large number of so-called prochiral molecules exist, which become chiral once they are adsorbed on a surface (with an associated loss of symmetry) [111,112].

Here we present STM results for the adsorption of one of the DNA base molecules guanine (G) onto the Au(111) surface. Guanine molecules adsorbed onto the surface will adopt a flat geometry [66] with an orientation either face up or face down due to confinement by the surface, so that guanine is said to be a prochiral molecule. The self-assembled G nanostructures are found to consist of nearly square building blocks (quartets) consisting of four molecules. The inter- and intra-quartets bonds between G molecules are hydrogen bonded. Directly upon deposition of G molecules at room temperature we found that an overall heterochiral phase including two enantiomerically pure homochiral G-quartet networks is formed, whereas upon annealing at 400 K a racemic G-quartet network was observed. *Ab initio* Density Functional Theory (DFT) calculations give further insight into the formation of these different G-quartet nanostructures, and it is revealed that the racemic G-quartet network is a dual-state network stabilized by entropy.

3.3.2 Results and discussion

After deposition of G molecules, the sample was transferred in-situ to the STM. Figure 3.8a shows that upon deposition (at 420 K) onto the clean Au(111) surface held at room temperature the G molecules self-assemble into well-ordered molecular nanostructures with irregular shape, which is in good agreement with previous findings [66]. The adsorption of the guanine molecules does not lift the herringbone reconstruction of the Au(111) surface, which implies a rather weak interaction between the molecules and the substrate. Furthermore, previous DFT calculations of individual G molecules on the Au(111) surface reveal that the G molecules bind weakly to the gold surface in a configuration with the G molecules lying flat on the Au(111) surface, so that the individual G molecules are highly mobile on the surface and there is no preferential position or orientation for adsorption [66]. Hence, the stability of the self-assembled G

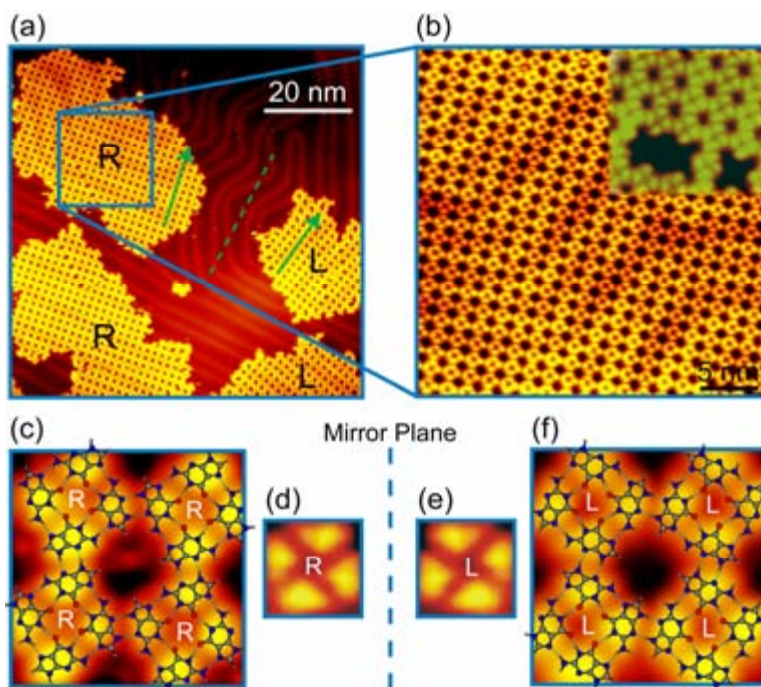


Figure 3.8: (a) A typical STM image containing mirror phases of R and L G-quartet networks. (b) A zoom-in of the R G-quartet network; inset: a molecular-resolved STM image of the R G-quartet network. (c) STM image of enantiomerically pure R G-quartet network with the superimposed theoretically calculated molecular model, which shows intra- and inter-quartet hydrogen bonding stabilizing the structure. (d) The unit cell of the R G-quartet network. (e) The unit cell of the L G-quartet network. (f) STM image and the theoretically obtained molecular model for the enantiomerically pure G-quartet network with L chirality. Scanning conditions: $I_t = -0.5 \sim 1$ nA, $V_t = -700 \sim 1250$ mV.

nanostructure is predominantly due to inter-molecular interactions, i.e. the hydrogen bonding between the G molecules [53].

Fig. 3.8b shows a close-up STM image of the self-assembled molecular nanostructure of the G network. Despite the hexagonal symmetry of the substrate, the guanine network displays an almost square lattice with the high space group symmetry $p4$. The high-resolution STM image (inset in Fig. 3.8b) shows that the individual G molecules are depicted in the STM images as triangular shapes and that four G molecules in a chiral arrangement form the unit cell (marked R in Fig. 3.8d). This network is associated with the previously reported G-quartet network [53,66]. In Fig. 3.8c we have superimposed the hydrogen-bonded molecular model obtained from ab initio DFT SIESTA calculations [76,77] on top of the STM image. As can be seen eight intra-quartet hydrogen bonds are formed to stabilize the quartet motif and another eight inter-quartet hydrogen bonds link adjacent quartets to each other to form the observed G-quartet network. As mentioned above, the surface induced chiral states of the G molecule should co-exist in equal portions. It is therefore expected that the other enantiomeric phase with respect to that shown in Fig. 3.8b should co-exist on the surface. Indeed, Fig. 3.8a shows islands (marked L) which have a different orientation with

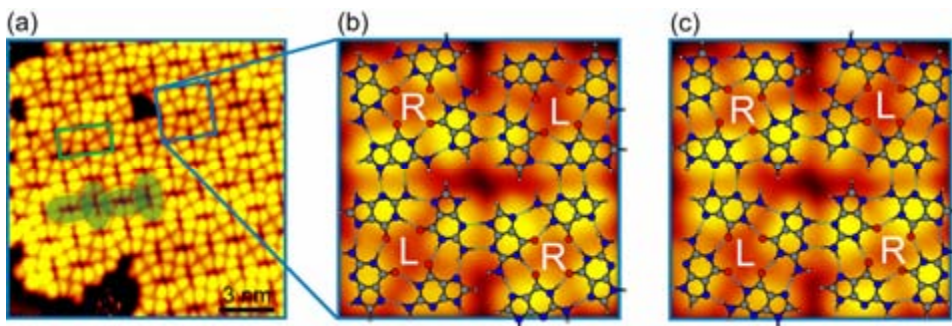


Figure 3.9: (a) STM image of the racemic G-quartet network. The unit cell is highlighted by a green rectangle. (b) The theoretically calculated molecular model A superimposed on the zoom-in STM image. (c) The theoretically calculated molecular model B superimposed on the same zoom-in STM image. Scanning conditions are the same as indicated in Fig. 3.8.

respect to islands marked as R. High-resolution STM images allow us to identify the detailed structure of islands L, the unit cell of which is shown in Fig. 3.8e, which is the mirror phase of the islands R. The theoretically calculated molecular model superimposed on the STM image of island L is shown in Fig. 3.8f. Upon adsorption of the prochiral G molecules onto the Au(111) surface, a surface-induced chirality is generated, which leads to the formation of two different chiral quartets (R and L, respectively). Subsequently, the R and L quartets serve as molecular building blocks to grow into enantiomerically pure R and L extended islands through inter-quartet hydrogen bonding. The surface-induced chirality is thus amplified from 0 dimension (single G-quartet motif) to 2 dimension (homochiral G-quartet islands) during this molecular recognition process. In Fig. 3.8a we thus observe a heterochiral phase formed by two enantiomerically pure homochiral R and L G-quartet networks coexisting on the surface.

Interestingly, by annealing the sample at 400 K the heterochiral phase can be transformed irreversibly into a racemic G-quartet network as shown in Fig. 3.9a. The unit cell of this racemic G-quartet network containing two quartets has been highlighted by a green rectangle in Fig. 3.9a. The theoretically calculated molecular model referred to as racemic structure A is superimposed on the STM image in Fig. 3.9b. Each quartet in this racemic G-quartet network is joined to any of the four adjacent quartets via two hydrogen bonds as was the case for the enantiomerically pure G-quartet network. However, in the racemic phase each quartet only joins to quartets with the opposite chirality as indicated in Fig. 3.9b, which results in a characteristic pattern of G quartets forming oval gaps running at 90° to each other through the whole network indicated by shadows in Fig. 3.9a. This racemic structure has much lower space symmetry $p2$.

A thorough analysis of the racemic structure A, as superimposed in Fig. 3.9b, shows that it is actually prochiral. By flipping the racemic structure A, an atomistically different structure, which we shall refer to as racemic structure B, is obtained in which quartets are connected with each other in a different manner as seen by comparing the molecular models shown in Fig. 3.9b and c. Furthermore, both structures can fit well with the STM images as can be seen by superimposing both models onto the same STM image as shown in Figs. 3.9b and c. Basically the positions of the quartets and the oval gaps between them change very little making them indistinguishable in our STM images.

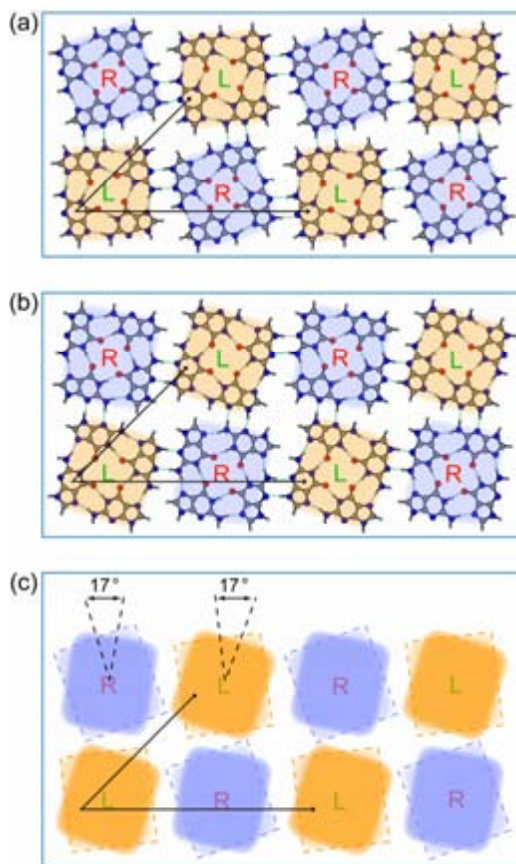


Figure 3.10: (a) The racemic structure A. (b) The racemic structure B. (c) Schematic of the relative distortion relating the two racemic structures A and B, where the dashed box corresponds to structure A and the solid box to structure B.

This new racemic structure is fascinating, as both of the two prochiral structures A and B can be obtained from each other by a continuous transformation corresponding to simultaneously pinning of all quartets R and L, and then rotating each of them by the same angle of about 17° , as shown schematically in Figs. 3.10a-c. Both structures have the same periodicity (lattice vectors) as indicated in Fig. 3.10 and identical stability in the gas phase since they are also mirror images of each other. Since the transformation from structure A to B or vice versa would require breaking of the existing double hydrogen bonds between quartets and establishing new ones after the rotation, an energy barrier must exist for the transition from one racemic structure to the other ($A \leftrightarrow B$). Hence, this situation corresponds to a double-well potential configuration where a minimum energy path exists on the potential energy surface, which connects the racemic structures A and B, with equal barriers on either side.

Our DFT calculations show that the racemic structure has a lower stability by 0.54 eV (per quartet) than the homochiral one (-4.00 eV and -4.54 eV, respectively). However, the racemic structure has two states of the same energy (structure A and B), whereas the homochiral structure has only one. Hence, the racemic structure should have higher

entropy and to a first approximation, it is higher by $k_B \ln 2$. A more thorough and rather expensive calculation, (not performed here) should also take into account the different vibrational contributions and thus its free energy, $G=H-TS$, will become lower at high enough temperatures. Therefore, we suggest the following explanation for our observations. When the G molecules are sublimated onto the surface at RT, they primarily form G quartet motifs, as these are the most stable small clusters stabilized by cooperative hydrogen bonds as proposed previously [66]. Due to equal supply of R and L G molecules, an equal number of R and L G-quartets exist. Since, our calculations show that the interaction between homochiral quartets (R-R or L-L) is stronger than the interaction between heterochiral quartets (R-L), thus R and L quartets at RT prefer to form homochiral G-quartet networks (i.e. R and L G-quartet networks segregate). When the sample is annealed at 400 K, the inter-quartet hydrogen bonds can be broken relatively easily and the homochiral G-quartet network undergoes the transition into the new racemic phase in which it fluctuates between the two structures A and B. After subsequent fast cooling to 100 K prior to the STM measurements, one of the racemic structures either A or B or both, become kinetically trapped and are observed in the STM images. Therefore, our observations and the theoretical analysis clearly demonstrate that the homochiral G-quartet network is energetically favorable at RT, while the entropically stabilized racemic G-quartet phase becomes energetically more favorable at higher temperatures, as observed experimentally.

Note that the existence of the racemic G-quartet structure cannot be explained by formation at high temperature of guanine tautomers observed experimentally [114,115] and studied theoretically [116], since all most stable forms are found to be inconsistent with the G-quartet structure as we observed.

3.3.3 Conclusion

In summary, we have demonstrated that the surface-induced chirality of the prochiral G molecule can be generated and amplified by room-temperature adsorption. Enantiomerically pure and racemic phases are observed, the latter being obtained by annealing to 400 K and subsequent cooling to 100 K prior to the STM analysis. This racemic structure is explained as an entropically stabilized dual-state molecular structure. Our findings may lead to a rational design of 2D supramolecular surface nanostructures with a specific chirality. This may be of particular interest for creating functionalized surfaces for biosensor and heterocatalysis applications, as well as for specific applications in drug design based on the biologically relevant G quartets [117].

3.4 Cytosine on Au(111)

Experimental microscopic imaging methods are required if one wants to improve our present understanding on the structure of amorphous materials. Non-symmetrical organic molecules adsorbed on solid surfaces may assemble into random networks, thereby providing us with model systems for organic glasses that can be directly observed by scanning tunneling microscopy (STM). Here we report on the structure of the disordered cytosine (C) network on the Au(111) surface, created by thermal quenching of the 2D fluid present on the surface at room temperature, to temperatures below 150 K. Comparison of STM images to density functional theory (DFT) calculations allows us to identify three elementary structural motifs (zigzag filaments and five- and six-membered rings) that underlie the whole supramolecular random network. The identification of elementary structural motifs may provide a new framework to understand medium-range order in amorphous and glassy systems.

3.4.1 Introduction

The microscopic description of glasses and amorphous solids is in general very challenging due to the lack of long-range order in their structure [118]. The structure of amorphous solids has traditionally been studied by space-averaging diffraction techniques, which provided a very detailed description of such materials on the macroscopic scale [118,119]. However, much less is known about the local structure of such disordered solids. Important breakthroughs in this respect came from optical microscopy studies of colloidal glasses [120,121]. However, due to the non-scalable behavior of the energy-relaxation processes with particle size, many details of how the molecular glasses persist and the dynamics of the glass transition cannot be answered with these model systems [121].

Organic molecules with the ability to form hydrogen bonds via peripheral functional groups that may be distributed in a highly anisotropic way have the potential to organize in random arrangements when deposited on atomically flat solid surfaces. The structure and dynamics of such systems can be addressed by scanning probe techniques at the molecular level [49,97,122] (provided the adsorption geometry is planar); thereby they have the potential to become a model system for studies on the structure of amorphous solids. In principle, the realization of such disordered systems also requires that molecule-surface interactions are much weaker than molecule-molecule interactions: if the molecules had an ability to arrange themselves in the gas phase in planar disordered structures, a strong interaction of the molecules with the surface would force them to form well-ordered structures controlled by the surface periodicity. The formation of a planar network is exemplified by the case of guanine (G) on Au(111) [66]: in this case, G self-assembles into a network of G quartets as determined almost entirely by hydrogen-bonding between the adsorbates, the role of the surface being only that of promoting planarity, as the corrugation of the potential energy surface is rather flat. However, the symmetry of the functional groups around the G molecules enables ordered networks to be formed.

Here we have studied the molecular-scale self-assembly of a cytosine (C) network on the Au (111) surface in real-space using STM and found that a supramolecular network forms which, unlike the previously reported case of a G structure, lacks long-range order. DNA base molecules adsorb weakly on noble metal surfaces, with an adsorption

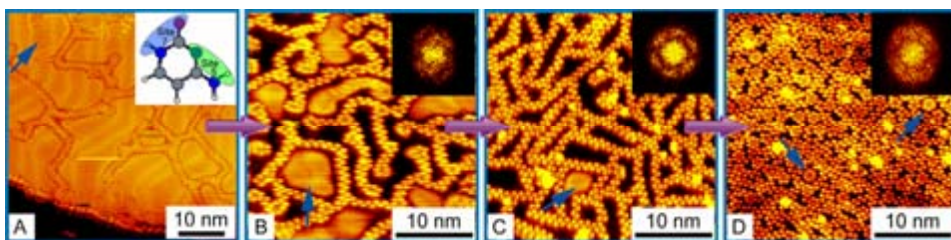


Figure 3.11: STM images of cytosine structures with increasing surface coverage (the pink arrows). Inset to (A): The most important binding sites which are used to form double hydrogen bonds between cytosine molecules. Blue arrows indicate mobile C zigzag branches (A) and C molecules or clusters trapped in nano-cages that appear as blurs (B, C). At higher coverages the blurs remind moving 5- or 6-fold rings (D). Scanning conditions: (A): $I_t = -0.5$ nA, $V_t = -1767$ mV (B): $I_t = -0.3$ nA, $V_t = -1767$ mV (C): $I_t = -0.7$ nA, $V_t = -1250$ mV (D): $I_t = -0.2$ nA, $V_t = -1250$ mV.

potential-energy surface displaying a small corrugation and a weak molecule-substrate charge transfer [7,58,64,66]. Experimentally we find that the C molecules are sufficiently mobile on the Au(111) surface, thus the molecular layer can be considered as a 2D fluid at room temperature (RT). Previous theoretical studies indicate that, due to the large number of hydrogen-bond donor and acceptor groups with which C is provided, a relatively large number of stable C-C dimer configurations could form involving double hydrogen bonds between groups of neighboring peripheral functionalities (or “binding sites”, see inset in Fig. 3.11A) [81]. The multiplicity of the strongest C-C dimer states with similar binding energies and the non-symmetrical distribution of the corresponding binding sites over the periphery of the molecules suggest that intermolecular interactions alone might direct the growth of disordered structures. Indeed, our STM results reveal that the 2D fluid of mobile C molecules found at RT, when quenched to low temperatures at a cooling rate of about 20 K/min on average, assembles into disordered structures, thus behaving like a 2D glass.

3.4.2 Results and discussion

When a sub-monolayer coverage of C molecules was deposited (at 390 K) on Au(111) at RT and the sample was imaged by STM at temperatures ≥ 180 K, no individual C molecules are observed because of their high mobility. Instead a noisy appearance or strikes is observed in the STM signal, the origin of which is associated with mobile C molecules diffusing much faster under the STM tip than the average STM scanning time [123,124]. We refer to this state as a 2D fluid. A series of STM images recorded at low temperatures (120-150 K) for increasing coverages on the surface is shown in Fig. 3.11. Near 1 ML the observed C structure is clearly disordered (Fig. 3.11D) with no long-range periodicity and the C structure thus represents an amorphous 2D system. This long-range disorder is reflected in its fast-Fourier transform (FFT) shown in the inset of Fig. 3.11D, which reveals only a bright rim corresponding roughly to a constant first neighbors distance. This short-range order is characteristic of most covalent and metallic glasses, thus indicating that the amorphous structure depicted in Fig. 3.11D can be described as a 2D glass.

The lack of long-range order is also apparent at lower C coverages (Figs. 3.11A to C), although a slight anisotropy in the intensity distribution of the FFT of the STM images

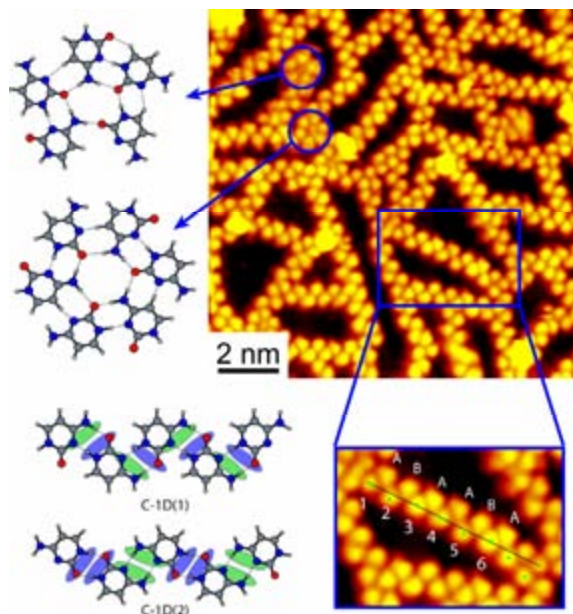


Figure 3.12: Three elementary structural motifs (filaments, 5- and 6-fold rings) are compared with the theoretical models. The color coding in the filament models (see inset in Fig. 3.11A) indicates the binding sites 5 and 7 involved in the two filaments, and this also helps to recognize the chirality of the molecules. The enlarged image shows that the seemingly straight filaments have no translational periodicity. The non-circular shapes of the molecules which are clearly not tip artefacts (molecules A are mirror-images of B) can be recognized in the high-resolution STM images. A line connecting the centres (indicated by green dots) of molecules 1 and 6 is used as a reference. It clearly shows that molecules 1, 3, 4, 6 binding to molecules A are centred along the reference line, whereas molecules 2, 5 binding to molecules B are off the reference line. Thus, it strongly suggests that the dimers 1-A, 3-A, 4-A, 6-A should be different from dimers 2-B, 5-B, indicating that the filament changes its structure after 2-3 dimers. Scanning condition: $I_t = -0.7$ nA, $V_t = -1250$ mV.

along the high-symmetry directions of the gold substrate seems to indicate a small but measurable templating effect of the substrate on the molecular arrangement. For low C coverages (below 0.5 ML), diffusion dynamics of the C molecules and supramolecular clusters is revealed even at 100 K. First, time-lapsed STM movies recorded with the fast-scanning Aarhus STM reveal rearrangements of the different structural elements with respect to each other. Some of the C structures appear as blurred protrusions in the STM images and cannot be resolved into their molecular constituents. In Figs. 3.11B to D these blurred protrusions can be found in the “nano-cages” between randomly oriented C filaments. STM movie shows that the C related protrusions may move in and out of the “nano-cages” if manipulation with the STM tip breaks one of its “walls.” Upon subsequent increase of the C coverage, the number of the blurred protrusions decreases, and these initially featureless blurred protrusions (see Fig. 3.11B, where one example is indicated by blue arrow) begin to display some internal structure, first appearing like a “doughnut” (Fig. 3.11C, indicated by blue arrow), and subsequently like blurred 5- and 6-fold rings (Fig. 3.11D, indicated by blue arrows). These findings suggest that the

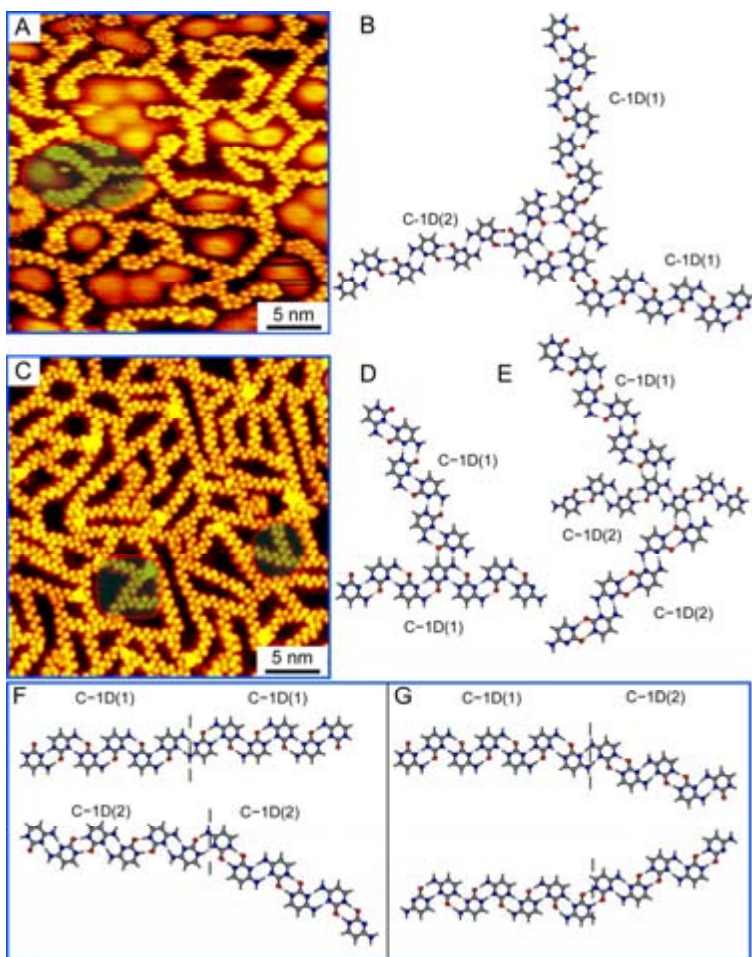


Figure 3.13: STM image in (A) and a theoretically predicted structure in (B) show the connections between C filaments and 6-fold rings in a “roundabout” fashion. STM image in (C) shows the C filaments linked together mainly via T- and bending junctions. The corresponding theoretically predicted structures are shown in (D) to (G), respectively. Examples of “roundabout” and T-junction motifs have been highlighted in (A) and (C), respectively. Scanning conditions: (A): $I_t = -0.4$ nA, $V_t = -1051$ mV (C): $I_t = -0.7$ nA, $V_t = -1250$ mV

blurred structures correspond to mobile C molecules or clusters enclosed in the “nanocages” of the random C network, unable to attach to it.

A thorough and detailed analysis of the STM images obtained for a coverage below 1 ML reveals that every C molecule belongs to at least one of the following three structural units: (i) zig-zag filaments, (ii) 5-fold rings and (iii) 6-fold rings (see Fig. 3.12). Over 200 images were analyzed for more than five different coverages, and for each coverage at least 20 images were examined. Thus, for our model system, the problem of describing this disordered structure can be reduced to the much simpler problem of understanding how these three elementary structural motifs link together.

In order to further characterize the structure of the random C network, we have performed *ab initio* density functional theory (DFT) calculations. The minimum-energy configurations for C molecules with geometries similar to the zigzag chains, and the 5- and 6-fold rings revealed in the STM images are shown in Fig. 3.12. By systematically attaching molecules to each other in all possible ways [81], several configurations with very similar binding energies were found for all three structures. The two most stable models for the periodic zigzag filaments, obtained by assuming that the unit cell is composed of two C molecules (that is, a C-C dimer), are denoted C-1D(1) and C-1D(2) respectively. The calculated binding energies of about 0.9 eV/molecule for these two structures are very similar and significantly larger than the ones obtained for 5- and 6-fold C rings (0.6 eV/molecule), in good agreement with the experimental finding that the filaments are the most common structure observed in the STM images. Since the stabilization energies of the two filamentary structures C-1D(1) and C-1D(2) corresponding to the same motif are very similar, we assume that all of them do co-exist in the random cytosine network, and their very similar geometry makes them indistinguishable by STM. From the calculations we find that the interaction with the gold surface is much weaker (adsorption energy found to be 0.1 eV) than the identified intermolecular hydrogen bonding strength between the C molecules. Although there is a weak indication in the FFT images of a preferential alignment of the filaments along the symmetry directions of the gold surface (Fig. 3.11C), this effect is much smaller as compared to the much stronger hydrogen bonding driving the assembly of C molecules.

Next, we addressed how these different elementary structural motifs interconnect with each other to form the disordered cytosine networks. The ends of the two stable finite filament segments (shown in Fig. 3.12) exhibit a number of exposed hydrogen-bonding groups, i.e. they are “sticky”, whereas the peripheral functional groups exposed on the sides of the filaments are mostly non-polar and thus less prone to form stable bonds to neighboring C molecules. Correspondingly, we never observed a “bare” filament termination. As shown in Figs. 3.13A and C, the filaments are always linked to some other filament through 6-fold ring or in a T-junction fashion (possible models for which are displayed in Figs. 3.13B, D, and E). Similarly, the “sticky ends” of any two filaments can join head-to-tail resulting in either bent or linear filament structures (Figs. 3.13F and G). Our STM images show that indeed most of the observed filaments which are longer than two to three dimers quite often are bent (Fig. 3.13C). Furthermore, our high-resolution STM images reveal a change in the shape of molecules (marked as A and B in the enlarged STM image in Fig. 3.12) along straight filaments in positions that would be equivalent if there was translational periodicity. This indicates that these molecules A and B do not have the same orientation, and thus translational periodicity only appears over two to three dimer distances along the filaments.

Figs. 3.13A and B depict experimentally and theoretically, respectively, how the “sticky ends” of cytosine filaments can link together through the 6-fold ring in a “roundabout” fashion. As in the case of 5- and 6-fold ring formations, the bonds involved in the interconnections among the different elementary structural motifs will be weaker than those involved in the stabilization of the C-1D structures. On the other hand, the “non-sticky” nature of the filament side-borders makes it difficult for molecules or molecular clusters trapped inside “nano-cages” to attach to their “walls”, and thus they diffuse fast in the enclosed regions (they appear as blurred protrusions in the STM images discussed above). Thus, by connecting and combining the three elementary structural motifs in the fairly small number of ways just described, the C structures

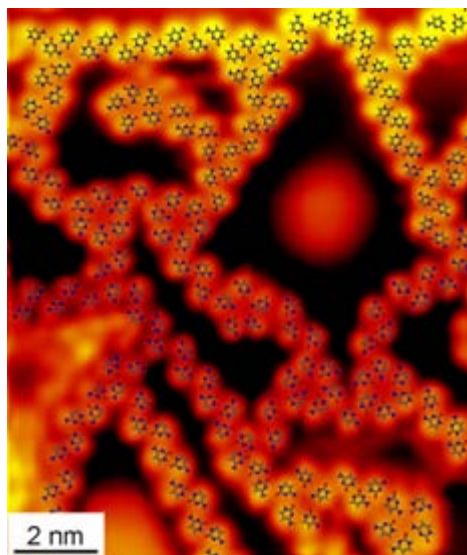


Figure 3.14: STM image of a ‘glassy state’ of cytosine on Au(111) with an overlay illustrating that a few elementary hydrogen-bonded structural motifs and their possible connections explain the image. Scanning condition: $I_t = -0.15$ nA, $V_t = -1767$ mV.

observed in the STM images can be explicitly characterized, and an example of this is shown in Fig. 3.14.

Previous STM experiments performed in an electrochemical environment [125] reveal that there exists another structure for the system C/Au(111) in which ordered arrays of zigzag filaments of C molecules lie parallel to each other bound by weak van der Waals (vdW) forces acting between non-polar (non-sticky) areas of the filaments. Note that in this arrangement each molecule is also hydrogen bonded to other two molecules along the filament, but it also interacts with two molecules of the neighboring filaments through vdW interactions. In the random network we observe, only hydrogen bonding is involved and the majority of the C molecules are bound to only two neighbors through hydrogen bonding. Hence, because of an additional vdW interaction, in relatively large islands of parallel C filaments, the binding energy per molecule will be greater than in a random network containing the same number of molecules, ensuring that the ordered arrangement has the lowest energy, and it thus serves as the 2D cytosine ground state.

As crystalline islands can only survive if they are larger than some critical size, kinetically their formation is highly unlikely. Indeed, upon fast cooling the formation rate of a large stable crystalline nucleus cannot compete with the formation rate of much smaller structures such as 5- and 6-fold rings, roundabouts and T junctions, which are energetically the most stable clusters containing small numbers of C molecules, and the system gets trapped in a random network during the first stage of the kinetic process of assembly formation. Thus, this kinetic process leads to a dynamical capture of the 2D fluid upon fast cooling, when the available thermal energy in the system becomes insufficient to facilitate escape from the local order of the liquid state into the ground crystalline state.

3.4.3 Conclusion

As a result we can conclude that in spite of the lack of periodicity in the random cytosine network, we have revealed that only a few elementary structural motifs exist through which C molecules bind to each other, and yet very complex structures can be formed from these structural building blocks. The present cytosine model system is kinetically trapped in a disordered state, in a similar way as a glass is trapped in the amorphous state, since it would need to overcome prohibitively large energy barriers to move away from it. Examples of glass-forming systems where the constituents are molecules that can form hydrogen bonds in one of their ends, but interact only weakly through the other parts, such as for example ethanol, are known in the literature [126]. The results presented here may reveal an interesting route for studying the structure of organic glasses, by performing a systematic search of particularly stable motifs and their possible interconnections. The structure we describe here is similar to a Continuous Random Network, where the constituents of the network are not individual atoms or molecules, but they rather consist of a small number of supramolecular elementary motifs, some of which present medium-range order. The identification of such structural motifs would not have been possible without the proper choice of a model system and the application of the STM technique to reveal the nano-scale order.

3.5 Cytosine+Guanine and Cytosine+Adenine on Au(111)

Molecular recognition between complementary nucleic acid (NA) bases is vital for the replication and transcription of genetic information, especially under prebiotic conditions, in which the dedicated molecular machinery of evolved living organisms was not yet developed to any extent [127,128]. Therefore, it is of utmost fundamental interest to investigate this recognition process under mimic prebiotic conditions in order to explore how life could possibly emerged under conditions other than those present on Earth today. Here we show that molecular recognition does indeed occur between individual NA bases adsorbed on a solid surface such as Au(111) under extremely clean ultra-high vacuum (UHV) conditions, that is, even in the absence of any solvents and salts. We demonstrate by variable-temperature Scanning Tunneling Microscopy (VT-STM) that binary mixtures of the complementary bases guanine (G) and cytosine (C) on the surface are stable towards thermal treatments up to their desorption temperature, while mixtures of the non-complementary bases adenine (A) and cytosine (C) segregate upon gentle annealing. From a thorough analysis of our STM images and an interplay with state-of-the-art *ab initio* Density Functional Theory (DFT) calculations we conclude that G could indeed recognize its complementary partner C and the complementary mixture's resilience is due to the formation of embedded Watson-Crick pairs between adsorbed G and C molecules. These results show that the presence of the solid surface can help the recognition of NA base molecules by keeping the molecules in a flat configuration and reducing the possibilities in phase space which trap the molecules in 2D and easily steered by directional H-bonding, but at the same time the efficiency of the recognition process is very sensitive to growth conditions. Such conditions must then be closely mimicked by any experiment aimed to understand the origin of the first self-replicating molecules.

3.5.1 Introduction

Ever since the fascinating double helix structure of DNA was discovered by Watson and Crick fifty years ago [129], upon which a simple set of base pairing rules were proposed for the four NA bases guanine (G), cytosine (C), adenine (A) and thymine (T), the complementarities between the patterns of hydrogen-bonded donors and acceptors in the A-T and G-C pairs has been found to play a crucial role in the fidelity with which DNA is replicated [129], since it would impose an enthalpy penalty to form double stranded DNA from error-containing strands. However, experimental evidence has proven that several DNA polymerase enzymes can efficiently incorporate non-natural nucleotides containing synthetic bases without the capability of forming hydrogen-bonds, but with a shape that closely mimics that of the natural nucleobases [130]. Hydrogen-bonding is thus *a priori* not necessary for a high-fidelity replication of DNA in evolved organisms. An important fundamental question to address is thus: Why would the base pairs A-T and G-C contain complementary hydrogen-bonding groups, as if they were necessary for replication when they are not? One possible answer is that they might indeed have been necessary to attain some degree of fidelity in the replication of the first self-replicating molecules in the prebiotic soup on Earth, when the elaborated molecular machinery of modern living organisms had not yet fully evolved [127]. It has been shown that short RNA strands can act as templates, catalyzing the polymerization of complementary RNA strands from activated nucleotides in solution. The reaction, though, proceeds slowly and

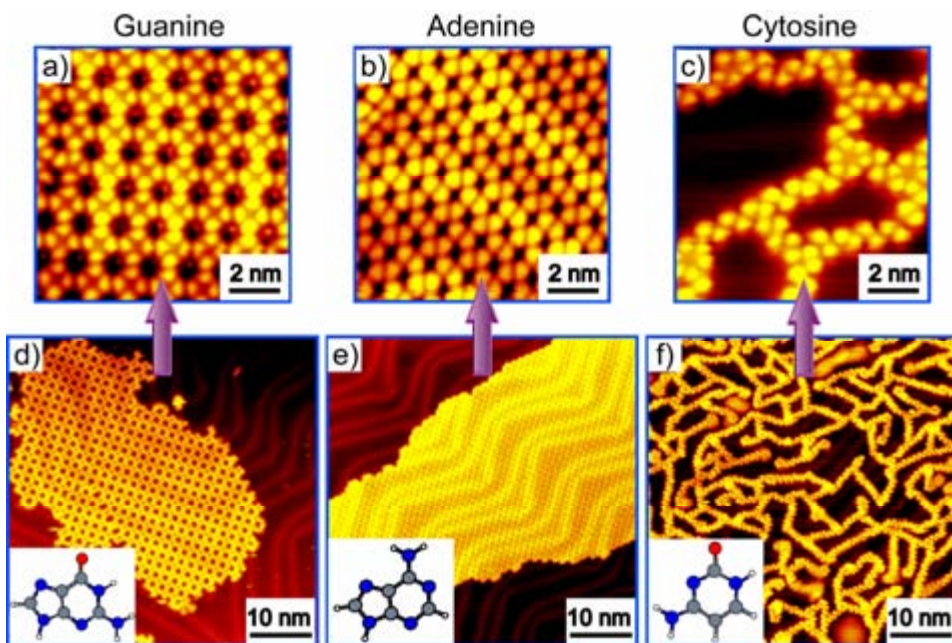


Figure 3.15: STM images of single DNA bases deposited on Au(111) at RT. Guanine (a, d) and adenine (b, e) show 2D island growth. The herringbone reconstruction, known from clean Au(111) can clearly be seen as modulation on the top of the purine structures, indicating weak interaction between the substrate and the molecules. Cytosine (c, f) grows into 1D filaments consisting of zigzag branches and ring-like structures. Blurs in areas that are confined by branches are due to mobile C molecules. The insets show the chemical structure of the molecules with O, N, C and H atoms shown as red, blue, grey and small white circles. All images are acquired in constant current mode $I_t = -0.3-0.7$ nA, $V_t = -800-1500$ mV.

the replication process is rather unfaithful [127]. This is however not very surprising in view of the small free energy gain associated with complementary binding of the nucleotides in solution [131], which involves the breaking of hydrogen-bonds between the nucleobases and the water molecules of the solvent (which is energetically costly) and the loss of freedom for the nucleobase dimer, as compared with the solvated bases (entropically costly) [130].

It has been proposed that surfaces of solid minerals and graphite grains [132] might have played a major role in the evolution of prebiotic molecules and acted as catalysts to enhance the RNA replication fidelity and the reaction rate [128], but the detailed role of the solid surface in molecular recognition between complementary nucleobases has not yet been thoroughly addressed. Here we use variable-temperature STM and DFT calculations to investigate the feasibility of molecular recognition in complementary G-C system as compared with the non-complementary A-C system using the inert Au(111) surface as a model substrate.

3.5.2 Results and discussion

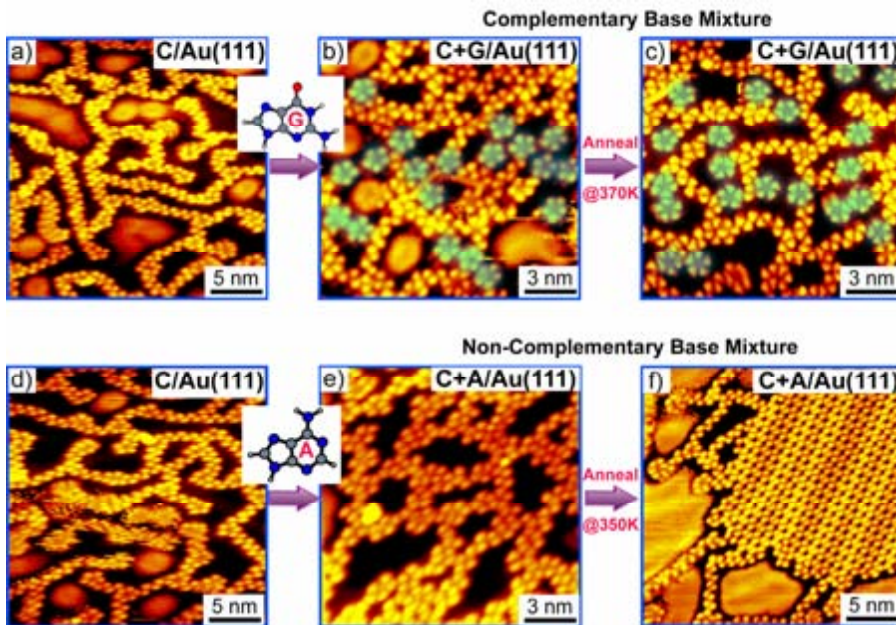


Figure 3.16: Co-deposition experiment for complementary C+G (a-c) and non-complementary C+A (d-f) bases. During the first step, similar amounts of C were deposited at RT in each case (a, d). After deposition of G (b) a sharp increase in the number of 5-fold rings is found (indicated by the green shadows), which was not observed after deposition of A (e). C+G as well as C+A mix upon co-deposition (b, e). After annealing the complementary C+G mixture remains disordered binary phase (c), while the non-complementary C+A mixture segregates into A islands and C zigzag branches (f).

Prior to the studies of NA base complementarities, we first studied the adsorption of single individual bases. In Fig. 3.15 we show three representative STM images of the molecular networks formed by depositing G (Figs. 3.15a and d), A (Figs. 3.15b and e) and C (Figs. 3.15c and f) molecules on the Au (111) surface held at room temperature (RT). The STM images were recorded at 100-150 K to prevent undesired diffusion events and to enhance the tunneling junction stability. The corrugation of the potential energy landscape for adsorbed NA bases is small enough to enable molecules to move around to form the observed self-assembled molecular networks. The molecular assembly, thus, arises from the hydrogen-bonding between the peripheral functional groups of the NA base molecules, consistent with previous studies for G [66], C [69], T [68] and A networks [133] on Au(111) and on other different substrates [7,58,64,134]. NA base molecules adsorbed on noble-metal (111) surfaces are found to adopt a flat-lying geometry in which the rings in the molecular backbone are parallel to the substrate surface [58,66,68,69,133].

For the G and A (purine) molecules the STM images clearly depict the formation of self-assembled two-dimensional (2D) well-ordered structures (Figs. 3.15a and b). The submolecular-scale structures of the molecular networks for both molecules are clearly resolved and the molecular structures are easily distinguishable from each other in the STM images. For the guanine case, G molecules self-assemble into a hydrogen-bonded network of G-quartets similar to those found in G-quadruplex DNA [66]. For the case of

A, we observe a self-assembled molecular structure very similar (but not exactly the same [133]) to that obtained after depositing A molecules on Cu(111) [58], Ag/Si(111) [64] or graphite [134].

On the contrary, the C molecules do not initially nucleate and grow in 2D self-assembled islands (Fig. 3.15c). At low coverages (below 0.25 ML), we are not able to image the C molecules on Au (111) even when the STM is held at low temperature (100 K), due to the very high mobility of individual C molecules and small C clusters. However, for coverages above 0.25 ML, the C molecules form a disordered molecular network of interconnected 1D zigzag filaments interconnected by 5- and 6-fold rings. Similar branches consisting of double molecular rows have been reported for C deposited on Cu(111), although an exact comparison is hampered by the lack of molecular resolution in that study [58]. Even at higher C coverages, we still observe some diffusion and rearrangements of the hydrogen-bonded C molecules within the C network structures. In the areas enclosed by several C branches, “blurred” ring-shaped structures are observed, which are attributed to mobile C molecules or clusters confined in such nano-cages. The details of this interesting C structure which has glassy-like behaviour were recently discussed in a separate publication [69].

Once we have identified and characterized the adsorption structures of the individual single NA bases, we proceed to perform the co-deposition experiments of the binary mixtures. First we deposited the C molecules at RT which resulted in the mobile and open filament type network we described above, and determined the C coverage with the STM. In the second step either the complementary base (G) or the non-complementary base (A) were deposited onto the surface (held at RT), already partially covered by C molecules, and subsequently imaged both samples with the STM at low temperature. Finally, the samples were annealed at a temperature lower than the lowest desorption temperature of the three bases for 10-15 min and the surfaces were subsequently imaged at low temperature again.

STM images of such a deposition-annealing sequence are shown in Figs. 3.16a-c for C+G and d-f for C+A, respectively. In the shown experiment we deposited comparable amounts of C in the first step (Figs. 3.16a and d), and obtained comparable total coverage after deposition of the second base (C+G or C+A in Figs. 3.16b and e, respectively). In Fig. 3.16a and d the typical C structure with zigzag branches and ring-like structures is observed. After deposition of the purine molecules (G or A), the structures for both binary mixtures are observed to have a similar appearance in the STM images (Figs. 3.16b and e), similar to the pure C structure (Figs. 3.16a and d). The only difference that can be straightforwardly noticed is a dramatic increase in the number of five-fold rings upon G deposition (Fig. 3.16b, indicated in green), that is not observed upon A deposition (Fig. 3.16e). It can be stated that upon deposition at RT both purine molecules (G and A) get incorporated into the pre-existing C network (see below the detailed analysis of this), and thus both G-C and A-C pairs must exist.

However, dramatic differences are observed after annealing the binary mixtures at temperatures slightly below the lowest desorption temperature of the pure bases. In the case of C+G annealed to 373 K for 10 min, the structure remains the same as before annealing, the only noticeable difference being that the blurred mobile molecules have disappeared (the imaged region in Fig. 3.16c is typical). The binary structure of C+G is thus stable during annealing. Further annealing treatments at higher temperatures (400 K), however, lead to desorption of the C molecules, and only the pure G molecules are left on the surface. On the contrary, in the case of C+A after annealing to 353 K for 10 min, we mainly find large islands which can be associated with the self-assembled

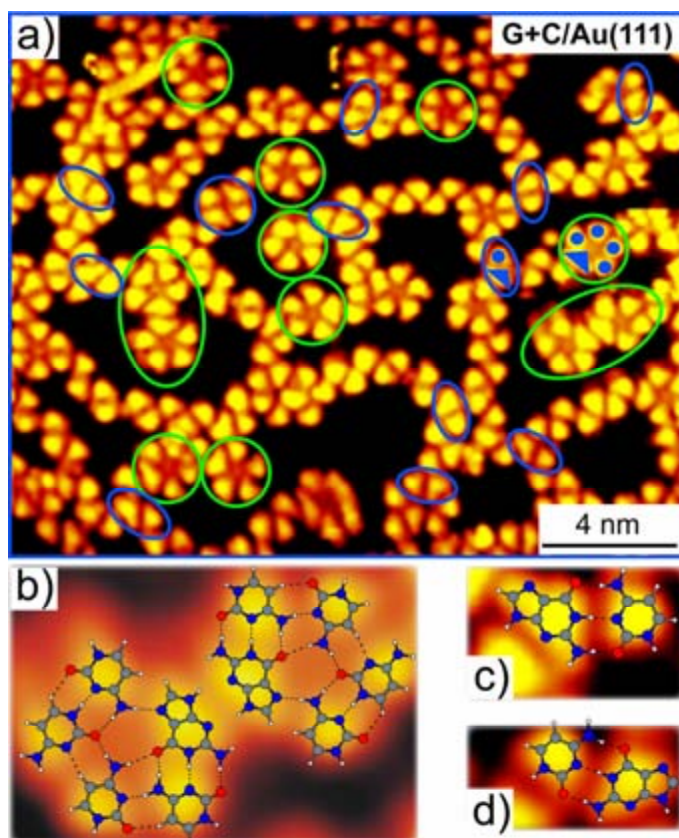


Figure 3.17: (a) High-resolution STM image of the complementary C+G structure after annealing. The blue circles indicate G-C dimers involved in filamentary structures and the green circles indicate five-fold rings containing G-C dimers. The blue triangles indicate G, while the blue balls indicate C molecules, respectively. (b) The enlarged image showing two 5-fold rings both containing one G-C Watson-Crick base pair. The superimposed structures are the relaxed minimum-energy DFT calculated geometries, which fit quite well to the experimental STM image. (c, d) The enlarged STM images show two G-C dimers with different chiralities, which are superimposed by the calculated G-C Watson-Crick base pair dimer structure.

structure of pure A and zigzag-branches of pure C, i.e. the binary mixture of non-complementary bases segregated into pure A and pure C domains (Fig. 3.16f). These experiments have been systematically performed with varying amounts of C, G and A resulting in the same qualitative results.

The random network created by the C molecules contains a considerable amount of empty space: in nanocages within C-islands (due to the molecules being mostly connected only to two neighbours) and between C-islands. This means that a lot of C binding sites are not used. The deposited G (or A) get into these empty spaces and connect to the C molecules resulting in their incorporation into the C network. Upon annealing, two processes are possible: (i) the initial network is completely disintegrated and then reformed thanks to high mobility of the molecules, or (ii) only the weakest pairs are broken, the strong pairings between the molecules survive and serve as precursors of

the new formation during annealing. In either case of the C+G and C+A mixtures, complete disintegration of the initial random-network structures (in which molecules are mostly bound to two neighbours) would result in their segregation since both G and A molecules, highly mobile at annealing temperature, will first form highly stable network structures in which every molecule is hydrogen-bonded to three neighbours. Although entropically it is more advantageous to keep the mixture, the temperature is not high enough to make this factor dominant. The fact that the C+G mixture, based on complementary bases, remains disordered upon annealing suggests that this scenario does not work in this case. This leads to the conclusion that the interaction in C-G pairs must be much stronger than that in C-C and G-G pairs (and thus the second scenario). However, the first scenario must be at work in the case of the C+A mixture formed by non-complementary pairs, since it segregates. Since it is thus possible to induce segregation of the non-complementary mixture by thermal annealing whereas the complementary mixture is “resistant” to annealing, we conclude that by gentle thermal treatments it is possible to induce C to somehow recognize its complementary partner G.

To obtain a more detailed understanding of the enhanced stability of C+G mixtures after annealing, we further analyzed the images of the mixture of the complementary bases. A thorough analysis of the high-resolution STM images reveals two different kinds of molecules in the observed C+G mixtures, some of them appearing in the STM images as larger, elongated triangular protrusions, whereas some of them as small equilateral triangles, which can be clearly distinguished in Fig. 3.17a. The apparent larger triangular molecules are found to be incorporated in the filament structures, basically forming a local dimer structure with one of the small molecules, and they are also very common in the five-fold rings (as indicated in Fig. 3.17a). Many of these consist of one larger triangular molecule and four smaller molecules that close the five-fold ring. In a previously reported experimental and theoretical study on the adsorption of G on Au (111) [66] it was shown that the G molecules, adsorbed in a flat adsorption geometry on the surface, indeed appear as such larger triangular protrusions in the STM images. We thus conclude that most of the five-fold rings of C+G mixtures are composed of one G molecule with an orientation that can be deduced from the shape of the triangle and four C molecules. A similar analysis also reveals that the G-C pairs exist in the filament structures as well (see, e.g. Fig. 3.17a), i.e. G and C molecules are intermixed in the final structure. In the same way, we have also convinced ourselves that G and C molecules are incorporated in the initial mixture formed upon co-deposition before the annealing.

To obtain further fundamental insight into the atomic-scale structures of the C+G mixture, several models were proposed based on the criterion of maximizing the number of hydrogen bonds in the structures. The starting point in the analysis is the Watson-Crick (WC) C-G base pair (with the stabilization energy of -1.21 eV [82,83,135,136]), which has the highest stability among all NA bases [82,83]. In comparison, the three most stable C-C pairs have binding energies ranging between -0.87 and -0.99 eV [81], which are considerably lower than for the WC pair. Note, that they all use different binding sites of C to those of the WC pair and thus will not compete with it during the growth. However, the most stable G-G pair (with the rather high binding energy of -1.12 eV, other pairs have much lower stabilities) would be hindered by the WC pair, as both use the same binding site of G. Thus, there must be G-G pairs present in the observed structures as well, alongside the WC G-C pairs. C and G molecules in the final structure will bridge these pairs.

Using the WC pair as the main building block, we constructed a molecular model for the five-fold ring containing a single G and four C molecules. The DFT relaxed structures of the rings, together with the WC pair, are shown in Figs. 3.17b, c and d superimposed on the STM images. We find that both the proposed five-fold ring and the G-C dimer structure fit very well with features observed in the STM images of the C+G mixture. Hence, we propose that most of the observed elementary structures contain at least one WC G-C base pair. This observation offers an explanation for the enhanced stability of C+G mixtures with respect to the pure G and C structures.

For a relatively large range of temperatures, the Watson-Crick pairs constitute the smallest stable structures that can be formed in a C+G mixture. Once a G-C Watson-Crick pair is formed, it will not break easily, thus preventing the segregation of G and C molecules. Formation of isolated G-C and G-G pairs had already been observed in gas-phase, but the binding selectivity was not discussed [137].

In the case of the non-complementary mixture C+A, the binding energies for the most stable C-A pairs (between -0.75 and -0.88 eV) are slightly smaller than or comparable with the most stable C-C (-0.99 eV) and A-A (-0.86 eV) pairs [79]. In this case upon annealing all pairings must be broken, and the whole network completely disintegrated (and thus the second scenario discussed above). Since A can form highly stable hexagonal 2D islands with no extra space between the molecules, these islands form first. The C molecules present around have no choice but to connect with themselves in filaments and attach to the A islands boundaries as observed experimentally.

3.5.3 Conclusion

In conclusion, from an interplay of STM imaging and DFT calculations we have shown that the recognition between complementary NA base molecules adsorbed on solid surfaces is indeed feasible, and that the relatively small energy difference between A-C and G-C pairs allows us to choose a temperature range in which C binds preferentially to its complementary partner G and not to the non-complementary partner A. This recognition is helped by the balance between molecule-molecule interactions and the constraints to the molecules' ability to move in 3D space that is set by the surface, which restricts molecules' mobility (both translational and rotational) to the two-dimensional above-the-surface phase space. This suggests that solid surfaces can indeed play an active role in catalyzing RNA polymerization with replication accuracy. The recognition process takes place here in the absence of water, a NA backbone or enzymes: it is simply driven by the energy difference between hydrogen bonded A-C and G-C dimers, and the temperature. The experiment outlined here fixes the minimum conditions under which a high-fidelity, hydrogen-bond directed, replication would be energetically advantageous. In this respect it constitutes a minimum benchmark experiment to compare with for more realistic experiments in which for example, the role of backbone stiffness and conformational freedom, solvents and other biochemical environment must all be taken into account.

3.6 Guanine and K^+ on Au(111)

3.6.1 Introduction

Human telomeric DNA with stretches of guanines folds into G-quadruplexes made of stacking of G-quartets, have been demonstrated to be promising targets for designing novel anti-cancer agents and potentially for controlling gene expression [138,139]. The so-called G-quartet motif is a hydrogen-bonded ionophore [140], which has intrigued fundamental interest ranging from the areas of structural biology, biophysics, supramolecular chemistry, medicine and recently to nanotechnology. To date a number of studies have been performed experimentally and theoretically to reveal the detailed conformations, hence the physicochemical nature of the G-quartet related structures both on solid surfaces and in solutions [141-143]. In particular, our group first reported the formation of G-quartet network by guanine molecules alone on Au(111) surface under ultrahigh vacuum (UHV) conditions [66]. As important cautions in cellular environments, K^+ (and Na^+) templated G-quartet motifs have been an extensive research subject in structural biology and biochemistry, mostly studied in 3D solution phase by various spectroscopic techniques [144-148]. Meanwhile the crystal structures of a number of lipophilic G-quadruplexes have been solved [149-153]. In order to simplify and get further insight into the studied system, we have performed experiments that go on step further when incorporation of K ions with guanine molecules has been investigated by high-resolution Scanning Tunneling Microscopy (STM) under UHV conditions. This unambiguously provides the real-space morphologies of different 2D nanoporous G-quartet based metallosupramolecular networks coordinated with K^+ for the first time.

Nanoporous networks were reported to be formed on surfaces either by molecular building blocks themselves via hydrogen bond, van der waals interactions or with the assistance of metal atoms [154-161]. Considering the great potential of patterning surfaces on nanotechnology, it is a challenging and critical subject to generate nanoporous networks with designed structures, e.g. controlling the size and the shape of the cavities of the networks. Note that the size and even the shape of the cavity in a porous network are always considered to be one of the important parameters in the studies of host-guest systems, and might need to be varied specifically from case to case to adopt different guest molecules. To achieve this goal is however, a technically difficult issue, which always involves complicated chemical synthesis to fabricate the potential molecular building blocks suitable for further self-assembly process through directional and selective hydrogen bond or metal-ligand coordination [155,157]. In this work, we have succeeded in creating different nanoporous networks by delicately changing the K^+ ratio exclusively. Interestingly, by increasing the K^+ ratio step by step, the size and the shape of the formed cavities can be controlled from square lattice ($a=10$ Å) over rectangular lattice ($a=10$ Å, $b=14$ Å), square lattice ($a=14$ Å) to rectangular lattice ($a=15$ Å, $b=18$ Å). In particular, at low K^+ ratio, a biologically relevant G-quartet network embedded with K^+ ion in the center of each G-quartet motif was found unambiguously in real space. All these metallosupramolecular networks are found to be stabilized by the interplay of hydrogen bond and metal-ligand coordination. This is particularly relevant for the bottom-up fabrication of surface patterning, which holds the ultimate goal of building desired nanostructures in a controlled manner from 2D to 3D. The identification of G-quartet motif embedded with K^+ in real space is of utmost

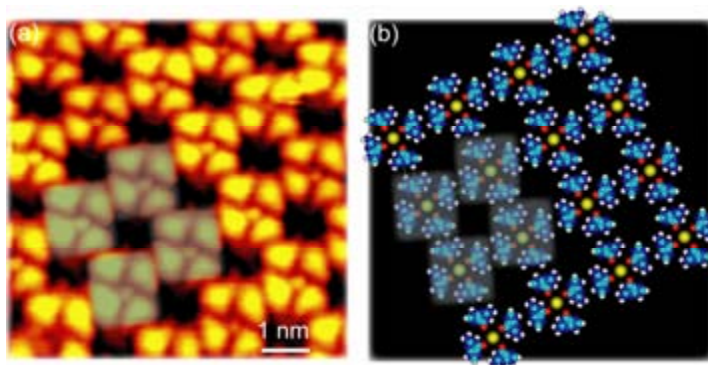


Figure 3.18: (a) High-resolution STM image of G-quartet network and K^+ complex with the ratio of $K:G=1:4$. (b) Tentative model for the observed metallosupramolecular network as shown in (a). In the model the K ions are presented by the yellow balls. The space-filled molecular model is used for guanine molecule, in which red is oxygen, dark blue is nitrogen, white is hydrogen, and light blue is carbon.

relevance for understanding the complex G-quadruplexes structures in biological systems, and thus helps to advance the strategy for anti-cancer drug design.

3.6.2 Results and discussion

To study the binary system of G molecules and K ions we first deposited G molecules onto a clean Au(111) substrate held at room temperature (RT). This resulted in the formation of G-quartet network, which is consistent with the previous work [66]. The K atoms were then subsequently deposited by thermal sublimation at 5.5-6.0 Å onto the surface covered by G-quartet networks at RT. It is reasonable to consider that K atoms become ionized to K^+ after deposition onto the surface. Fig. 3.18(a) shows the STM topography of the metallosupramolecular G-quartet network embedded with the K^+ in the center of each G-quartet motif (as referred to Phase I in the following) resulted from low K^+ dose. The G molecules are imaged as triangular protrusions and the central dot in each G-quartet motif represents the K^+ . It was experimentally and theoretically proved that the interaction between G molecule and Au(111) substrate is weak so that the self-assembly process is predominately steered by the intermolecular interaction i.e. hydrogen bond in this system [66]. It is clearly revealed by high-resolution STM images that in phase I one K^+ is bound by four G molecules (G-quartet) via metal-to-ligand bonding ($K:G=1:4$), and the inter- and intra-quartet hydrogen bonds link the metallosupramolecular G-quartet motifs into extend networks as observed in the experiment. In this case, the G-quartet network is still maintained and thus the hydrogen bonding pattern is assumed to be not much affected by the incorporation of K^+ as compared with the pure G-quartet network [66]. It was previously suggested that cation binding presumably reduces the repulsion of the four central oxygen atoms of the hydrogen-bonded quartet, thus enhances hydrogen-bond strength [140]. A proposed model of this metallosupramolecular network is shown in Fig. 3.18(b), in which two kinds of interactions that hydrogen bonding ($N-H\cdots O$, $N-H\cdots N$) and metal-to-ligand bonding ($K-O$) can be identified.

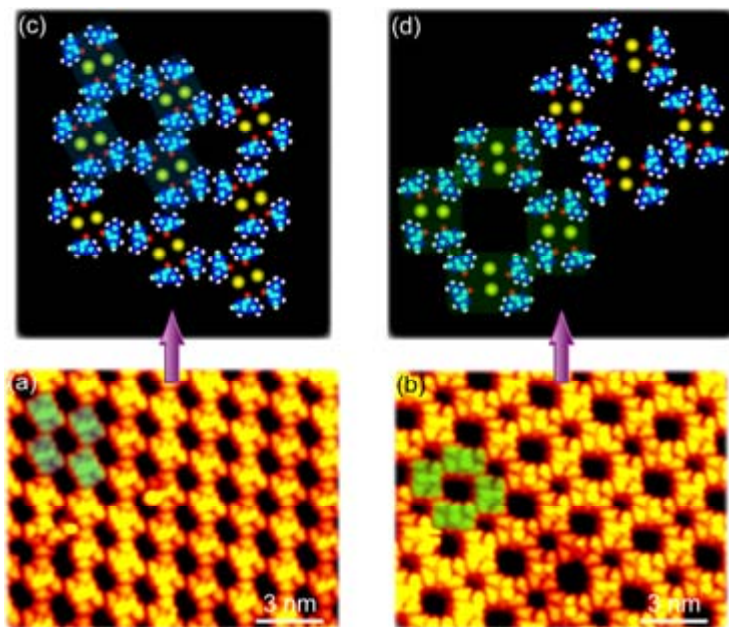


Figure 3.19: (a) and (b) High-resolution STM images of the coexisting metallosupramolecular networks of G and K^+ complex with the ratio of $K:G=1:2$. (c) and (d) Tentative models for the observed metallosupramolecular networks as shown in (a) and (b), respectively.

It is worth mentioning that this observed G-quartet motif embedded with K^+ is very relevant to the reported G-quadruplexes structures found in biological system. Also today the interest in G-quartet structures remains unabated. Numerous studies have shed light on the structure, conformational diversity and dynamics of the human telomeric G-quadruplexes by various techniques such as NMR spectroscopy, single-molecule fluorescence resonance energy transfer, electrospray mass spectrometric, and single-crystal X-ray [144-147,162]. But our study provides the first evidence in real space to reveal this biologically relevant metallosupramolecular G-quartet motif and thus reduced the complexity from 3D to 2D.

Interestingly, by delicately increasing the amount of K^+ dose, phase I is found to undergo a transition to another two coexisting metallosupramolecular networks (phase II and III) with the ratio of $K:G=1:2$. Figs. 3.19(a) and (b) display the high-resolution STM images of these two networks. In these two networks the trace of G-quartet motif can still be recognized, (cf. the highlighted rectangular units in the STM images). Though, in this case the G-quartet motif has been split away from square shape to rectangular shape mediated by two coordinated K ions. Fig. 3.19(a) shows that all the rectangular units orient along the same direction, which result in the homogeneous nanoporous network, whereas in Fig. 3.19(b) the rectangular units alternatively change the orientation resulting in the heterogeneous nanoporous network with two kinds of cavities. The proposed models shown in Figs. 3.19(c) and (d) elucidate that two pairs of intra-quartet double hydrogen bonds ($N-H\cdots O$, $N-H\cdots N$) are obviously broken, which could be a result of the competition between hydrogen bonding and metal-ligand interaction. Meanwhile, the G-quartet shape is still kept by the coordination of two K ions resulting

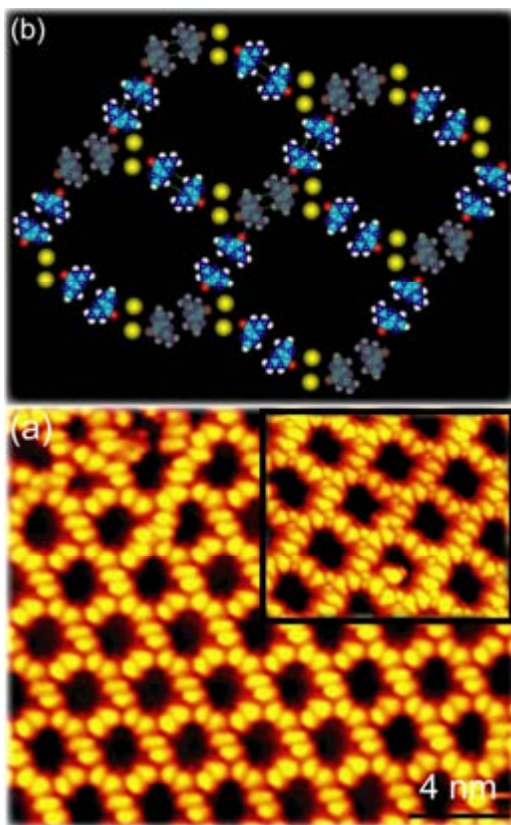


Figure 3.20: (a) High-resolution STM image of the metallosupramolecular network of G and K^+ complex with the ratio of $K:G=2:3$. The inset shows that the K^+ can be clearly distinguished with good tip condition. (b) Tentative model for the observed network as shown in (a). Different colour codings indicate different chiralities of G molecules.

in new metal-ligand coordination motif (cf. the above-mentioned rectangular unit) based on G-quartet motif. The inter-linkages between those rectangular units (for both phase II and III) are the same type of double hydrogen bonds ($N-H\cdots N$, $N-H\cdots N$) as for the linkage of quartet motifs in phase I. However, it should be noticed that the double hydrogen bonds ($N-H\cdots N$, $N-H\cdots N$) linking the rectangular motifs might also have been broken in the first stage during adsorption of K ions and reconnected together in the further self-assembly process. Otherwise phase III as shown in Fig. 3.19(b) would not be expected to exist, since half of the rectangular motifs in that phase have rotated with respect to phase II as shown in Fig. 3.19(a) indicating the freedom of the whole rectangular motif. Thus, the scenario would be two K ions embedded into each G-quartet motif (by breaking part of the intra-quartet hydrogen bonds), resulting in the above-mentioned rectangular motif after deposition of K^+ at higher dose. Meanwhile the inter-quartet hydrogen bonds were also split apart, probably due to the locally accumulated strain induced by incorporating more K ions into quartets than for the case of phase I. Also, the rectangular motifs are locally moveable and thus render the formation of both

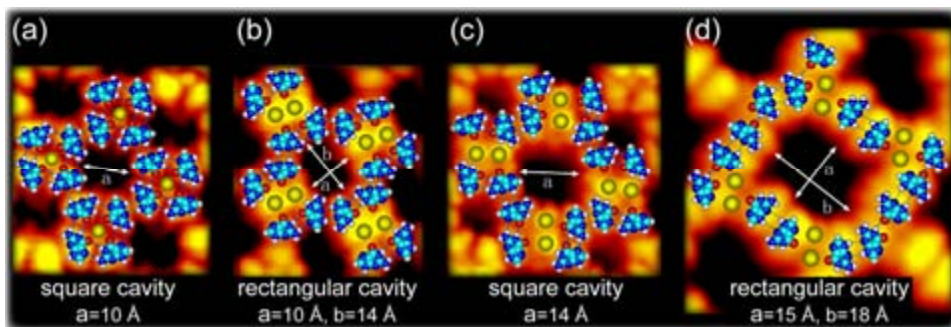


Figure 3.21: (a)-(d) Investigation on the size and shape of different cavities formed by G and K^+ complex (phase I, II, III, IV, respectively). The proposed models have been superimposed on each STM image.

phase II and III, which adopt the same inter-quartet hydrogen bonds as for phase I, though the rectangular motifs are rotated alternatively in phase III.

Surprisingly, through further increase of the amount of K^+ dose, an unexpected metallosupramolecular network with the ratio of $K:G=2:3$ (phase IV) has been found as shown in Fig. 3.20(a). In this case the G-quartet motifs were completely gone; instead, a much more open honeycomb network with homogeneous cavities was formed. The inset in Fig. 3.20(a) explicitly shows the atomic-resolved structure with unambiguous identification of the K ions (small dots among the G molecules). Based on our high-resolution STM images the proposed model is shown in Fig. 3.20(b), in which a local threefold asymmetrical unit comprising of two K ions and three G molecules can be identified. Note that the former-mentioned phase I, II and III could be considered as homochiral ones (i.e. all of the G molecules have the same chirality: molecule either faces up or down with respect to the surface). However, this honeycomb phase IV is heterochiral in the sense that one G molecule has different chirality from the other two in the threefold unit as indicated in Fig. 3.20(b) (different colour coding indicates different chiralities). Considering that each isolated island of G-quartet network is homochiral at RT, though different islands were usually found to have different chiralities, no racemic structure was found at RT [66]. It implies that phase IV was formed by breaking the whole G-quartet motif apart into individual molecules due to incorporation of considerable amount of K ions. Then the individual G molecules (with different chiralities) diffuse around and reorganize into the complex honeycomb metallosupramolecular network from an interplay of hydrogen bonding and metal-to-ligand bonding. Therefore the former three metallosupramolecular networks (phase I, II and III) are suggested to be kinetically trapped structures, and the hydrogen bonding situation (with respect to the G-quartet network) is only locally affected by the K ions. However, the honeycomb metallosupramolecular network (phase IV) is considered to be a thermodynamically stable structure at RT, since both inter- and intra-quartet hydrogen bonds are largely disturbed as G molecules and K ions diffuse around on the surface and finally reorganize into the experimentally observed phase IV.

Further investigation on these four different metallosupramolecular nanoporous networks formed on the surface reveals that though the same molecule is employed, by delicately changing the ratio of K ion, we have succeeded in creating various

nanocavities in a controlled manner. Figs. 3.21(a)-(d) illustrates various cavities with different shapes and sizes fabricated in this study. Notice that previously reported studies on creating nanoporous structures were based on employing different molecular building blocks with different lengths, functional groups, symmetries, etc., or balancing the molecule-substrate interactions and registries [154-159]. While in this study, by varying the ratio of K^+ dose, the competition between hydrogen bonding and metal-to-ligand bonding can be delicately adjusted. Hence the resulted metallosupramolecular nanoporous structures, which opens a new avenue to create nanoporous networks in a controlled manner.

3.6.3 Conclusion

In conclusion, for the first time the biologically relevant K^+ -embedded G-quartet metallosupramolecular network was observed on the surface in real space. Different metallosupramolecular nanoporous networks which are dependent on the K^+ ratio are formed with various cavities in size and shape. Those networks are found to be as a result of balancing between hydrogen bonding and metal-to-ligand bonding. The current work might provide new insight into the G-quadruplex structure in biological community and thus anti-cancer drug design.

3.7 DNA base derivatives on Au(111)

3.7.1 Introduction

DNA has been shown to have the potential to lead to new avenues for directed self-assembly of nanostructures with controlled functionalities on a surface. While Watson-Crick base pairing is dominant within nucleic acids, it is important to note that the nucleobases are not exclusive in their binding behavior. There are for example at least 28 possible base-pairing motifs that involve at least two hydrogen bonds which can be formed between the four natural bases. These, and other nucleobase binding modes, can play an important role in any nucleobase self-assembly process, which is controlled by hydrogen bonding. Single nucleobases have the ability to form one- or two-dimensional supramolecular nanostructures, when deposited onto various surfaces. To understand the DNA replication mechanism in further details it is natural to simplify the studied system by appropriately choosing the model system. In this study non-natural modified DNA bases have been investigated by high-resolution STM imaging. In these non-natural bases the nitrogen atom normally attached to the sugar moiety in DNA has been replaced by a bulky group. Such modification will lead the studied system to be closer to the hydrogen-bonded situation of base pairing in DNA structure by replacing one of the H donor groups, thus reducing the possibilities of base pairing steered by hydrogen bonding. Therefore it would be more vivid to explore the base complementarities in such a system, since all of the hydrogen bonding sites on the non-natural bases should be the same as the ones in real DNA structure. Here we briefly show some very recent results on those modified bases on the Au(111) surface.

3.7.2 Results and discussion

To investigate how the modified bases behave on the surface we deposited A_derivative, T_derivative, G_derivative, and C_derivative by thermal sublimation at 370 K, 360 K, 420 K, 360 K, respectively, onto a clean Au(111) substrate held at room temperature (RT). For co-deposition experiments C_derivative was first deposited and then followed by G_derivative. After deposition the sample was transferred in-situ to the cold STM. From Fig. 3.22 it is clearly seen that by replacing one of the H donor groups in G and A molecules the self-assembled structures are dramatically changed. The G_derivative is imaged as a triangle and a ball representing the G moiety and phenyl moiety, respectively. The G_derivatives form 1D hydrogen-bonded zigzag chains that are laterally linked by the phenyl groups resulting in the observed 2D structure. The A_derivative is imaged as a stick including the A moiety, phenyl moiety and Br atom which shows bright contrast in the end of the molecule. It is also clear that the A_derivatives form an interdigitated chain structure that is obviously distinguishable from the network structure formed by A.

Fig. 3.23 (left) shows the DFT calculated structure of G_derivative superimposed on the high-resolution STM image and a good agreement is achieved. It can be seen from both the experimental and theoretical results that the structure formed by G_derivative is heterochiral (i.e. molecules have different chiralities and in equal amount). Fig. 3.23

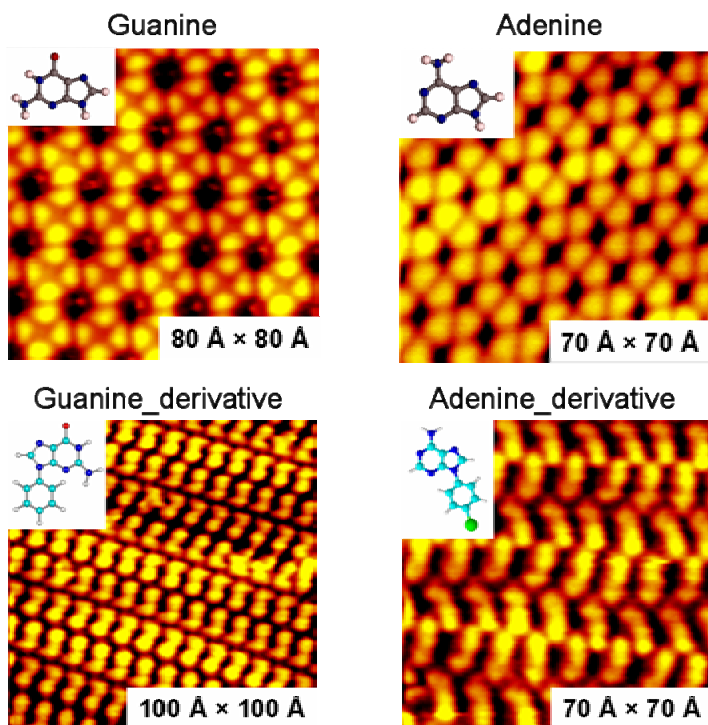


Figure 3.22: Comparison of the self-assembled nanostructures formed by G and G_derivative, A and A_derivative, respectively. For G and A derivatives: red: O, dark blue: N, light blue: C, white: H, green: Br.

(right) shows the tentatively proposed structure of A_derivative (a heterochiral one as well) superimposed on the high-resolution STM image.

Fig. 3.24 shows the self-assembled structures formed by C_derivative and T_derivative, as compared with the structures formed by C and T. It clearly reveals that ordering can be achieved by the C_derivative as compared with the C nanostructures. However, deposition of T_derivative results in some disordering. Another T_derivative with a bigger bulky group is still under investigation.

Fig. 3.25 shows a very interesting honeycomb network formed by co-deposition of C_derivative and G_derivative. Considering there is only locally ordered structures formed by co-deposition of C and G, this honeycomb network formation provides a step forward with respect to the studies of molecular recognition between complementary base pairs. The modeling of this honeycomb network is being investigated.

3.7.3 Conclusion

Four DNA base derivatives have been studied which reveals dramatic changes of the self-assembled nanostructures formed on the Au(111) surface as compared with the original bases. Co-deposition of C_derivative and G_derivative results in an unexpected honeycomb network, which might provide useful information on the studies of molecular recognition between complementary base pairs.

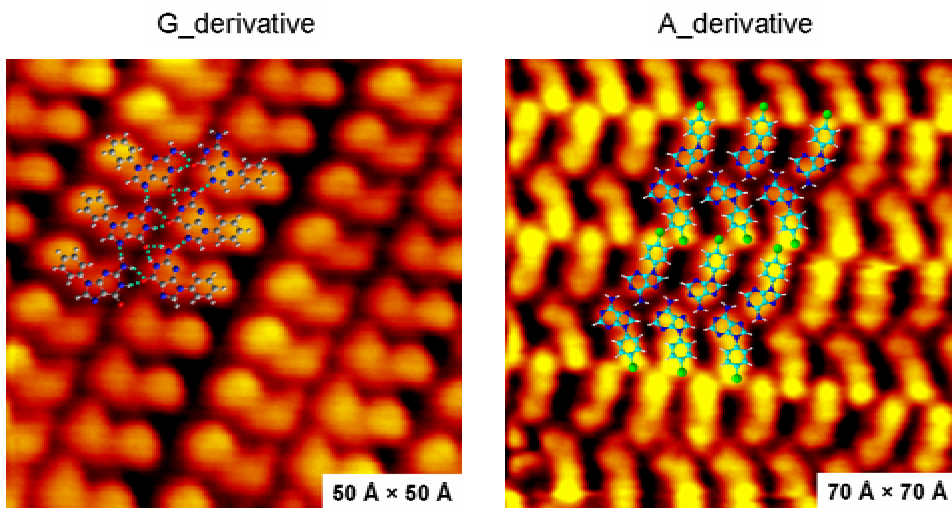


Figure 3.23: DFT calculated structure of G-derivative and tentative model of A-derivative have been superimposed on the high-resolution STM images.

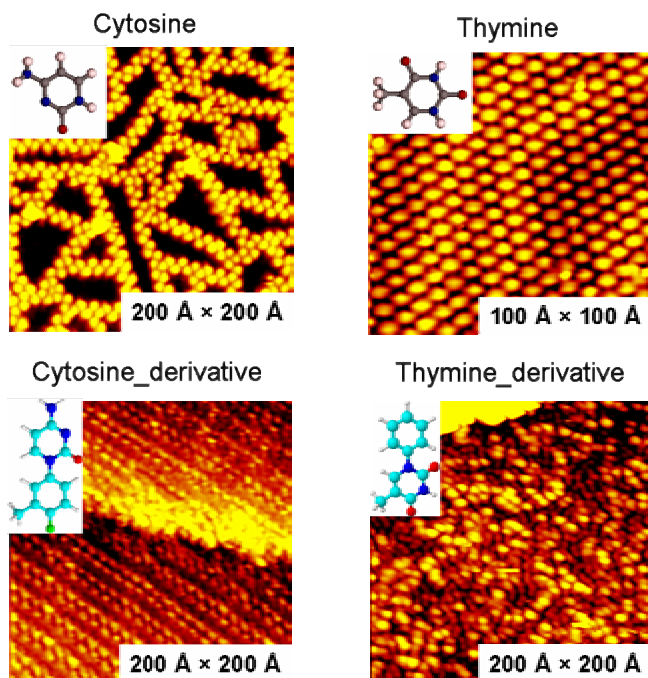


Figure 3.24: Comparison of the self-assembled nanostructures formed by C and C_derivative, T and T_derivative, respectively. For C and T derivatives: red: O, dark blue: N, light blue: C, white: H, green: F.

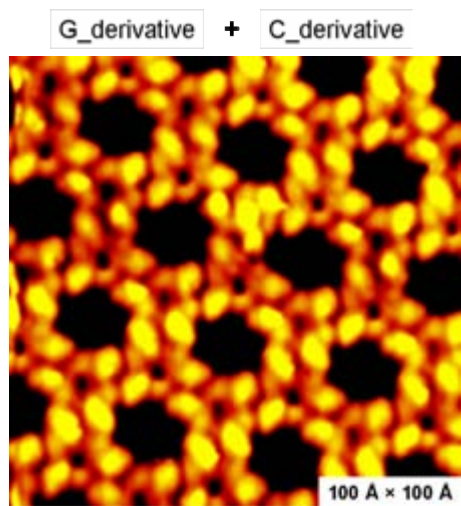


Figure 3.25: The honeycomb network formed by co-deposition of G_derivative and C_derivative.

CHAPTER 4

Rosette assembly and its building blocks on Au(111)

In this chapter a systematic investigation of adsorption of rosette assembly and its building blocks on a Au(111) surface will be described in detailed. As a first step, we investigated how self-assembled nanostructures are influenced by slight variations in the molecules that are used as small building blocks in rosette assemblies. Here I present different well-ordered nanostructures on Au(111) by variation of submolecular group on the cyanuric acid (CYA) molecule, which provides information on the control of supramolecular structures on surfaces by balancing different intermolecular interactions. As a next step, we investigated how to build up 2D nanostructures using complementary hydrogen bonds between different molecules. Here one of the most extensively studied model systems involving complementary hydrogen bonds between CYA and melamine (M) has been investigated. In our study, we found that stoichiometry plays an important role in determining the assembled structures from CYA and M on the surface. Then we changed our attention to the investigation of a realistic supramolecular assembly. The 3D highly ordered rosette assembly, which includes complementary hydrogen bonds, was chosen to explore the possibility of bringing such giant supramolecular complex to vacuum/solid interface and to investigate the influence of surface on the self-assembly process of such supramolecular complex.

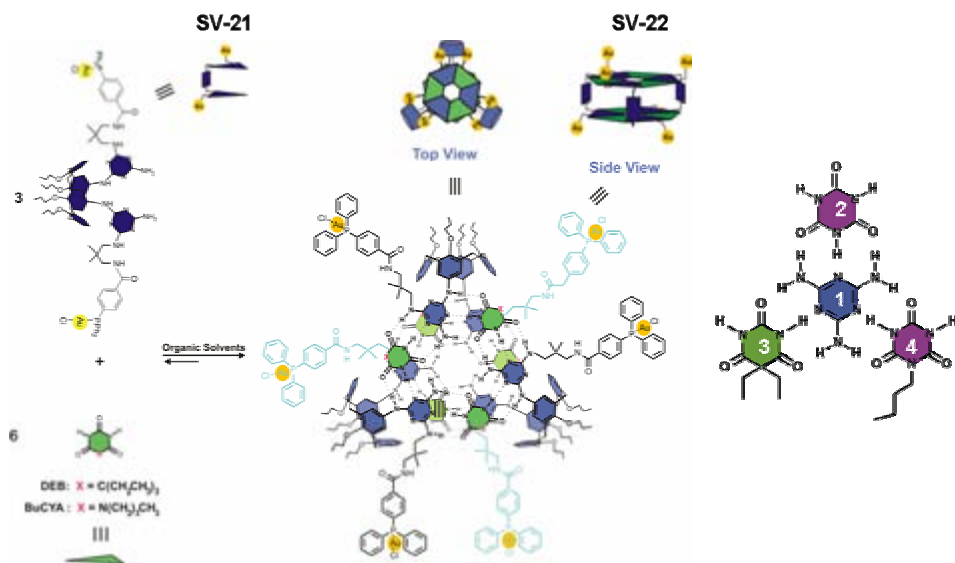


Figure 4.1: Illustrative scheme showing the self-assembly process of rosette assembly (SV-22) in solution. The rosette assemblies are built up from three big building blocks (SV-21) and six small building blocks (CYA/DEB/BuCYA). These small building blocks are simple organic molecules and can be interchanged at will. The SV-21 is a 3D complex compound built up of melamine derivatives. The essential bonding in the self-assembly of rosette assemblies occurs between the molecules shown on the right panel. The central blue one (1) is a melamine molecule which can form complementary hydrogen bonds to the other small building blocks (the purple one without tail is CYA (2), the green one with two tails (3) is DEB, the purple one with one tail (4) is BuCYA).

4.1 The rosette system

4.1.1 Introduction

Supramolecular chemistry based on noncovalent interactions is a powerful synthetic tool for the preparation of complex molecular architectures [172,173]. In particular, hydrogen bonds are considered to be useful for controlling molecular self-assembly due to the reversibility, specificity, directionality, and cooperative strength of this class of interactions [174,175]. An extensively studied heteromolecular H-bonding motif results from the interaction between diaminopyridine and diimide moieties, exhibiting three complementary NH \cdots O and NH \cdots N hydrogen bonds [174,179-181]. This classic H-bonding interaction has been exploited in the solution phase [180,181], in the solid state [174], and more recently at interfaces [51,52,176,182,183]. A prototypical molecular system exhibiting this complementary interaction is the cyanuric acid/melamine (CYA/M) system. The basic structure formed from these compounds both in solution, in bulk, and on surfaces is a symmetric two-dimensional (2D) array consisting of cyclic hexamers of 3M and 3CYA molecules, which was predicted in early studies [179] and later characterized by bulk X-ray diffraction [184,185].

Based on such classic H-bonding interaction between diaminopyridine and diimide moieties, a complex self-assembled supramolecular system, the so-called rosette assembly as shown in Fig. 4.1, has been recently synthesized [4,173]. From Fig. 4.1 it can be seen that the essential process during self-assembly is the formation of complementary hydrogen bonds between melamine derivatives and other small building blocks (such as DEB/CYA/BuCYA). This assembly which is formed in a liquid environment includes 36 hydrogen bonds and has a well-defined shape and size in 3D. One big advantage of this compound is that slight modification of the building blocks yields differently functionalized rosette assemblies. As a result, it is relatively easy to design the functionalities.

The ultimate goal and the most challenging part of 'bottom up' self-assembly is to construct 3D supramolecular structures on solid surfaces, which could be potentially used as functional molecular devices on surfaces. In this project we explored the transferability of such giant supramolecular complex to vacuum/solid interface and in particular studied one of the rosette assemblies, the so-called SV-22 (see Fig. 4.1), which is built up from big building blocks calix[4]arene dimelamines (SV-21) (which is a complex compound containing melamine derivatives) and small building blocks (DEB). By changing the small building blocks from DEB to CYA or BuCYA (both of which have very similar chemical structures to DEB) or by modifying the side groups of SV-21, other functionalized rosette assemblies can be synthesized. In the following sections I will detail the studies on this rosette assembly.

4.2 CYA, DEB, BuCYA on Au(111)

4.2.1 Introduction

First we studied these three small building blocks with the aim to achieve predictive power with respect to how molecular building blocks may be designed to form desired surface nanostructures. Although impressively ordered and complex structures have by now been synthesised and characterised, there is still a pronounced need to extend the database on molecular surface structures and, most importantly, systematically explore the relative importance and interplay between the different types of interactions involved. Here we used high-resolution STM imaging under UHV conditions to characterise and systematically compare adsorption structures formed from three closely related compounds with strong hydrogen-bonding capability on the Au(111) surface. We surprisingly find that slight variations of a submolecular alkyl group, not directly involved in the H-bonding, can have a pronounced effect on the self-assembled surface nanostructures causing a change from extended periodic rows to localised chains and polygonal clusters. The change is attributed to subtle differences in vdW interaction between the alkyl side-chains found on some of the compounds, an insight that can be employed to control the self-assembled surface nanostructures when multifunctional groups are involved in the molecular building blocks.

4.2.2 Results and discussion

The molecules investigated here are CYA, DEB and BuCYA, see Fig. 4.2. CYA is a three-fold symmetric molecule with three NH proton donating groups and three O

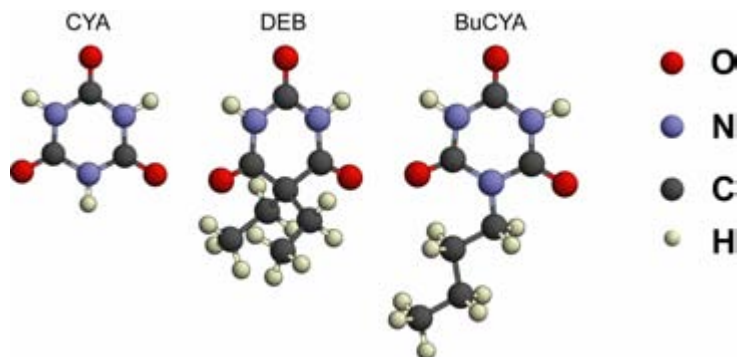


Figure 4.2: Model of the CYA, DEB, and BuCYA molecule, respectively.

acceptors allowing for $\text{NH}\cdots\text{O}$ H-bonds between the CYA molecules. In DEB one of the NH donor groups of CYA is replaced by two short alkyl chains (di-ethyl) attached at a carbon atom (C-alkyl) removing one of the H-donating sites. In BuCYA one of the NH donor groups of CYA is instead replaced by a longer alkyl chain (n-butyl) attached at a nitrogen atom (N-alkyl). Note that these modifications leave the same potential H-bonding sites available for DEB and BuCYA. The CYA, DEB, and BuCYA molecules were evaporated from glass crucibles in a home-built molecular evaporator by thermal sublimation at 350 K, 370 K, and 380 K, respectively, onto a clean Au(111) substrate held at room temperature. The Au(111) substrate was chosen as a noble inert substrate to minimize molecule–substrate interactions, thus allowing the self-assembly process to be dominated by intermolecular interactions.

Deposition of CYA onto the Au(111) surface leads to extended, ordered islands with a close-packed molecular structure as shown in Fig. 4.3a. The characteristic herringbone reconstruction of Au(111) can still be observed as a modulation of the molecular overlayer, indicating that the molecule-substrate interaction is not sufficiently strong to perturb the reconstruction. Each compact, slightly triangular protrusion corresponds to one CYA molecule. As displayed in the structural model of Fig. 4.3b, each CYA molecule forms H-bonds to its six nearest neighbours, creating a close-packed three-fold symmetric network. The unit cell dimensions are $a = 7.3 \pm 0.7 \text{ \AA}$ and $b = 7.0 \pm 0.7 \text{ \AA}$ as determined from the STM data. All of the molecular proton donating/accepting groups are involved in H-bonds.

Deposition of DEB also leads to extended molecular islands, but with a different molecular packing. As shown in Fig. 4.3c, zigzag molecular chains are formed, consisting of elongated molecular features displaying two sub-protrusions. The molecular orientation in adjacent chains is slightly different, but the structure is repeated for every two rows of molecules as indicated by the dashed lines. A unit cell for the molecular overlayer is shown with dimensions $a = 7 \pm 0.5 \text{ \AA}$ and $b = 26 \pm 1 \text{ \AA}$. A corresponding molecular model is displayed in Fig. 4.3d. The structure is explained as molecular chains in which each DEB molecule is linked to four neighbouring molecules via $\text{NH}\cdots\text{O}$ H-bonds similar to the situation for the CYA structure. The alkyl side-chains of the di-ethyl groups face away from the chain interiors. This prevents the formation of inter-chain H-bonds, consistent with the dark regions between the chains revealed in the STM image (Fig. 4.3c), but may be favourable for intermolecular vdW interaction. For adsorption with the ring-plane parallel to the surface, the di-ethyl chains will point away

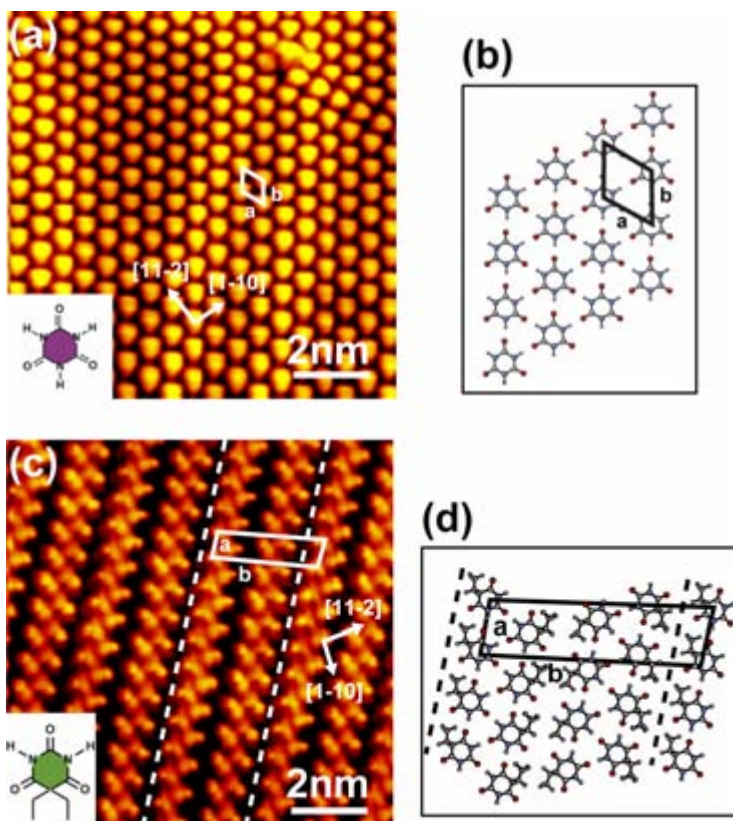


Figure 4.3: (a) STM image ($I_t = -0.72$ nA, $V_t = -1250$ mV) of self-assembled close-packed structure of CYA molecule on the Au(111) surface. The white rhomboid indicates the unit cell of this structure. (b) Model of the close-packed structure formed by CYA. The unit cell is indicated by the black rhomboid. (c) STM image ($I_t = -0.66$ nA, $V_t = -371$ mV) of twin chain structure formed by DEB on the Au(111) surface. A unit cell is indicated by the white rhomboid. (d) Model of the DEB twin chain structure with a unit cell indicated by the black rhomboid.

from and into the surface, due to the 3D molecular geometry. In the displayed model the two alkyl-chains are aligned exactly below each other and consequently only one is visible.

It is evident that replacing one of the donor groups of CYA with an alkyl group leads to a completely different self-assembled nanostructure. This is to be expected as the number of potential hydrogen-bonding sites is reduced and the three-fold symmetry of the molecule is broken. As the modification in BuCYA is very similar to DEB in the sense that one donor group is replaced by an alkyl chain, one might expect formation of similar structures for BuCYA and DEB. However, in sharp contrast to the results obtained for CYA and DEB, only locally ordered structures were formed upon deposition of BuCYA on Au(111) as shown in the overview image of Fig. 4.4a. The characteristic features observed are short segments of molecular chains and a few instances of polygonal ring-structures. The short molecular chains are randomly oriented, indicating lack of epitaxial order and a corresponding weak molecule-substrate interaction. The BuCYA molecular chains are shown in more detail in Fig. 4.4b, along

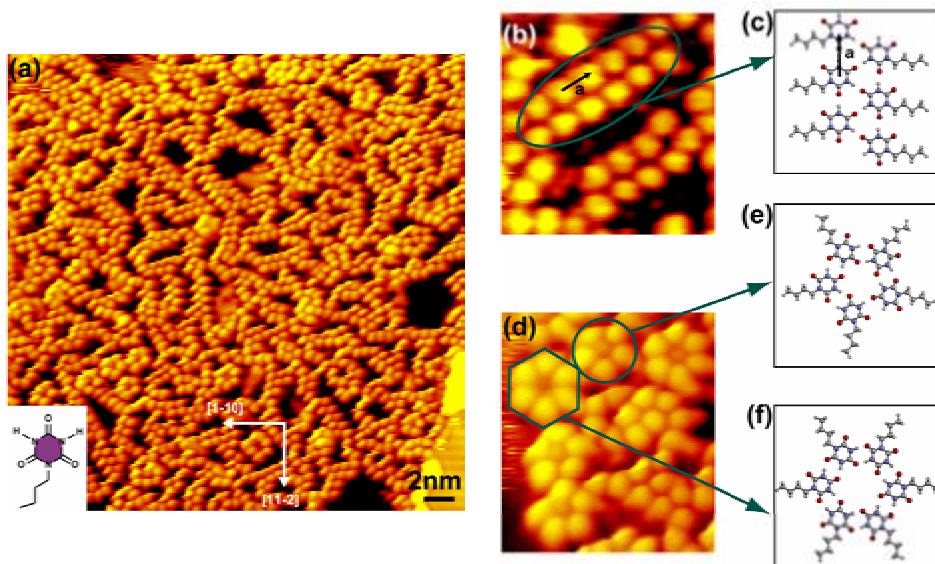


Figure 4.4: (a) STM image ($I_t = -0.39$ nA, $V_t = -1050$ mV) of short range ordered structures formed by BuCYA molecules on the Au(111) surface. (b) Close-up of the molecular chain structure (c) Model of the chain structure. (d) Close-up of pentagon and hexagon structures. Corresponding models are shown in (e) and (f), respectively.

with a structural model in Fig. 4.4c. The repeat distance along the chain is measured to be $a = 7 \pm 0.5$ Å. The chains have a similar zigzag hydrogen bonding motif as described for the DEB chains with each BuCYA molecule linked to four neighbours. The butyl side groups are assumed to extend to the sides of the chains, but do not provide contrast in the STM images. The co-existing pentagon and hexagon BuCYA structures are shown in Fig. 4.4d with structural models in Fig. 4.4e and f. In both structures, each BuCYA molecule is H-bonded to its nearest neighbours via two H-bonds.

By comparing the structures formed by DEB and BuCYA to the close-packed network formed by CYA, it becomes clear that all the observed structures are strongly guided by the anticipated $\text{NH}\cdots\text{O}$ hydrogen bonding interactions as evidenced by the similar triangular arrangement of molecules found in all the structures in which the intermolecular separation is ~ 7 Å. It is, however, intriguing, why the overall self-assembled nanostructures are so dramatically different for DEB and BuCYA although the two compounds have the same available H-bonding sites. In principle the binding strength of these sites may be slightly different for the two molecules due to subtle differences in their charge distribution caused by the intrinsically different C-alkyl (DEB) and N-alkyl (BuCYA) chains which are sp^3 and sp^2 bonded respectively. However, this is expected to be a minor effect. One clue to the difference between the two situations may be obtained from Fig. 4.4a where it is noticeable that the short fragments of the BuCYA chains are never aligned next to each other similar to the extended chains observed for DEB. We therefore speculate that the main difference between the two situations is an increased vdW attraction between the alkyl chains of DEB compared to BuCYA, leading to a higher degree of order for DEB. The side-chains on the two molecules have the same number of C-atoms. The increased vdW interaction is therefore attributed to partial detachment of one of the ethyl side-chains of DEB from the substrate

caused by the sp^3 bonding geometry of the di-ethyl group. This enables the side-chains to align in closer proximity to each other as compared to the case of BuCYA. Moreover, the end-groups may benefit from additional degrees of conformational freedom available in partially detached molecules further strengthening the vdW interactions.

4.2.3 Conclusion

In summary, we have systematically compared adsorption structures formed from a class of compounds that all display the same type of strong hydrogen bonding groups. The observed structures all appear to be dominated by the anticipated hydrogen-bonding interactions, but we surprisingly find that subtle changes to a side-group not directly involved in the H-bonding itself has a pronounced influence on the formed structures. This highlights the importance of obtaining an improved fundamental understanding of the hierarchy of interactions that underlie formation of well-defined nanostructures on surfaces and may guide future efforts to fine-tune intermolecular interactions to create desired self-assembled nanostructures.

4.3 Coadsorption of CYA and M on Au(111)

4.3.1 Introduction

We continue our work to investigate the classic H-bonding interaction in the CYA·M model system via coadsorption of CYA and M on a Au(111) surface. From the submolecularly resolved images, the M and CYA molecules are clearly distinguishable. The presence of the expected 1:1 stoichiometric phase after simultaneous deposition of CYA and M is verified. In addition, a novel nonstoichiometric phase (CYA_1M_3) is identified, which forms upon sequential deposition of M followed by CYA. The energetics of the homo- and heteromolecular interactions of M and CYA has been evaluated from self-consistent charge density-functional-based tight-binding (SCC-DFTB) calculations to explain the observed structures.

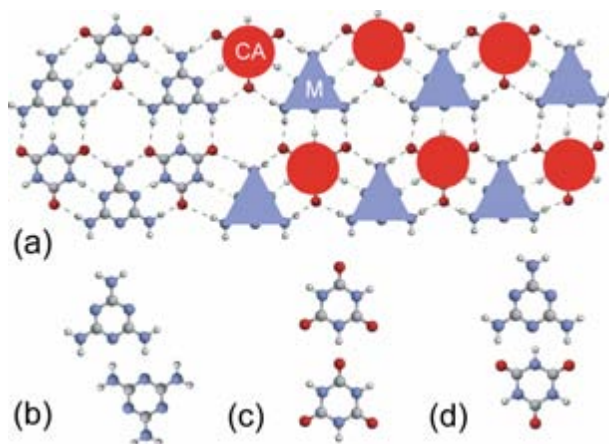


Figure 4.5: (a) Schematic representation of the CYA_1M_1 lattice stabilized by $\text{O}\cdots\text{HN}$ and $\text{N}\cdots\text{HN}$ hydrogen bonds. (b–d) Homo- and heteromolecular interactions between CYA and M molecules (red: O, blue: N, white: H, gray: carbon).

4.3.2 Results and discussion

Fig. 4.5a depicts a 2D array consisting of cyclic hexamers of 3M and 3CYA molecules. Homo- and heteromolecular dimers formed from M and CYA are depicted in Fig. 4.5b–d. The M dimer in Fig. 4.5b involves two H bonds between the NH donor and N acceptor groups and the calculated binding energy (E_b) for the optimized structure is 0.17 eV/molecule. The dimer formed from CYA molecules shown in Fig. 4.5c has a binding energy of 0.11 eV/molecule. Finally, the heterodimer formed through complementary coupling of one M and one CYA involves one $\text{NH}\cdots\text{N}$ and two $\text{NH}\cdots\text{O}$ hydrogen bonds and has a binding energy of 0.24 eV/molecule.

Both CYA and M were deposited by thermal sublimation from molecular evaporators held at ~ 356 K. Simultaneous deposition of CYA and M was achieved by heating both evaporators and overlapping their output beam on the surface. Molecules

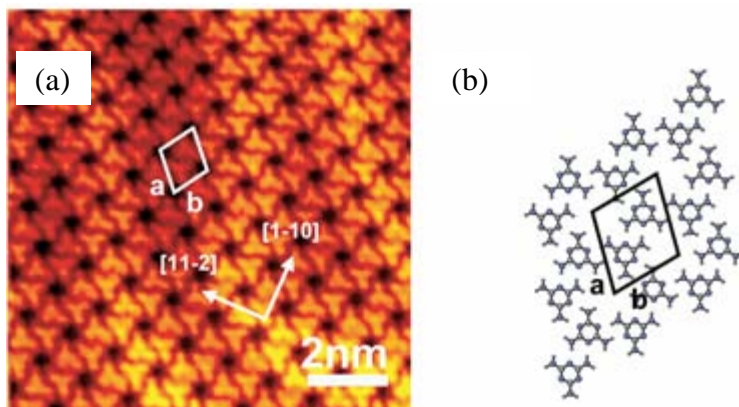


Figure 4.6: (a) STM image ($102 \times 104 \text{ \AA}^2$) of M network ($I_t = 0.5 \text{ nA}$, $V_t = 1250 \text{ mV}$) on Au (111). (b) Optimized model for the H-bonded M network.

were deposited onto the Au(111) sample held at room temperature. Adsorption structure formed upon deposition of CYA has been discussed in the last chapter. The adsorption structure formed by M on Au(111) is shown in Fig. 4.6. After deposition of M large well-ordered islands are observed. The herringbone reconstruction does not appear to change upon molecular adsorption or affect the self-assembly patterns observed in this study. This confirms that the molecule–substrate interaction here plays a minor role for the molecular ordering. STM image of M as shown in Fig. 4.6a shows that individual M molecules are resolved with a characteristic three-spoke shape, attributed to the position of the amino groups, which is distinctly different from the appearance of the CYA molecules with near-circular symmetry (cf. Fig. 4.3a). M forms a more complicated structure than CYA in which the spokes of neighboring molecules interdigitate, leading to the formation of six-membered rings surrounding open pores in the network. From the corresponding optimized model for M (Fig. 4.6b) the structure is seen to involve double H-bonding interactions to three neighbors surrounding each molecule. The lattice parameters for the calculated networks of M and CYA correspond well to those obtained from the STM images, as can be seen in Table 4.1.

The binding energies for the optimized periodic networks shown in Fig. 4.6b and Fig. 4.3b are 0.47 eV/molecule (M) and 0.65 eV/molecule (CYA), respectively. The networks are built up of homodimers of the type depicted in Fig. 4.5. The corresponding binding energies obtained by appropriately summing the pairwise interaction energies for these dimers are 0.51 eV for M and 0.66 eV for CYA (see also Table 4.2), that is, they are close to the calculated values for the extended networks. This is in contrast to, for example, networks of guanine molecules [66], where pronounced cooperative effects lead to a non-additive scaling of binding energy with the number of hydrogen bonds. In both the M and CYA networks, each molecule forms six H bonds, and the stronger binding energy of the CYA networks reflects that the $\text{NH}\cdots\text{O}$ hydrogen bonding interactions are stronger than the $\text{NH}\cdots\text{N}$ bonds, as expected [175].

Simultaneous deposition of CYA and M leads to a self-assembled network as shown in Fig. 4.7a. The characteristic circular and three-spoke shape for CYA and M is resolved (most clearly seen at the top-left side of the image), showing that the structure is a binary mixed phase involving heteromolecular H-bonding. Domains of pure CYA islands are found to coexist with this mixed phase, most likely due to a slight excess of

Network	Measured		Calculated	
	a [Å]	b [Å]	a [Å]	b [Å]
M	10.0 ± 1.0	11.4 ± 1.1	10.6	10.8
CA	7.3 ± 0.7	7.0 ± 0.7	6.8	6.9
CA ₁ M ₁	9.6 ± 1.9	7.4 ± 1.5	9.8	9.8
CA ₁ M ₂	25.8 ± 5.1	21.5 ± 4.3	20.3	20.3

Table 4.1: Measured and calculated lattice parameters for the unit cells displayed in Fig. 4.3a and Figs. 4.6–4.8. A good agreement is found for the M and CYA networks. Thermal drift during the measurements on the CYA–M networks hampers an accurate determination of the lattice parameters in these cases.

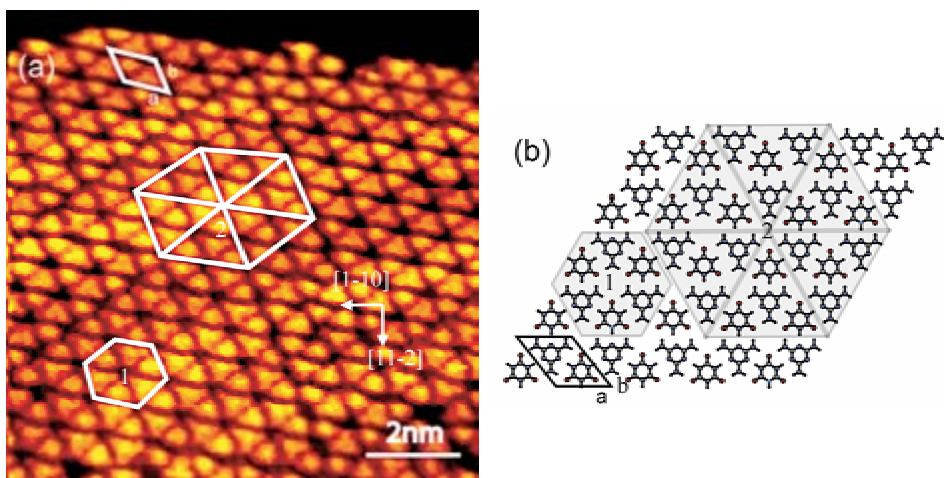


Figure 4.7: (a) STM image ($102 \times 104 \text{ \AA}^2$) of a self-assembled network resulting from simultaneous deposition of M and CYA on Au(111). The characteristic ball- and three-spoke shapes for CYA and M are clearly resolved. The structure is a mixed phase corresponding to the CYA₁M₁ network presented in Figure 4.5 ($I_t = 0.56 \text{ nA}$, $V_t = 1250 \text{ mV}$). (b) Optimized model for CYA₁M₁ network. The hexagons marked “1” and “2” in (a) and (b) show corresponding areas as a guide to the eye.

CYA molecules on the surface. Comparison of the area indicated with the hexagon marked “1” in Fig. 4.7a to the model for the CYA₁M₁ structure shown in Fig. 4.5a reveals that the observed structure corresponds to a motif based on the complementary CYA⋯M coupling of Fig. 4.5d. A binding energy of 0.82 eV/molecule is found for this stoichiometric CYA₁M₁ network, which is thus energetically preferred over the structures formed from the individual constituents. The corresponding binding energy calculated from the pairwise M⋯CYA dimer interaction energies is 0.72 eV/molecule (see Table 4.2), showing a slight tendency to additional stabilization in the extended network, which may result from each amino group on the M molecules engaging in two H-bonds to oxygen atoms on adjacent CYA molecules. The calculated H-bond lengths of

	Calculated E_b per dimer [eV]	Number of molecules per unit cell	Pair interactions per unit cell	Network E_b per molecule [eV] ^[a]	Calculated E_b per molecule [eV] ^[b]
M	0.34	2 × M	3 × M–M	$\frac{3 \times 0.34}{2} = 0.51$	0.47
CA	0.22	1 × CA	3 × CA–CA	$\frac{3 \times 0.22}{1} = 0.66$	0.65
CA ₁ M ₁	0.48	1 × M, 1 × CA	3 × CA–M	$\frac{3 \times 0.48}{2} = 0.72$	0.82
CA ₁ M ₃	–	6 × M, 2 × CA	6 × M–M, 6 × M–CA	$\frac{(6 \times 0.34) + (6 \times 0.48)}{8} = 0.62$	0.68

[a] Based on E_b of the dimer. [b] Calculated for each network.

Table 4.2: Calculated binding energy (E_b) by the SCC-DFTB method for dimers and extended networks (see 1st and 5th column). These numbers can be rationalized by counting the molecules present in the unit cells (see 2nd column) as well as the interactions between pairs of molecules (see 3rd column) in each of the networks in Fig. 4.3a,b and Figs. 4.6–4.8. Note that interactions with molecules in an adjacent unit cell only count for half. This allows for the estimation of the binding energy purely based on E_b of the respective dimers, as shown in the 4th column.

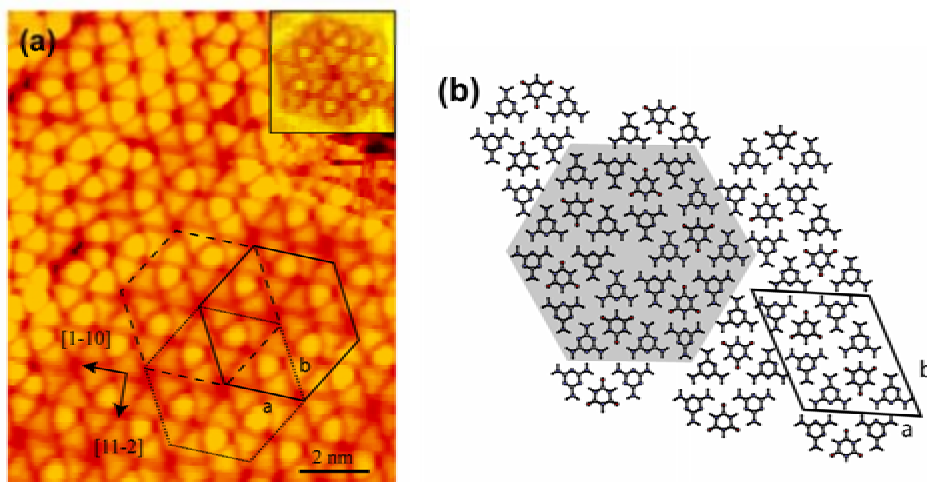


Figure 4.8: (a) STM image ($105 \times 128 \text{ \AA}^2$) of a self-assembled network on Au(111) resulting from deposition of CYA after M. The inset ($38 \times 41 \text{ \AA}^2$) shows the typical hexagon showing the shape of the individual molecules. Dividing such an hexagon in triangles as depicted schematically shows that in this network each CYA molecule bonds to three M molecules ($I_t = 0.52 \text{ nA}$, $V_t = 1250 \text{ mV}$). (b) Optimized model for this novel CYA₁M₃ network.

1.86 Å (O··H) and 1.96 Å (N··H) for the CYA₁M₁ network are in good agreement to the values of 1.93 Å and 2.01 Å obtained by bulk X-ray diffraction experiments [184,185]. The strength of the interaction between M and CYA has been addressed in bulk chemistry [187,188], but a direct comparison to the values obtained here is hampered by the complicated nature of the dissociation process for large rosette assemblies and also by solvent effects.

To investigate the influence of the deposition conditions on the formation of the CYA–M network we performed experiments in which the compounds were deposited sequentially onto samples held at room temperature. The thermal stability of the pure CYA and M phases was assessed by imaging the surface with the STM held at 300 K,

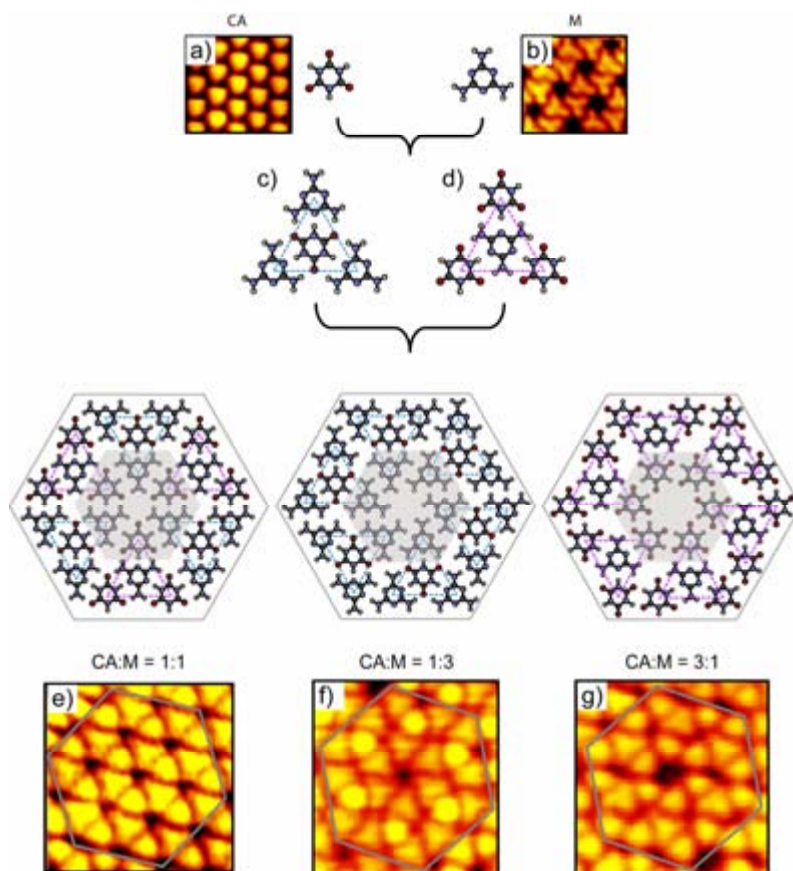


Figure 4.9: Systematic illustration shows the formation process of CYA·M complexes from individual component. (a) and (b) show how the individual component CYA and M behave on the surface. The schematic drawings (c) and (d) illustrate two different characteristic triangular structures formed by CYA and M. The three structural motifs of CYA·M complexes with their calculated molecular models are shown as (e)-(g).

showing that both the CYA and M networks are stable and can be imaged at room temperature, though diffusion process was found at the boundary of molecular islands for both CYA and M. In the sequential deposition experiments, molecules of the second component deposited may thus land both on top of and adjacent to islands of the first deposited component. If M is deposited after CYA, we observe primarily a separation into individual islands of CYA and M. However, if CYA is deposited after M we find extended regions of a binary mixture of CYA and M, of which an STM image is shown in Fig. 4.8a. Simultaneously, areas of pure M and CYA can also be seen, the occurrence of which depends on the relative ratio between the two compounds. The characteristic hexagons which are observable in these networks, as shown in the inset of Fig. 4.8a, shows that the ratio of M to CYA in this network is 3:1. We conclude that sequential deposition leads to a novel CYA_1M_3 network not present in the originally suggested structure. This novel network is only observed as a locally ordered structure as visible in Fig. 4.8a.

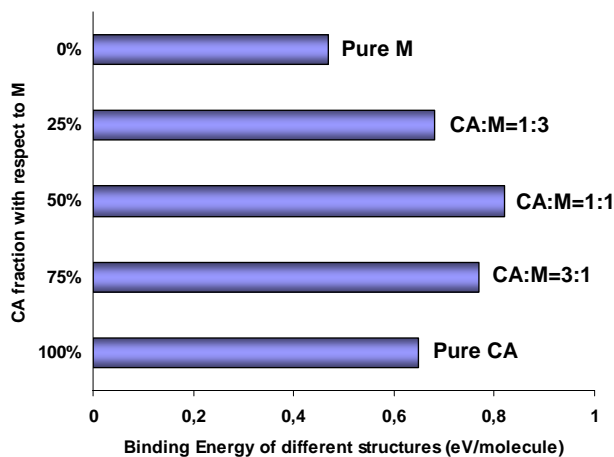


Figure 4.10: Calculated binding energies of different structures as a function of CYA fraction with respect to M in the CYA·M complexes.

From the structural model in Fig. 4.8b, the intermolecular interaction in this novel phase is seen to be identical to those of the pure M and the M–CYA structures. In particular the characteristic six-membered ring of M molecules is found in the center of the indicated hexagons. A binding energy of 0.68 eV/molecule has been calculated for the CYA_1M_3 network in the optimized structure shown in Fig. 4.8b. To rationalize this value, one may evaluate the number of M–M and M–CYA interactions in each unit cell of the rather complicated network structure (see Table 4.2). If each of these interactions is assumed to contribute the same binding energy as in the M and the CYA dimers, respectively, a binding energy for the CYA_1M_3 network of 0.62 eV is found, which is close to the calculated value for the optimized structure. Hence, the binding energies of all the extended networks are well accounted for by the pairwise interaction energies of the involved molecular building blocks.

The binding energy for the CYA_1M_3 phase is lower than the 0.82 eV/molecule found for the CYA_1M_1 phase while it is of comparable magnitude to the 0.65 eV/molecule of the CYA network. Incorporating CYA into an existing M network to form a CYA_1M_3 structure is thus energetically favorable. The formation of a CYA_1M_3 network may be explained as an intermediate step to convert to a thermodynamically stable CYA_1M_1 binary mixture phase. One may speculate whether the added CYA molecules are embedded in the pores of the existing M islands upon direct impingement from the gas phase or primarily interdiffuse from the edges of the islands after deposition on the free terraces. Experiments performed at low CYA dose indicate that the latter mechanism is dominant, since intermixing is primarily observed at the perimeters of the M islands while the M structure is unperturbed in the central areas of the islands. This would be consistent with the observation that nearly no binary mixture phase is observed when depositing M on top of existing CYA networks, due to the higher binding energies of the CYA networks and associated problems with incorporating a molecule into it.

4.3.3 Summary

Systematic studies with variation of the ratio of CYA to M and annealing temperatures show that the simultaneous co-deposition also results in another novel phase as shown in Fig. 4.9(g) which intermixes with the 1:1 phase, but with very few fractions comparing to the 1:1 phase. This novel phase can be identified as 3:1 phase of CYA:M, where the central cyclic CYA hexamer is unexpected and not observed for the pure CYA structure. We can then summarize the experimental results and theoretical calculations about the coadsorption of CYA and M system on Au(111) as illustrated in Fig. 4.9 and Fig. 4.10, respectively. We speculate that these two novel rosette motifs could be kinetically trapped during deposition on the surface. It can be seen from Fig. 4.10 that intermixing CYA and M always have the energy gain compared with the individual components. The detailed analysis of the kinetic effects on this system is still under investigation. By quantifying the hierarchy of homo- and heteromolecular interaction strengths, we have gained insight that can guide future efforts towards using this important complementary hydrogen-bonding motif in the synthesis of self-assembled surface nanostructures.

4.4 SV-21 and its derivative on Au(111)

4.4.1 Introduction

After investigation of the individual small building blocks (CYA, DEB, and BuCYA) and the coadsorption system of CYA and M in the last sections we go on for the next step by exploring the big building blocks (SV-21 and its derivative) of the rosette supramolecular complex. The stability against fragmentation of SV-21 sublimated onto a Au(111) surface under UHV conditions has been investigated by STM.

Adsorption and organization of molecules at the vacuum-solid interface [97] have received particular attention for fundamental studies, motivated by the high degree of cleanliness achievable, the large suite of vacuum-based surface science analysis techniques that can be employed, and the superior control of substrate temperature and coverage. Difficulties in this bottom-up self-assembly route arise, as larger and more complex molecular building blocks are being studied. In particular thermal fragmentation during vacuum sublimation or induced breaking due to molecule-substrate interactions during/after landing onto surfaces may occur and prevent formation of desired nanostructures [36,190]. Although advanced deposition strategies have successfully been employed to alleviate these problems, such as pulsevalve [191] or electrospray [192] injection of dissolved molecules as well as molecular soft-landing [193] by mass-spectrometry methods, it is nevertheless of general interest to explore comparatively simple routes toward stabilization of large organic compounds on surfaces.

Using the STM we here show that the stability against fragmentation of a large organic compound (SV-21) sublimated onto a Au(111) surface UHV conditions can be significantly enhanced by coordinating it to gold atoms prior to deposition. Vacuum deposition of metal-containing organic compounds has previously been achieved in several instances [36,170,190,191], but this is to our knowledge the first time that the incorporation of coordinated metal atoms is shown explicitly to have a stabilizing effect. The compounds used in this study (calix[4]arene dimelamine derivatives, see Fig. 4.11a and Fig. 4.12a) have previously been investigated as building blocks in liquid-phase self-assembly of the hydrogen bonded “rosette” complexes [16].

4.4.2 Results and discussion

Deposition of the gold-containing complex C1 (at 360 K) dominantly leads to regular domains as shown in Fig. 4.11b, coexisting with a smaller fraction of disordered phase. The regular domains consist of v-shaped entities stacked to form densely packed lamellae. The individual entities are imaged as one central protrusion with two arms extending from it, each terminating in a region of enhanced contrast in the STM images. This STM signature fits well with the structure of intact C1, and a schematic adsorption model for the lamellae is displayed in Fig. 4.11d. The distance between the bright features at the end of the two arms is $22 \pm 1.5 \text{ \AA}$, which, by comparison to the molecular model of Fig. 4.11d, suggests that these features can be attributed to the coordinated gold atoms.

Considering that C2 only deviates from C1 by removal of the coordinated gold atoms, we anticipated to find a similar structure after deposition of this compound. Instead, however, we observed a considerably less-ordered surface morphology as

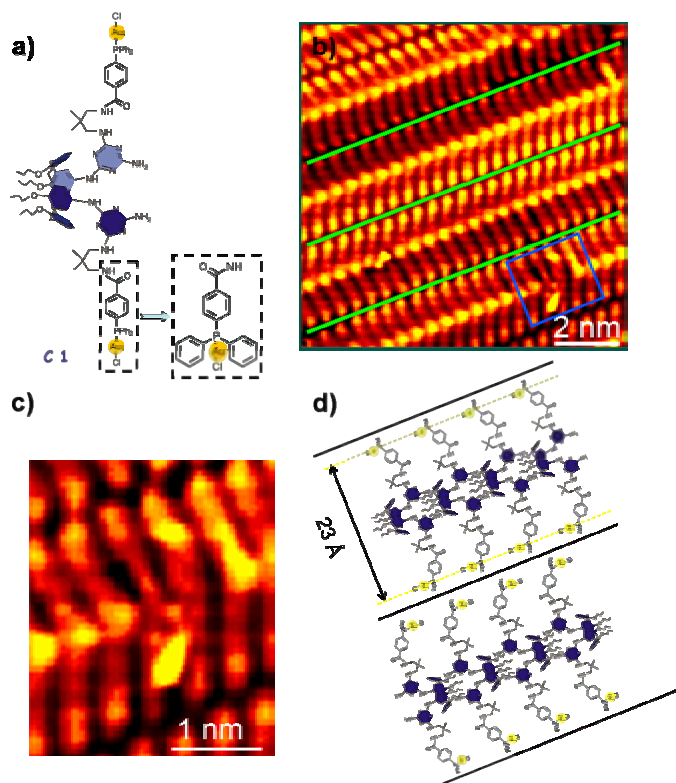


Figure 4.11: (a) Gold-functionalized compound (**C1**) consisting of a central head formed from a calix[4]arene moiety connected to two identical arms, each starting at a melamine unit and terminating in a triphenylphosphine group that coordinatively binds a Au(I) atom. (b) STM image showing the well-ordered lamella structure formed by **C1** (green lines indicate lamellae boundaries). The two molecular arms are imaged with slightly different apparent heights (by 0.3 Å), which is attributed to the 3D conformation of **C1** as indicated by light/dark blue colors in (a). $I_t=0.4$ nA, $V_t=1250$ mV. (c) Zoom-in on the region indicated in (b) showing tip-induced fragmentation. (d) Proposed molecular model for the lamellae. The distance between gold atoms at the terminal of the molecule is 23.3 Å. The experimentally observed periodicity along the lamellae (4.8 ± 0.5 Å) is less than that of the adsorption model, suggesting that the calix[4]arene head unit adopts a more upright-standing orientation than shown in the model.

displayed in Fig. 4.12b. The dominating features are (i) bright clusters which appear to be pinned at the ridges of the Au(111) herringbone reconstruction and (ii) domains of regularly spaced stripes occupying both fcc and hcp regions of the Au(111) substrate and oriented along two main directions (indicated by green arrows in Fig. 4.12b). The stripes have a narrow size distribution (Fig. 4.12c) with a mean length of 21.5 ± 1.5 Å. The cluster sizes predominantly lie in the range from 60 to 100 Å² (Fig. 4.12d). The ratio between the number of stripes and clusters is approximately 3:1 (445:132 as determined from Fig. 4.12b). We interpret these features as the result of fragmentation of **C2**. Tentatively, we suggest that fragmentation occurs at the two equivalent amine bonds (marked with red dashed lines in Fig. 4.12a) and that the two resulting arm fragments, each of ~ 11.3 Å extent, dimerize to form the observed stripe features of roughly the

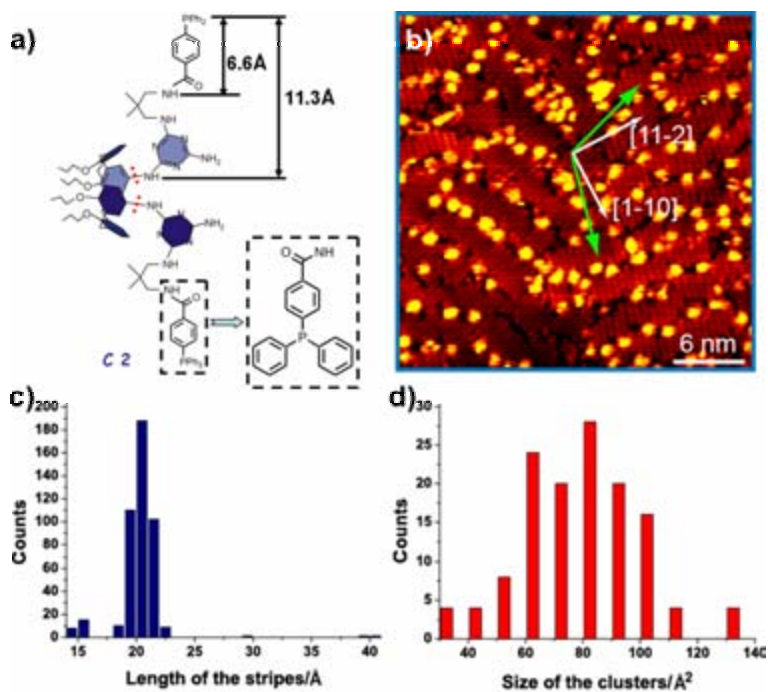


Figure 4.12: (a) Triphenylphosphine calix[4]arene derivative (**C2**) deviating from **C1** by the lack of coordinated gold atoms. Approximate molecular dimensions are indicated. (b) STM image of the surface morphology after deposition of **C2**. $I_t=0.4$ nA, $V_t=1250$ mV. (c) Histogram over the length of the observed stripes. (d) Histogram over the lateral size of the observed clusters.

double length e.g. through hydrogen bonding of the melamine groups of **C2** [96]. The observed clusters are accordingly ascribed to several nucleated calix[4]arene head-units.

The stability of the compound **C1** was probed directly by molecular-scale manipulation with the STM tip. By performing a line scan over an intact **C1** molecule at tunneling parameters that bring the tip close to the surface ($I_t = 1.5$ nA, $V_t = 200$ mV), the bright head can be pushed to the side while the two arms remain relatively unperturbed on the surface (see Fig. 4.11c). This indicates that also **C1** is particularly labile to fragmentation at the position where the head and arms are connected, and supports the conclusion that the structure observed for **C2** is due to fragmentation at the amine bonds. Overall more than 20 distinct sample positions (each corresponding to ~ 500 deposited molecules) were examined without finding any evidence for intact **C2** molecules, while for **C1** $\sim 90\%$ of the deposited compounds were found in the ordered regions ascribed to intact molecules. We therefore conclude that the stability of the gold-coordinated compound **C1** is significantly enhanced compared to the compound **C2** without gold atoms.

The stabilization of **C1** may occur either during thermal sublimation or during/after adsorption to the surface as observed previously [36]. We find it most likely that the stabilizing effect occurs on the surface since (i) the coordinated gold atoms are peripheral to the compound and thus have no obvious stabilizing effect, and (ii) the sublimation temperature of 360 K is not particularly high compared to the anticipated stability against pyrolytic dissociation for these compounds. We speculate that the

dissociation is induced by charge transfer between molecule and substrate which may be affected by the presence of the coordinated Au(I) atoms, leading to a larger stability of C1.

4.4.3 Conclusion

In conclusion, the described results suggest a new route toward self-assembly of molecular nanoscale structures from large organic building blocks and warrants further experimental or theoretical studies into the origin and generality of this unanticipated stabilizing effect.

4.5 Rosette assembly SV-22 on Au(111)

After characterizing both the small building blocks and big building blocks we then explored the transferability of the whole rosette supramolecular complex to the vacuum/solid interface.

After deposition of SV-22 large well-ordered islands were observed as shown in Fig. 4.13a. A close-up STM image (Fig. 4.13c) clearly shows that this structure is different from the previously discussed structures formed by SV-21 and DEB. So we believe the observed structure shown in Fig. 4.13c should be associated with deposition of SV-22. However, the line scan taken in Fig. 4.13a rules out the possibility that the structure is formed by intact SV-22, since the profile (cf. Fig. 4.13b) shows that the island is only about 3 Å in height. By comparing with the molecular model and dimensions shown in Fig. 4.13d one should expect an apparent height of about 1.3 nm for a ‘face-on’ manner or about 3 nm for an ‘edge-on’ manner adopted by the intact SV-22. The structure shown in Fig. 4.13c exhibits lateral periodicity of 3 ± 0.3 nm (periodicity is indicated by the green lines), which fits well with the width of SV-22. In addition, the periodicity along the rows is 1.5 ± 0.1 nm which is in good agreement with the thickness of SV-22. Both periodicities of the observed structure show the signature of SV-22 except for the height. We thus think the observed structure is related to partially decomposed SV-22, which is broken either during the thermal sublimation process or during the landing process on the surface. We find that the dissociation process most likely occurs on the surface, as the sublimation temperature is far below the decomposition temperature for SV-22 examined during the synthesis process. It is interesting that by annealing the self-assembled structure associated with SV-22 (Fig. 4.13a) to 370 K a polymerized filamentary structure was formed on the surface as shown in Fig. 4.14 and it is stable at least up to 900 K. Moreover, codeposition of DEB and SV-21 does not result in the observed well-ordered structure (Fig. 4.13a,c) associated with SV-22 complex. The thermal treatment experiments further confirm that anneal of the coadsorbates of DEB and SV-21 does not form the above-mentioned filamentary structure (Fig. 4.14).

In summary the rosette supramolecular complex was tried to deposit on the surface from the conventional thermal sublimation method, and well-ordered structure formed on the surface, which could be associated with partially decomposed SV-22 complex. The results presented in this work would warrant further studies on proceeding delicate chemical modifications on SV-22 complex to make it more robust or with other functional groups embedded that are responsible for the soft-landing process toward building the desired 3D supramolecular architectures on surfaces.

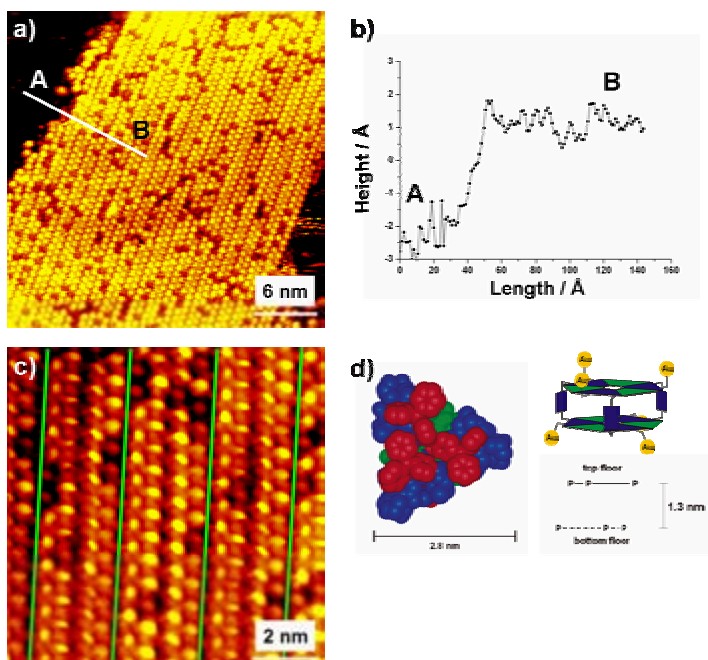


Figure 4.13: (a) STM image of the overview structure associated with deposition of SV-22. (b) Profile of the line scan shown in (a). (c) A zoom-in STM image shows the detailed molecular structure associated with deposition of SV-22. $I_t = -0.4$ nA, $V_t = -1250$ mV (d) molecular model of SV-22 together with the dimensions.

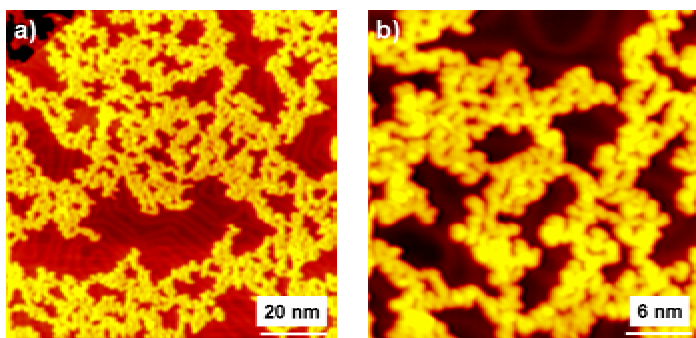


Figure 4.14: Filamentary structure formed by annealing at 370 K after deposition of SV-22, which is stable at least up to 900 K. $I_t = -0.4$ nA, $V_t = -1250$ mV.

CHAPTER 5

Molecular mould on Au(111) and Cu(110)

In this chapter a systematic investigation of adsorption of Lander-type molecular mould on Au(111) and Cu(110) surfaces will be described in detail. As a first step, the Lander molecule was deposited on both Au(111) and Cu(110), and the molecule-substrate interactions on both substrates were directly probed by STM manipulation. Then we investigated the self-assembled nanostructures of Lander molecules (with/without diaminopyridine functional group) on Au(111). As the next step, we studied the complex system of combination of Lander molecule with Ni coordinated PTCDI supramolecular matrix.

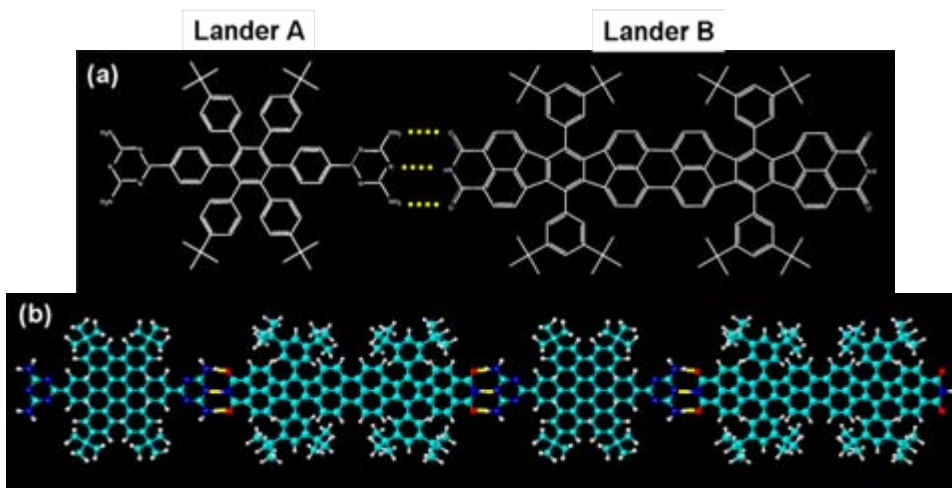
5.1 Aim of the project

The aim of this project is to create 1D well-defined metallic nanostructure on solid surfaces in relation to the field of molecular electronics engineering. The strategy applied here is that we need to form 1D supramolecular chains on surfaces that could hopefully serve as moulds to accommodate the metallic atoms underneath. In the next step one can remove the covered molecules and only the formed metallic wires survive on the surface. To approach this direction joint efforts are required. We decided to choose Lander molecules as candidates, since it was shown that Lander molecules were able to restructure the step edges of Cu(110) surface [23], and to trap metallic adatoms underneath due to the decoupling from surfaces by the spacer bulky groups [196]. In order to form 1D supramolecular chains on surfaces two kinds of functionalized Lander molecules were synthesized in the group of A. Gourdon at Toulouse. As seen from Scheme 5.1 two Lander molecules are respectively embedded with diaminopyridine and diimide moieties with the capability of forming triple complementary hydrogen bonds and subsequently forming the ABAB-type supramolecular chains. Such classic interactions have been discussed in detail in a model system of melamine and cyanuric acid in Chapter 4. Since this is still an ongoing project we have presently characterized the Lander A ($C_{64}H_{68}N_{10}$, bis-diaminotriazine, referred to as DAT in the following) on both Cu(110) and Au(111). Furthermore, we have picked up PTCDI (with the same diimide groups as Lander B) as a simpler candidate to perform the coadsorption experiment with DAT to investigate the feasibility of forming 1D supramolecular chains. These will be briefly described in the following sections.

5.2 DAT on Cu(110) and Au(111)

5.2.1 Introduction

In the first step, we investigated DAT adsorbed on both Cu(110) and Au(111) surfaces by means of high-resolution STM imaging and manipulation to probe the relevant molecule-substrate interactions on both surfaces under UHV conditions. It is generally expected that adsorbed molecules on Au(111) would feel a very small corrugation of the potential energy surface, which is in contrast to the anisotropic Cu(110) surface, where specific favorable adsorption sites or larger corrugation would impose on the adsorbed molecules. As shown in Fig. 5.1(a), the DAT molecule consists of hexaphenyl benzene attached with four tert-butyl lifting groups as spacer legs and two diamino-pyridine functional groups for potential formation of hydrogen bonding, where the phenyls can rotate around their σ bonds resulting in a non-planar conformation for the molecular backbone. The results presented here show by lateral STM manipulation that the DAT molecule can be translated and rotated on the Cu(110) surface, and only adopt four favorable orientations with respect to the underlying Cu(110) lattice, and the DAT molecule can be manipulated from lower terrace to upper terrace of Cu(110). On the contrary, the DAT molecule is experimentally demonstrated to be rather mobile on Au(111) surface and by triggering the molecule by STM tip it was found to run out of the scanning regime.



Scheme 5.1: (a) Schematic models of Lander A (DAT) and Lander B molecules, respectively. (b) Proposed model for 1D molecular chain formed by Lander A and Lander B via complementary H-bonds.

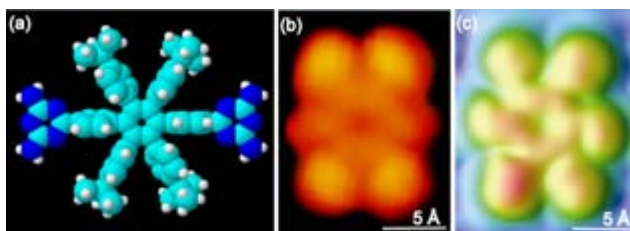


Figure 5.1: (a) Space-filled model of bis(diaminotriazine) (DAT) molecule ($C_{64}H_{68}N_{10}$) where the carbon, hydrogen and nitrogen atoms are represented respectively in pale blue, white and blue. (b) Typical high-resolution STM image of an individual DAT molecule on Cu(110) ($I_t = -0.66$ nA, $V_t = -1.73$ V). (c) ESQC-simulated STM image of the DAT on Cu(110) using the same tunneling conditions as the experimental result in (b).

5.2.2 Results and discussion

DAT molecules were deposited at 510 K onto the substrate held at RT. Fig. 5.1(b) presents a high-resolution STM image of a DAT molecule on Cu(110), showing four bright lobes in the corner forming a rectangular shape ($11.0 \text{ \AA} \times 6.5 \text{ \AA}$), two dim lobes on each sides and some subtle protrusions in the centre. The morphology of this molecule on Cu(110) is identical to that on Au(111). We interpret that each bright lobe corresponds to tunneling through one of the four tert-butyl groups, while the side dim lobes and subtle protrusions are attributed to the hexa-phenyl rings, which are connected with the central benzene by σ bonds. There is, however, no obvious feature that can be attributed to the diamino-pyridine groups in this image. Under the same tunneling conditions as those for the result in Fig. 5.1(b) (sample voltage, -1.73 V; tunneling

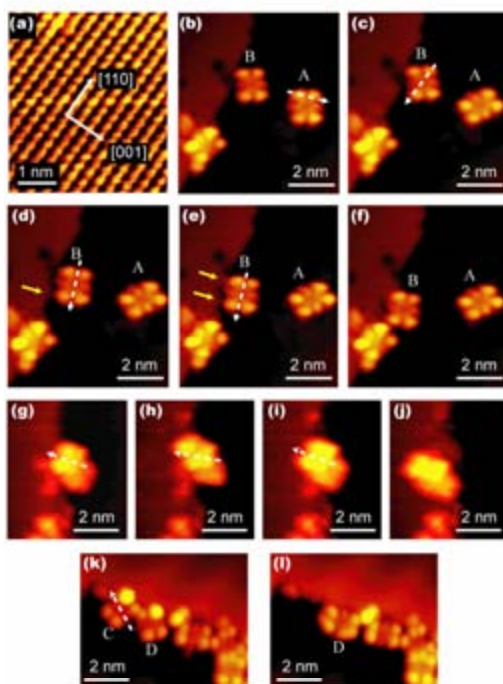


Figure 5.2: High-resolution STM images showing the atomically resolved Cu(110) surface in (a) and the manipulation sequences of individual DAT molecules on Cu(110) in (b-j) and on Au(111) in (k, l). On Cu(110), three different manipulation processes can be performed: the DAT molecule marked 'A' can be rotated on terrace as shown in (b,c); molecule marked 'B' can be moved along the step edge while changing its orientation as shown in (c-f); the molecule can even climb over the step edge from lower to upper terrace as shown in (g-j). On Au(111), the DAT molecule is relatively mobile. As shown in (k,j), the molecule 'C' can be easily removed from the step edge triggered by STM tip while the neighboring molecule 'D' was rotated simultaneously.

current, -0.66 nA) on Cu(110), theoretical simulations have been performed using elastic-scattering quantum chemistry (ESQC) [197] combined with molecular mechanics (MM2). As seen from the simulated STM image in Fig. 5.1(c), the contribution of diamino-pyridine groups to the tunneling current is apparently minor. This is in good agreement with the experimental result. The invisibility of diamino-pyridine groups may result from decoupling from the substrate by the spacer legs of a DAT molecule.

The high-resolution STM images in Fig. 5.2 present the manipulation sequences of individual DAT molecules on Cu(110) and Au(111), with the white dash arrows showing the directions of the applied operations. Fig. 5.2(a) shows an atomically resolved clean Cu(110) surface, where the two close-packed directions are indicated. At low temperature (~ 110 K) the orientation of the single DAT molecule (marked 'A' in Fig. 5.2(b,c)) can be manipulated on a Cu(110) terrace from -45° to 15° with respect to the [110] direction of the substrate. Based on the statistical analysis of STM manipulation results of both individual DAT and DAT dimer on terraces, it is found that there are only four different stable adsorption orientations of DAT on Cu(110), i.e. the

longer molecular axis is -45° , -15° , 45° , 15° off, respectively, with respect to the [110] direction of the substrate.

As shown in the sequence of Fig. 5.2(c-f), the molecule 'B' is steered by STM tip and displaced gradually along the step edge of Cu(110) from the top toward another DAT molecule adsorbed on the step edge near the bottom of the images. During this lateral translation, the orientation of the molecule 'B' is simultaneously varied. Notice that compared to the smooth and flat step edge along [110] in Fig. 5.2(c), there are protrusion formations at the step edge induced by the interaction with molecule 'B' during movement, as pointed out in Fig. 5.2(d) and (e) by the yellow arrows. The ability of Lander molecules to mould nanostructures at the step edge of Cu(110) have been reported previously [23]. In those cases the reshaping of the step edges occurred at room temperature. However, the results presented here reveal that even at low temperature (~ 110 K) the DAT molecule is still capable of affecting the shape of the step edge. But this influence is temporary and reversible, i.e. once the molecule is removed the protrusions vanish.

The consecutive images shown in Fig. 5.2(g-j) demonstrate that by manipulating a single DAT molecule to climb over the step edge from lower terrace to upper one, various contact configurations of DAT with respect to the step edge can be created. In Fig. 5.2(g), the obvious difference in the apparent height of the four lobes of DAT suggests that the molecule is tilt and leans at the step edge. Through continuous movements triggered by the STM tip, the molecule climbs up step by step, and the whole molecule is finally moved to the upper terrace. It is noticeable that the intramolecular conformation is also apparently changed during the manipulation process revealing the flexibility of the molecular backbone of DAT molecule.

As a comparison, similar STM manipulation is also performed on Au(111) at the same low temperature. In Fig. 5.2(k), the molecule 'C' is supposed to be rotated at the step edge. Surprisingly, after being triggered by the STM tip molecule 'C' is completely gone from the step edge and even diffuse out of the scanning region. At the same time, as seen in Fig. 5.2(l), this manipulation on molecule 'C' also induces the rotation of its neighbouring molecule 'D' from sort of leaning at the step edge to be parallel to it. This manipulation process further confirms that the local interaction between the DAT molecule and Au(111) substrate is obviously lower than that for Cu(110).

5.2.3 Conclusion

Through lateral STM manipulation various contact configurations of DAT molecule at the step edge of Cu(110) were engineered in a controlled manner; through rotation, lateral translation, and hurdle over the step edge. However, on Au(111) at the same temperature regime (~ 110 K), the DAT molecule is facile to move away under STM manipulation. This study provides direct experimental evidence on choosing appropriate molecular components and substrates towards future applications on molecular electronics.

5.3 Lander A (with/without diaminopyridine functional groups) on Au(111)

In this section the results of Lander A (with/without diaminopyridine functional groups, as shown in Fig. 5.3) supramolecular nanostructures on Au(111) will be briefly presented. As described previously this Lander A molecule is embedded with two diaminopyridine functional groups with the capability of forming hydrogen bond [96]. One might expect the formation of 1D hydrogen-bonded molecular chain as shown in Fig. 5.4. However, experimentally we did not observe such 1D molecular chain, but instead, three supramolecular networks were found, which might originate from interplay between steric effect, vdW interactions and hydrogen bonding.

Fig. 5.5a shows the close-packed structure formed by direct deposition of Lander A molecules on the Au(111) surface held at room temperature. In this structure the molecules adopt a crisscross arrangement with respect to each other. As shown in the tentative model (see Fig. 5.5b), the diaminopyridine groups are placed between two tert-butyl groups of nearest neighbouring molecules. This arrangement may simply be dominated by vdW close-packing interactions.

After deposition of Lander A molecules at high coverage and followed by subsequent anneal at $\sim 100^\circ\text{C}$ another two phases were formed as shown in Fig. 5.5c and e. For the four-blade dimer structure (cf. Fig. 5.5c) and the six-blade dimer structure (cf. Fig. 5.5e), the Lander A molecules form more complex arrangements that may contain elements of H-bonding. An elementary structural motif in both structures is a Lander A dimer in which the anticipated H-bonding between the diaminopyridine groups may be achieved (the dimers are indicated by bars in Fig. 5.5c and e). The observed networks can be rationalised from arranging these dimer units in different ways (cf. Fig. 5.5d and f for the proposed molecular models).

For the complementary experiment of identifying the role of the diaminopyridine groups in the formation of the above-mentioned networks, we further performed the experiment by deposition of another Lander molecule without diaminopyridine functional groups (cf. Fig. 5.3d) on the surface. As a result, we found this Lander molecule formed another close-packed structure direct after deposition as shown in Fig. 5.6a along with a tentative model shown in Fig. 5.6b. It illustrates that in this structure the molecules form compact rows in one direction (possibly via the interactions between phenyl rings of the neighboring molecules) and laterally interdigitate together by the tert-butyl groups of the neighboring molecules.

As the next step we are interested in receiving input from theoretical point of view to see if the diaminopyridine groups can be rotated and tilted in 3D to optimise the hydrogen bonding formation in Lander A dimers. This is an interesting aspect as the Lander-type molecule has bulky tert-butyl spacer groups that lift the molecular board, and thus the attached diaminopyridine functional groups, away from the surface. Hence, the diaminopyridine groups should have more conformational flexibility than 2D planar compounds adsorbed directly at the surface.

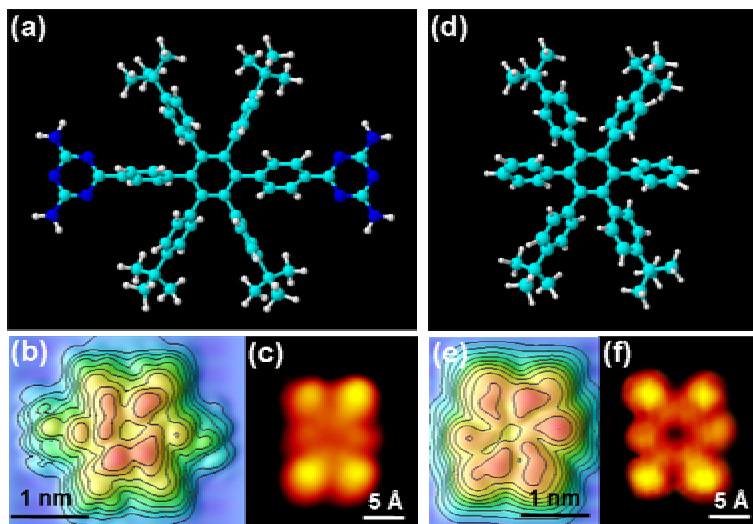


Figure 5.3: (a) Molecular model of Lander A molecule. (b) ESQC simulated STM image of Lander A molecule compared with the experimental result as shown in (c). (d) Molecular model of Lander A molecule without diaminopyridine functional groups. (e) ESQC simulated STM image of Lander A molecule without diaminopyridine functional groups as compared with the experimental result as shown in (f).

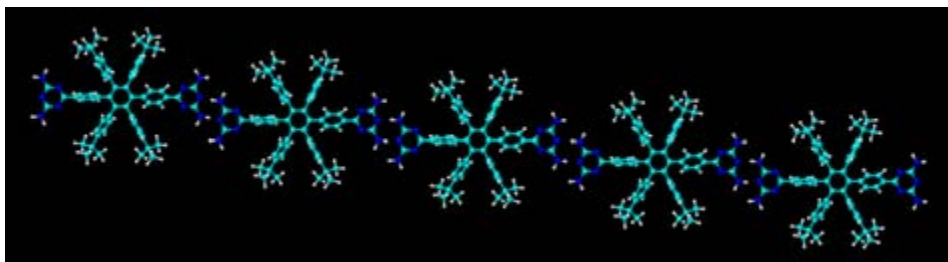


Figure 5.4: The expected 1D hydrogen-bonded supramolecular wire formed by Lander A molecules.

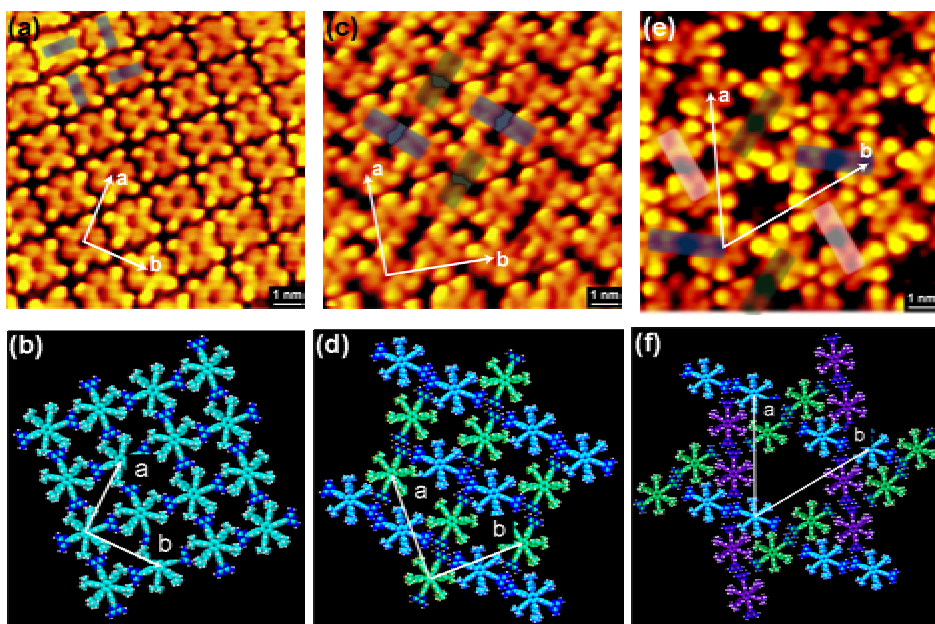


Figure 5.5: (a) High-resolution STM image of the close-packed structure formed by Lander A molecules along with the tentatively proposed molecular model as shown in (b). The bars in (a) show the molecular arrangement. (c) High-resolution STM image of the four-blade dimer structure along with the tentatively proposed molecular model as shown in (d). The bars in (c) show the Lander A dimers arrangement. Different colour coding in (d) helps to distinguish different dimers. (e) High-resolution STM image of the six-blade dimer structure along with the tentatively proposed molecular model as shown in (f). The bars in (e) show the Lander A dimers arrangement.

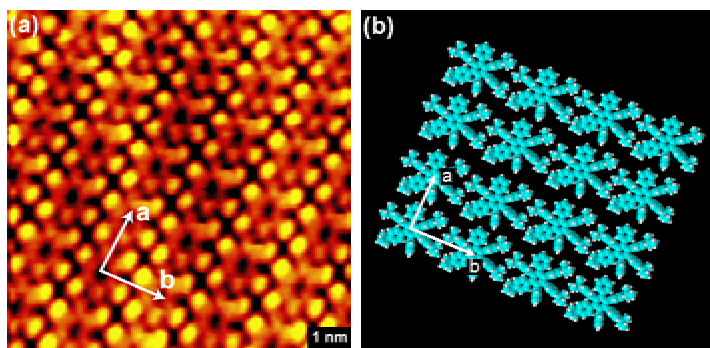


Figure 5.6: (a) High-resolution STM image of the close-packed structure formed by Lander A molecule without diaminopyridine functional groups. (b) Tentatively proposed molecular model for this structure.

5.4 Lander A caged by Ni-PTCDI matrix on Au(111)

To explore the possibility of forming hydrogen bonded supramolecular chains by Lander A and PTCDI codeposition experiment was performed. Furthermore, we have also extended the complexity of the studied system by dosing Ni atoms together with PTCDI to investigate the metal ligand interactions. In this section a triple-component system including Ni atoms (Fig. 5.7a), PTCDI molecules (Fig. 5.7b), and Lander A molecules (Fig. 5.3a-c) will be briefly discussed. When depositing Ni atoms and PTCDI molecules simultaneously or sequentially onto a clean Au(111) surface, we have observed Ni-PTCDI clusters, filamentary structures with different types of junctions, and 2D matrix. Interestingly, coadsorption of the three components shows that the Lander A molecules can be caged and aligned by PTCDI-Ni matrix.

After deposition of PTCDI on Au(111), large islands with ordered structure are formed as shown in Fig. 5.7b. The proposed model superimposed on the STM image suggests that the molecule stripes (along vector **a**) are formed by the double hydrogen bond between diimide groups of the neighbouring molecules and those stripes are laterally (along vector **b**) packed by vdW interactions into 2D ordered structure.

To study the metal-ligand interactions between Ni and PTCDI we first deposited Ni atoms on the Au(111) surface as shown in Fig. 5.7a. As can be seen Ni clusters mainly nucleated at the elbows of the Au(111) herringbone reconstruction. Codeposition of Ni and PTCDI from low coverages to high coverages, different Ni-PTCDI coordinated structures can be formed. At low coverage of Ni atoms and PTCDI molecules PTCDI-Ni clusters can be formed, which nucleated at the elbows as well (Fig. 5.8a). The majority of clusters consists of Ni coordinated PTCDI trimer. The inset of Fig. 5.8a shows the proposed model of such trimer structure superimposed on the high-resolution STM image. At a higher coverage, one-dimensional filamentary structures (which are interconnected somehow) were formed as shown in Fig. 5.8b. Some characteristic junctions extracted from the filamentary structures are shown in Fig. 5.8e along with the superimposed proposed models. It is noticeable that the Ni coordinated PTCDI filaments do have the similar hydrogen bonding situation to the case of pure PTCDI structure (cf. Fig. 5.7b). However, such Ni-coordinated PTCDI filaments repulse each other to prevent formation of close-packed structure. At even higher coverage and an appropriate ratio of PTCDI and Ni, a 2D matrix can be formed as shown in Fig. 5.8c. As seen from the proposed model shown in Fig. 5.8d the molecular rails in the matrix form the same hydrogen bonded and Ni coordinated structure as the case for Ni-PTCDI filaments), and the molecules in between the molecular rails are also coordinated by Ni atoms as crossties with two different orientations. The matrix is thus stabilized by the interplay between hydrogen bonding and metal-ligand interaction.

Surprisingly, after codeposition of the triple components of Lander A, PTCDI and Ni and followed by anneal @ $\sim 100^\circ\text{C}$ we found that some of the Lander A molecules are caged and thus aligned by the molecular rails of Ni-PTCDI matrix (cf. Fig. 5.9). The detailed structural models are still under investigation from theoretical point of view. However, codeposition of Lander A with PTCDI does not turn out an ordering formation, which is in contrast to our expectation that they will form hydrogen bonded structure through the diimide groups of PTCDI and diaminepyridine groups of Lander A. This could be attributed to the height difference between Lander A and PTCDI adsorbed on the surface, which hampers these two functional groups to couple from each other. So our next step is to first study the Lander B individually and try to codeposit Lander A

and Lander B on the proper surface to explore the feasibility of forming desired hydrogen-bonded structures.

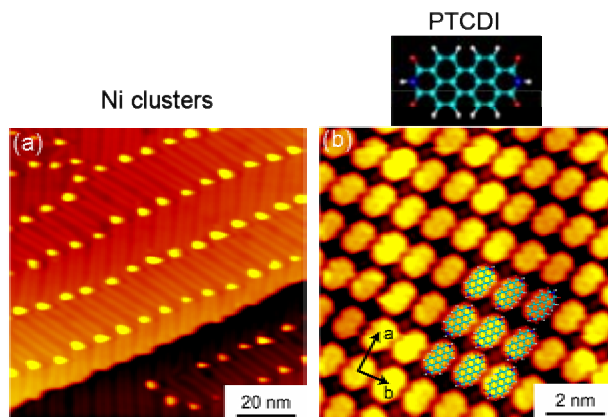


Figure 5.7: (a) STM image shows that Ni clusters grow at the elbow sites of the Au(111) surface. (b) PTCDI islands form on the terrace of the Au(111) surface. The tentatively proposed model is superimposed on the high-resolution STM image.

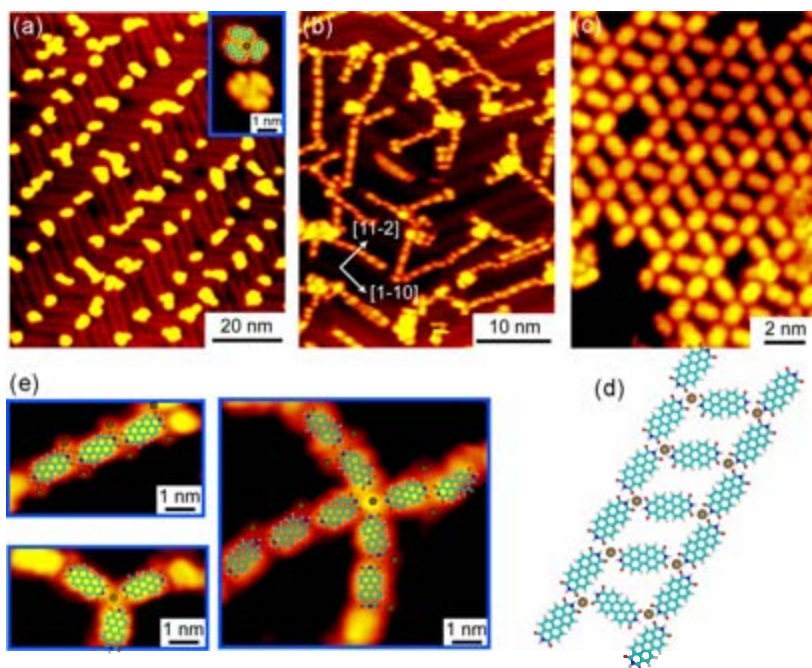


Figure 5.8: Codeposition of Ni and PTCDI from low to high coverage shows the formation of Ni-PTCDI clusters nucleated at the elbows of the Au(111) (a), Ni-PTCDI filamentary structures (b), and 2D Ni-PTCDI matrix (c) together with tentatively proposed model (d). (e) Tentatively proposed models of Ni-PTCDI coordinations are superimposed on the high-resolution STM images of filament and different junctions extracted from the filamentary structures.

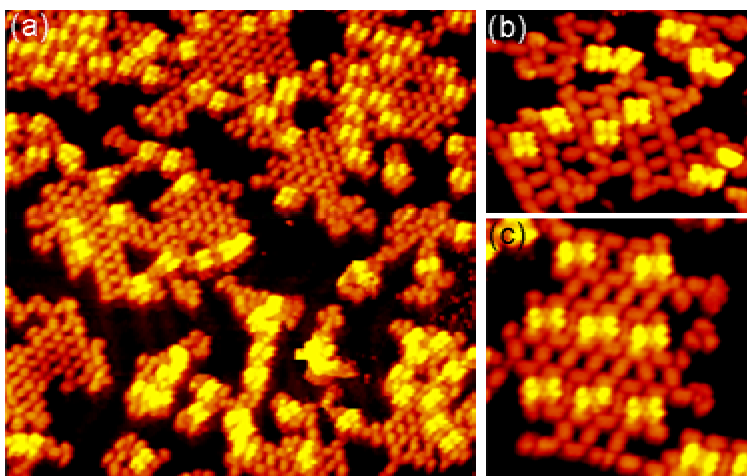


Figure 5.9: (a) codeposition of triple components of Lander A, PTCDI, and Ni shows that the Lander A molecules are caged by the Ni-PTCDI matrix and thus aligned by the matrix. The high-resolution STM images are shown in (b,c).

CHAPTER 6

NDCA on Ag(110)

2,6-naphthalene-dicarboxylic acid (2,6-NDCA) was adsorbed on a Ag(110) surface with an average terrace width of only some tens of a nm. STM result shows that the adsorbates self-assemble into one-dimensional mesoscale length chains. These extend over several hundred nanometers and thus the structure exhibits an unprecedented tolerance to monatomic surface steps. DFT and XPS explain the behavior by a strong intermolecular hydrogen bond plus a distinct template-mediated directionality and a high degree of molecular backbone flexibility.

6.1 Introduction

It is well known that organic molecules can self-assemble on surfaces through hydrogen bond formation [2,11,13,50-52,66,136,154,198-210]. Self-assembly, besides being of fundamental scientific interest in itself, is thought to be a viable pathway towards functional supramolecular architectures in nanotechnology. One challenge in the field is to design self-assembled structures which are insensitive to native surface defects. As an example, on perfect surfaces the formation of one-dimensional (1D) structures can be controlled relatively easily [2,11,13,50,198,199], while on surfaces with many structural defects such as step edges the formation of 1D structures represents a much greater challenge. The defects can hinder the mesoscopic-scale ordering of the molecular building blocks and make a proper functioning of the assembly impossible. Here we show how hydrogen bonding of organic molecules on a stepped metal surface leads to linear self-assembled structures, "1D chains", that extend into the mesoscale length regime. The system is tolerant to monoatomic step edges.

6.2 Results and discussion

The 1D chains, formed upon adsorption of sub-monolayer (ML) amounts of 2,6-naphthalene-dicarboxylic acid (NDCA, $C_{10}H_6(COOH)_2$) on a stepped Ag(110) single crystal surface, were characterized by STM and XPS. Sub-ML amounts of NDCA were sublimated onto the room temperature sample from a thermal evaporator at ~ 530 K. The large-scale STM topograph in Fig. 6.1(a) reveals that the NDCA self-assembly on Ag(110) results in close-to-straight 1D chains in the $[-110]$ direction, which extend on the mesoscale length regime in spite of the stepped character of the surface. An analysis of the STM image yields a lower limit to the average 1D chain length of about $0.14 \mu\text{m}$. This is a lower limit since ~ 50 % of all 1D chains extend into the surrounding area not imaged. The longest 1D chain is at least $0.65 \mu\text{m}$ long. Owing to their large size, more than 90 % of all 1D chains cross at least one step edge; the average number of steps crossed by a single 1D chain is 2.3 and the highest is 13. 24% of the 1D chains end at the steps. Comparing this to an estimated 5% or less of the total area belonging to the step edges (counting the atoms adjacent to the edge on the terraces) shows that the steps constitute a barrier for the molecular 1D chains. Nevertheless, since the large majority of all 1D chains cross one or more step edges, the continuation of the 1D chains over the step edges is energetically more favorable than the formation of open 1D chains that terminate at the steps.

Figures 6.1(b-c) are STM images of parts of 1D chains on flat terrace regions of the surface. Each bright protrusion in the 1D chains corresponds to one single NDCA molecule. There exist two distinct orientations of the adsorbates, either aligned with $[-110]$ (species A) or slightly tilted with respect to $[-110]$ (species B). Both A and B bind to neighboring molecules along $[-110]$ in a head-to-tail fashion. An analysis of a large number of STM images shows that $\sim 2/3$ of all molecules adsorb as species A and $\sim 1/3$ as species B. In Fig. 6.1(c) an accidental tip change resulted in an STM image with atomic resolution on an uncovered part of Ag(110) and imaging of the NDCA molecules on a covered part. From this image the location of the substrate close-packed rows within the 1D chains (white lines) and the adsorbate-substrate registry can be determined (the black lines indicate two periods of four Ag atoms each). From a detailed analysis of this and

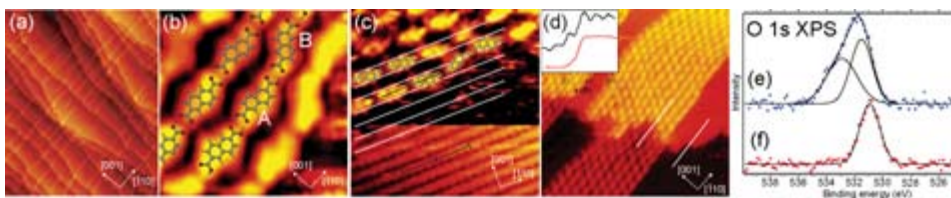


Figure 6.1: STM and XPS results. (a) $6200 \times 7000 \text{ \AA}^2$, $I = -0.39 \text{ nA}$, $V = -220 \text{ mV}$. 1D molecular chains of NDCA on Ag(110). (b) $35 \times 35 \text{ \AA}^2$, $I = -0.25 \text{ nA}$, $V = -185.8 \text{ mV}$. The molecular model stems from the optimization of a gas phase network (see text). (c) $60 \times 60 \text{ \AA}^2$, $I = -0.79 \text{ nA}$, $V = -883.8 \text{ mV}$. Investigation of the registry of NDCA with the Ag(110) surface. (d) $195 \times 195 \text{ \AA}^2$, $I = -0.20 \text{ nA}$, $V = -262.8 \text{ mV}$. The lines indicate the traces of the line scans in the inset. Inset: line scan over an adsorbate-covered step edge (black) and a free step edge (red). The relative alignment of the scans is arbitrary. (e,f) O 1s XPS, (e) $\sim 0.3 \text{ ML}$ NDCA deposited onto Ag(110) at room temperature and not treated any further, (f) 1 ML NDCA deposited onto a room temperature Ag(110) surface and annealed to $200 \text{ }^\circ\text{C}$ for 20 min.

many other STM images (without tip change and atomic resolution, but with simultaneous resolution of the molecules and the substrate close-packed rows) we find that species A is adsorbed with the molecular axis aligned with and centered over the substrate trough. Along [001], i.e., perpendicular to the 1D chains, we find a minimum distance between any two adsorbates of two Ag atomic rows. Species B, in contrast, is rotated by an angle of about 40° to [-110] and positioned with its center on top of the substrate rows. Finally, Fig. 6.1(d) presents an STM image of a 1D chain extending across a step edge. The inserted line scan with a regular structure in the NDCA protrusions across the step edge suggests that the bonding in the 1D chains is largely unaffected by the monatomic step and that the molecules on the lower terraces do not lie flat at the steps.

The O 1s XPS results in Fig. 6.1(e) reveal a broad peak with two components of equal weight. This spectrum was obtained on NDCA sublimated onto a room temperature Ag(110) surface and not further treated, and thus the results directly correspond to the STM measurements of Fig. 6.1(a-d). The two components stem from the two distinct oxygen species of the protonated carboxylic group [211,212]. The larger width of the high binding energy as compared to the low binding energy peak is suggested to be related to the effect of intermolecular hydrogen bonding. Important here is that both components exist and that they have the same spectral weight. This proves that the carboxylic groups are protonated and that the molecules thus cannot form a covalent bond to the Ag substrate. However, owing to the XPS detection limit, the statement is valid only for the majority of molecules, i.e., for the terrace-bonded NDCAs, while a deprotonation of the step-bonded NDCA cannot be excluded so far. DFT will allow us to discard this possibility as described below. After annealing to 200°C only one O 1s XPS peak persists (Fig. 6.1(f)). This shows that all oxygen atoms have become chemically equivalent due to deprotonation and formation of a bidentate bond of the carboxylic group to the substrate. Hence, under the room temperature conditions of the STM experiments a kinetic barrier hinders the deprotonation of the NDCA.

We probed a large number of adsorbate geometries using DFT. The outcome for some of these is summarized in Table 6.1. It should be noted that for the smallest surface unit cells the calculations were performed using two as well as three or four atomic layer slabs of Ag(110), while the systems with large surface unit cells with several NDCAs

No.	Molecular geometry		Figure	2 layer slab	3 layer slab	4 layer slab
1	monomer	P	\parallel $[\bar{1}10]$, on top of troughs	0.31 eV		0.29 eV
2	monomer	P	\parallel $[110]$, on top of atomic rows	0.18 eV		0.17 eV
3	1D chain	P	\parallel $[\bar{1}10]$, on top of troughs	2(a left) 1.41 eV		1.20 eV
4	1D chain	P	\parallel $[\bar{1}10]$, on top of atomic rows	2(a right) 1.20 eV		1.09 eV
5	1D chain	P	\perp $[\bar{1}10]$			0.70 eV
6	monomer	D	covalently bonded, \parallel $[\bar{1}10]$	5.11 eV	4.65 eV	
7	monomer	D	covalently bonded, \perp $[\bar{1}10]$	5.31 eV	4.94 eV	
8	dimer	P	\parallel $[\bar{1}10]$, on top of troughs	0.91 eV		
9	dimer	P	at step edge	2(c) 0.77 eV		
10	two monomers	P	at step edge	2(d) 0.40 eV		
11	dimer	P	centre of molecule on top of step edge	0.50 eV		
12	two monomers	half-D	covalently bonded to step edge	2(e) 2.70 eV		
13	two monomers	half-D	covalently bonded to step edge	2(f) 2.81 eV		
14	gas phase net	P	ratio species A : species B = 3 : 1	2(b)	no substrate: 0.61 eV	

Table 6.1: DFT calculated binding energies per molecule of the indicated systems. The P/D label refers to the protonated/deprotonated state of the adsorbate, half-D to deprotonation of only one of the two molecular carboxylic groups. The monomer labels refers to true monomer calculations in rows 1-2 (using periodic boundary conditions on a large substrate slab), to covalently bonded NDCA on a commensurate substrate slab in rows 6-7, and two adsorbates without hydrogen bond interaction in a dimer calculation in rows 10, 12 and 13. The specification of the orientation refers to the direction of the molecular principal axis. The slab specification refers to the number of substrate layers in the calculation.

only could be modeled using two-layer Ag(110) slabs. The accuracy of the two-layer slab results can be estimated from noting that the binding energy of NDCA in an infinite 1D chain on a Ag(110) terrace only changes from 1.20 to 1.41 eV (Table 6.1, row 3) when going from the four-layer to the two-layer slab. Thus, the use of two layer-slab results in our discussion is justified, in particular since our conclusions are based on the comparison of relative energies obtained in the thin slab calculations. The DFT calculations for the adsorbate geometries at step edges were performed using an NDCA dimer, which made it possible to calculate many different NDCA geometries using a single choice of super cell without the restriction of having to choose an adsorbate cell commensurate with the substrate unit cell. Here we assume that the NDCA-NDCA and NDCA-Ag bond energies within the dimer are unaffected by the absence of the bonds between the dimer and the rest of the 1D chain. This assumption is justified by the finding of a less than 10% increase of the NDCA-NDCA bond strength when moving from the adsorbed 1D chain to the adsorbed dimer. Finally, it is noted that DFT, as well known, does not properly account for the dispersion contribution to the binding energy. From a comparison of the binding energies of benzene to Cu(111) and Cu(110) obtained from DFT to those obtained from Møller-Plesset second-order perturbation theory and/or to experiment, the here used PW91 parametrization can be expected to describe approximately 5 to 25% of the dispersion strength only [213,214]. However, since (i) the binding energy of the investigated systems is dominated by hydrogen bonding with interaction strength larger than the dispersion interaction strength and (ii) the dispersion interaction strength should be similar in all investigated systems, this deficiency does not invalidate our findings.

Figure 6.2(a) (cf. Table 6.1, rows 3 and 4) shows the two most favorable non-covalently bonded NDCA geometries on a Ag(110) terrace. In the calculation the formation of the hydrogen bond was achieved by restricting the unit cell to single molecule on a Ag(110) slab with suitable periodic boundary conditions. In accordance

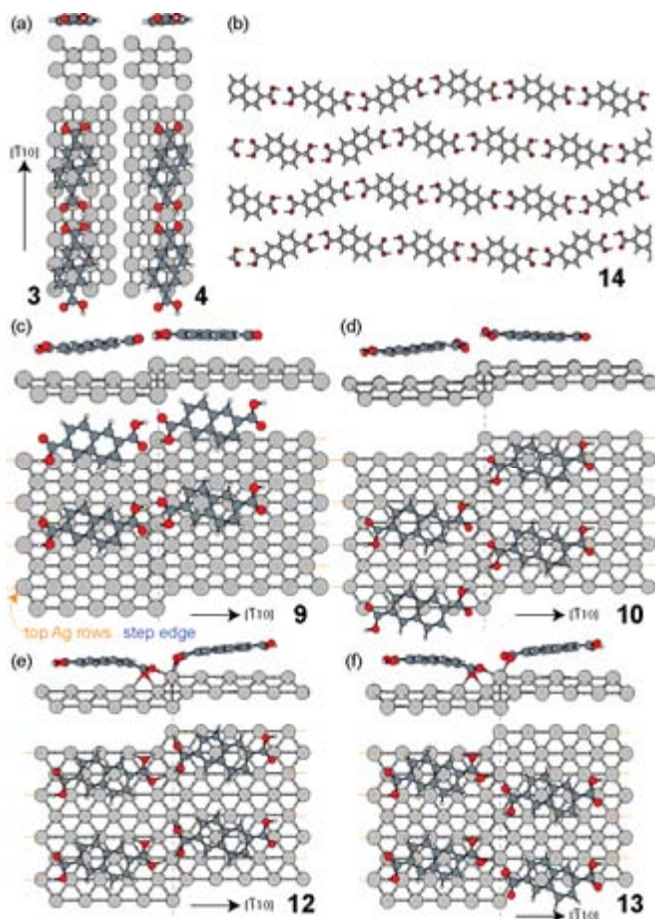


Figure 6.2: DFT results. The numbers refer to Table 6.1. (a) Head-to-head hydrogen-bonded NDCA on top of a substrate trough (left) and a close-packed Ag-row (right). (b) Gas phase net of two species A and B with different orientations corresponding to the adsorbate orientations observed experimentally. (c) to (f) NDCA dimers at a step edge. (c) Most stable configuration of a protonated NDCA dimer at a step edge. (d) Two protonated NDCA without NDCA-NDCA hydrogen bonds. (e) Two deprotonated NDCA molecules in registry cross the step edge. (f) Two deprotonated NDCA molecules out of registry across the step edge.

with the experimental observation of species A, the geometry of Fig. 6.2a (left) with the molecules aligned over the Ag close-packed troughs is most stable. From a comparison of the chain configuration (row 3 in Table 6.1) with an isolated NDCA monomer (row 1) it is seen that the strength of the NDCA-NDCA double bond in the infinite 1D chain amounts to (binding energy of one NDCA in the 1D chain – binding energy of an isolated NDCA) = $(1.20 - 0.29) \approx 0.9$ eV (1.1 eV on two-layer slabs), much more than the molecular bonding contribution along [001], which we have calculated to be less than 0.1 eV/NDCA [215]. The NDCA-NDCA double hydrogen bond strength is a bit higher in the terrace-adsorbed dimer (row 8), $2 \times (0.91 - 0.31) = 1.20$ eV, where the factor 2 accounts for the fact that a dimer only contains half an intermolecular bond

/NDCA. Nevertheless, a comparison of rows 3 and 8 of Table 6.1 shows clearly that the formation of 1D chains is more favorable than the formation of open-ended dimers.

Adsorbed 1D chains containing species B could not be modeled due to the large size of the adsorbate/substrate unit cell. Instead a gas phase net containing both species A and B in the absence of the Ag support was optimized (Fig. 6.2(b) and row 14 in Table 6.1). The resulting single molecule geometries were further optimized in the presence of the Ag(110) substrate and turned out to be equally stable. Thus, the observed 2/3 : 1/3 ratio of species A and B results from intermolecular interactions (in particular along [-110]) with a small energetic advantage for species A.

The most stable geometry of an NDCA-dimer at an Ag step edge found here is characterized by an intact intermolecular hydrogen bond, cf. Fig. 6.2(c) and row 9 of Table 6.1. A breaking of the hydrogen bond reduces the binding energy by nearly 0.4 eV/NDCA (Fig. 6.2(d), row 10). Thus theory, as experiment, invokes a notion of the lower terrace adsorbates bending up at the step edges to form head-to-tail hydrogen bonds to upper terrace adsorbates. The slight bend of these molecules leads to a minor energy loss, which can be assessed from a calculation of the energy variation with molecule bending (not shown), and which is less than 0.1 eV/NDCA. It is overcompensated by the energy gain from hydrogen-bonding formation across the step. Nevertheless, in line with the experimental results it is also found that the Ag step edge partially prohibits the formation of the ideal NDCA-NDCA bond. This is seen from the strengths of the hydrogen bonds at the step edges, which can be estimated to lie in between $2 \times (0.77 - 0.31) = 0.92$ eV and $2 \times (0.77 - 0.40) = 0.74$ eV. Here the reference point is either an isolated NDCA adsorbed on a terrace (row 1) or a dimer without hydrogen bond at a step edge (row 10). This value is clearly smaller than the 1.20 eV reported above for the terrace NDCA-NDCA bond.

DFT gives large binding energies for deprotonated and covalently bonded molecules at an Ag step edge [216], cf. Fig. 6.2(e, f), rows 12-13 in Table 6.1. However, a separation of the molecules parallel to the step edge (Fig. 6.2(f)) is preferred over a continuation of a 1D chain over the step (Fig. 2(e)). Thus for covalently bonded 1D chains one would expect randomly distributed 1D chains which end at the step edges, at variance with the experimental finding of unbroken 1D chains across the steps. Hence our assumption that all adsorbates are fully protonated and purely non-covalently bonded is confirmed.

6.3 Conclusion

Thus, we have shown that even on defect-afflicted surfaces self-assembly by hydrogen bonding can be used to build 1D mesoscale structures from single molecular building blocks. The theoretical analysis shows that the primary key factor is a robust hydrogen bond. But self-assembly across step edges also depends crucially on the directionality mediated by the substrate, since the 1D chains would not cross the step edges if there existed adsorbate geometries rotated away from the close-packed rows with energies not much smaller than those of the most stable terrace geometries. Also the energy loss inflicted by the bending of the molecules at the step edges is smaller than that for the alternative geometry of open 1D chain ends. Thus, the flexibility of the molecular structure is an additional important ingredient needed for achieving the observed monatomic step tolerance.

CHAPTER 7

Iridium(III) phosphorescent emitter on partly oxidized Cu(110)

The phosphorescent emitters used in organic light emitting diodes (OLEDs) play a crucial role for tuning the color and the luminescence intensity. We have investigated by STM the adsorption of iridium(III) phosphorescent emitter molecules used in OLEDs on a partly oxidized Cu(110) surface. Surprisingly we find that 50% of the emitters have dissociated upon adsorption at the substrate. The findings suggest that the decrease in the lifetime of OLEDs, which are manufactured by vacuum vaporization technique, is due to the dissociation of emitter molecules present in the device.

7.1 Introduction

With their high brightness and availability of a wide range of emission colors, organic light emitting diodes (OLEDs) represent a promising solution for lighting applications as well as for low-cost, full-color flat-panel displays on arbitrary substrates [217,218]. OLEDs consist of one or more semiconducting organic thin films sandwiched between conduction electrodes. The operating principle of such a device is based on the recombination of electrically injected carriers within phosphorescent emitters to generate light. As such, the phosphorescent emitter, in which the recombination actually takes place, plays a key role for tuning the color and the luminescence intensity. In small molecule devices, separate electron and hole transport layers (ETL and HTL) are inserted on either side of this recombination zone to further confine carriers and excitons to a thin region near the interfaces of the HTL and ETL [219-221]. As a result the recombination process is strongly affected by the structure and electronic properties of this interface [222,223]. In order to improve OLED device characteristics, a deeper understanding at the molecular level of the processes occurring at this interface is needed [224]. Scanning tunneling microscopy (STM) is the technique of choice to probe the electronic and transport properties of organic molecules at the molecular level [225]. Some STM studies on organic compounds present in OLED devices have been performed previously [225-227], but a detailed understanding of the crucial triplet emitter is still lacking. Here we report STM studies of the triplet emitter [Ir(2-phenylpyridine)₂(acetylacetonate)] molecules after *in situ* deposition under clean ultrahigh vacuum (UHV) conditions onto a solid surface.

7.2 Results and discussion

Iridium(III) complexes containing 2-phenylpyridine and acetylacetonate ligands [Ir(ppy)₂(acac)] (hereafter labeled as N842) are known to exhibit high triplet quantum yields and are representative for the phosphorescent molecules used in the emitting layer in OLEDs [228]. This complex, shown in Fig. 7.1a, was thermally sublimated under UHV conditions from a molecular evaporator onto a partly oxidized Cu(110) surface held at room temperature. The evaporation temperature was 412 K, far below the decomposition temperature of ~523 K. These conditions yield a coverage in the submonolayer range to facilitate imaging of individual molecules. The partly oxidized Cu(110) surface is created by exposing a clean Cu(110) surface to 4–6 L (1 L=10⁻⁶ Torr) of O₂ at 625 K [229]. This procedure leads to a self-organized reconstruction with alternating clean Cu rows and (2×1)-O reconstructed regions consisting of Cu–O added rows, both aligned along the (001) surface direction, as shown in Fig. 7.1b. A ball model of this nanopatterned surface is shown in Fig. 7.1c. This substrate was chosen as it is relatively easy to obtain atomic resolution on the Cu–O added rows, while simultaneously imaging the deposited molecules. As such it becomes possible to determine the registry of the molecules with respect to the underlying atomic lattice.

Figure 7.2a shows a typical high-resolution STM image obtained after deposition of N842 complexes on a partly oxidized Cu(110) surface. The individual bright spots visible are associated with the individual N842 complexes deposited onto the substrate. It is found that the N842 complexes adsorb almost exclusively on the bare Cu regions in between the Cu–O areas. Previous studies [23,24] of large organic molecules on solid

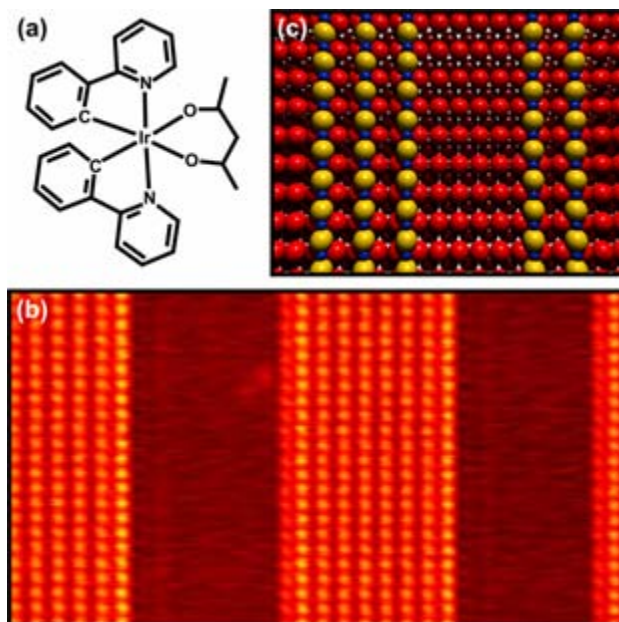


Figure 7.1: (a) Molecular structure of the iridium(III) complexes. (b) $151 \times 82 \text{ \AA}^2$ STM image of the Cu–O/Cu nanopatterned surface used. Images are rotated such that the (001) direction is vertical. 2×1 reconstructed oxidized areas can clearly be distinguished, separated by bare Cu stripes running along the (001) direction ($I_t = 1.13 \text{ nA}$; $V_t = 112.9 \text{ mV}$). (c) A corresponding ball model of the surface shown in (b). In the ball model the yellow atoms represent the added rows of Cu on top of the underlying Cu(110) lattice. The added rows of Cu have an O atom between them represented by the small blue spheres.

surfaces indicate that the main interaction between the molecule and the substrate is most likely van der Waals attractive interaction between the phenyl groups and the metallic surface. As such the binding on the bare Cu stripes is much stronger as the oxygen partly withdraws the charge density of the underlying metal.

From Fig. 7.2a it is apparent that two distinct protrusions, labeled A and B, are observed, with a clear difference in apparent height. A statistical analysis of a number of large scale STM images with a total of 491 protrusions resulted in a distribution of: $47 \pm 2\%$ protrusion A, $47 \pm 2\%$ protrusions B while $6 \pm 1\%$ of the protrusions could not be uniquely assigned. The resulting histogram of the observed objects shows two clearly distinct peaks at 4.4 \AA and 1.8 \AA corresponding to the apparent height of protrusions A and B, respectively (see Fig. 7.2b). The observed size and height for protrusion A corresponds well with the dimensions of the intact N842 complex. However, the observed height for B is typical for atomic adsorbates or flat-lying aromatic compounds, but is too low for the molecule under investigation here [230]. This observation suggests that 50% of the N842 complexes have dissociated upon adsorption at a Cu(110) surface. Pyrolytic dissociation during the evaporation step can be excluded as the decomposition temperature of $\sim 523 \text{ K}$ far exceeds the evaporation temperature of 412 K . Tip induced dissociation can be ruled out as well since no dissociation events have been observed upon repeated scanning of the same surface area. This indicates that the dissociation of the N842 complexes takes place on the substrate. One would therefore expect to observe

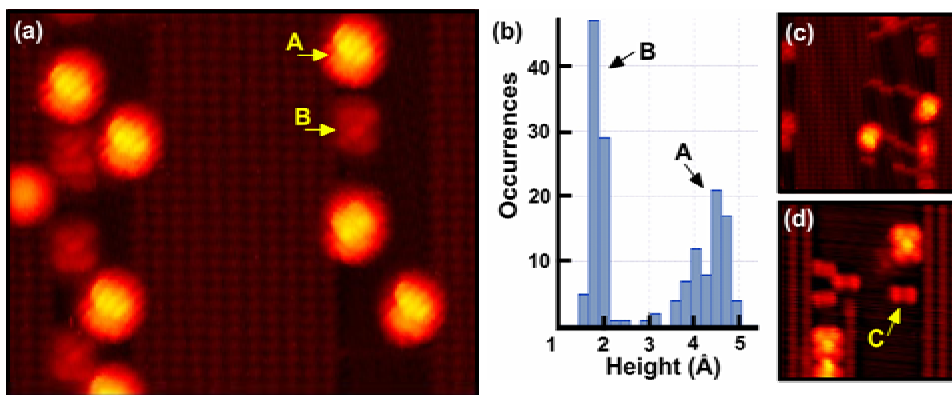


Figure 7.2: (a) Typical $127 \times 104 \text{ \AA}^2$ STM image after vacuum deposition of N842 complexes on a partly oxidized Cu(110) surface. Adsorption of molecules occurs almost exclusively on the bare Cu rows. We observe two clearly distinct protrusions (labeled A and B) with different apparent heights. ($I_t = -0.8 \text{ nA}$; $V_t = -1250 \text{ mV}$) (b) A histogram of the height distribution reveals that A and B have a apparent heights of 1.8 \AA and 4.4 \AA , respectively. (c) $120 \times 120 \text{ \AA}^2$ STM image obtained at 160 K with mobile species present ($I_t = -1.18 \text{ nA}$; $V_t = -1096 \text{ mV}$). (d) $58 \times 58 \text{ \AA}^2$ image obtained at 110 K ($I_t = -0.82 \text{ nA}$; $V_t = -1250 \text{ mV}$). Features corresponding to isolated ligands are clearly visible at 110 K , as indicated by C.

the dissociated ligands on the substrate as well. Closer examination of the selected STM images presented so far indeed shows the presence of smaller objects as well, but those features are mobile even at a sample temperature of 160 K , as shown in Fig. 7.2c. Repeating the measurements at 110 K allows us to directly resolve these additional features, labeled C, as shown in Fig. 7.2d. The shape and size of these features indeed agree very well with those expected for an isolated ligand, which gives an additional confirmation for the dissociation of the N842 complexes on the Cu(110) surface.

A similar observation of the dissociation of a related class of chromium containing organometallic complexes upon adsorption on Cu(100) was reported by Grillo et al., although in their case all molecules had dissociated upon adsorption [231]. Constant-current image calculations, using the electron-scattering quantum chemistry method, for the chromium containing complex show excellent agreement with our experimentally observed features and heights (see Fig. 3 of Ref. [231]). As the geometrical structure of the chromium containing complex is closely related to the N842 complex, this provides additional evidence that in our case protrusion A corresponds to the intact N842 complex, while protrusion B corresponds to a N842 with one of the acetylacetonate ligands missing.

The direct observation of dissociated N842 complexes is surprising for two reasons. Firstly, iridium is a 5d metal making the organometallic complex inherently more stable than a 3d metal complex such as the chromium containing complex. Secondly, the three ligands used in the chromium complex studied in Ref. [231] are phenyl substituted acetylacetonate, which are less electron donating and hence inherently less stable. In our case we have used only one acetylacetonate (without phenyl groups) in combination with 2-phenylpyridine ligands, which contain donor-acceptor properties, thereby making the complex more stable. For these two reasons the iridium containing complexes are considered highly robust. That these complexes are indeed more stable than the chromium complexes is confirmed by the observation that 50% of the molecules on the

substrate are still intact, while all chromium containing complexes had dissociated upon adsorption [231]. The exact mechanism of dissociation is not yet clear, however, the observed ratio of 50/50 between the intact and dissociated molecules suggests that the adsorption geometry of the molecule on the surface plays a crucial role. For large organic molecules it is highly favorable for the molecule to adsorb with phenyl rings lying flat on the metal surface. Due to its geometrical shape, the molecule has a 50% chance to land on the surface with the acetylacetonate ligand either pointing up or down. If it points up it remains intact, however, if this specific group points downwards it is to be expected that the molecule gains enough energy by bringing the phenyl groups closer to the surface so that it is energetically favorable to break the bonds to the ligand.

7.3 Conclusion

In summary, we have characterized the adsorption of iridium(III) phosphorescent emitter molecules on a partly oxidized Cu(110) surface. In doing so we provide convincing evidence that 50% of the emitters have dissociated upon adsorption at the substrate. Our findings suggest that the decrease in the lifetime of OLEDs, which are manufactured by vacuum vaporization technique, is due to the dissociation of emitter molecules present in the device. Therefore, to enhance the lifetime of OLEDs, careful design and development of more robust phosphorescent complexes are required. The work towards this goal is in progress.

CHAPTER 8

H on HOPG

Structures and kinetics of H monomers, dimers, and trimers on HOPG will be detailed in the following sub-chapters. First, we present STM results which reveal the existence of two distinct hydrogen dimer states on graphite basal planes. DFT calculations allow us to identify the atomic structure of these states and to determine their recombination and desorption pathways. Direct recombination is only possible from one of the two dimer states. This results in increased stability of one dimer species and explains the puzzling double peak structure observed in temperature programmed desorption spectra for hydrogen on graphite. Secondly, we present STM experiments and DFT calculations which reveal a unique mechanism for the formation of hydrogen adsorbate clusters on graphite surfaces. Our results show that diffusion of hydrogen atoms is largely inactive and that clustering is a consequence of preferential sticking into specific adsorbate structures. These surprising findings are caused by reduced or even vanishing adsorption barriers for hydrogen in the vicinity of already adsorbed H atoms on the surface and point to a possible novel route to interstellar H₂ formation. Thirdly, we present STM images of meta-stable hydrogen adsorbate structures on the HOPG (0001) surface and identify two unique and stable hydrogen structures. One of these is observed after thermal anneals to 525 K at both high and low hydrogen coverage and is identified as a hydrogen dimer structure. The other, a novel, more complex structure not previously observed, appears only after thermal anneals at high hydrogen coverage and is observed to exhibit long range orientation within each micro-crystallite region on the HOPG surface.

8.1 H dimer on graphite(0001) surface

8.1.1 Introduction

The interaction between molecular and atomic hydrogen and graphite surfaces has attracted considerable interest in recent years. The possibility of using carbon nanostructures as a storage medium for hydrogen has been extensively investigated [232], and it has been suggested that hydrogen atoms stored in the chemisorbed state of graphite might be an energy source for future space applications due to the high energy release in molecular hydrogen formation from atomic recombination on this surface [233]. In the area of interstellar chemistry, hydrogen on graphite is considered to be a key model system. In spite of continuous destruction by UV radiation and cosmic rays, H_2 is the most abundant molecule in the interstellar medium (ISM).

However, no efficient gas-phase route exists for H_2 formation at the low H-atom densities of the ISM. Thus, efficient formation of H_2 in interstellar dust and molecular clouds is believed to proceed via atomic recombination of hydrogen atoms adsorbed on interstellar dust grain surfaces. Recent experiments have shown that such processes are indeed possible under conditions resembling those found in dense and cold (10–20 K) diffuse interstellar clouds [234–236]. However, the mechanisms suggested by these experiments are all based on recombination of physisorbed atomic hydrogen and are efficient only in a small temperature interval [234]. Hence, they cannot explain efficient formation under conditions found in warmer environments such as photo dissociation regions (PDRs), where more tightly bound, chemisorbed, states of adsorbed hydrogen atoms have to be invoked [237]. Since carbonaceous grains are believed to be abundant in the ISM, particular attention has been focused on atomic recombination of hydrogen adsorbed in chemisorbed states on graphite surfaces [237].

The chemisorbed state of atomic hydrogen on graphite was initially observed using ultraviolet photon spectroscopy [238], and its characteristics were predicted by density functional theory calculations. The calculations show that hydrogen binds with a binding energy of ~ 0.7 eV at an on-top site, causing a reconstruction of the graphite surface in which the C atom below the H atom puckers out of the surface by 0.35\AA [239,240]. Because of this puckering there is a barrier to enter into the chemisorption state of about 0.2 eV [239,240]. Atomic recombination to molecular hydrogen from chemisorbed atomic hydrogen on graphite has been observed in temperature programmed desorption (TPD) measurements [241] and via Eley-Rideal processes [242]. The TPD spectra are 1st order suggesting that the H atoms might be paired on the surface prior to desorption or that the rate limiting step in the recombination process involves only one H atom. Also, the spectra exhibit a double peak structure indicative of multiple adsorption sites and desorption pathways. In spite of increased theoretical activity aimed at determining the mobility of hydrogen atoms [241,242] and the binding energy of hydrogen dimer states [243,244] on graphite, the recombination pathways for hydrogen atom adsorbates on graphite surfaces are still undetermined.

Here we show STM experiments combined with DFT calculations, which clarify both the structures and kinetic recombination pathways of different hydrogen dimer states on HOPG. At low coverage, recombination is seen to take place out of only one hydrogen adsorbate dimer state, in which hydrogen atoms are adsorbed on carbon atoms on opposite sides of the carbon hexagon. All other states, including the nearest neighbor

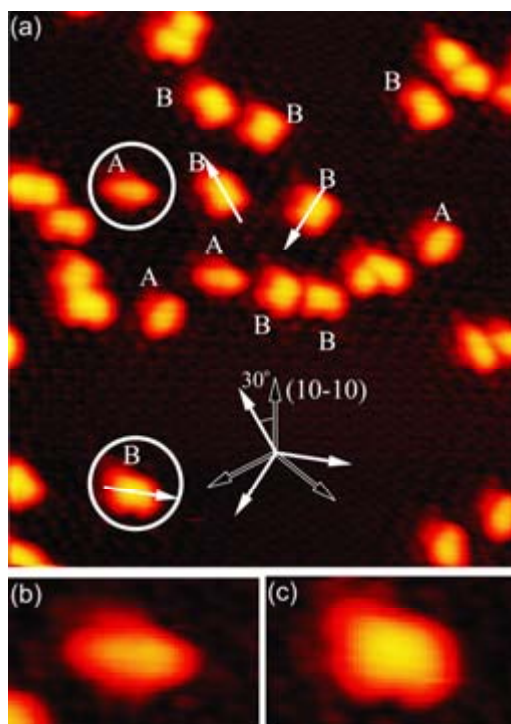


Figure 8.1: (a) STM image ($103 \times 114 \text{ \AA}^2$) of dimer structures of hydrogen atoms on the graphite surface after a 1 min deposition at room temperature. Imaging parameters: $V_t = -884 \text{ mV}$, $I_t = -160 \text{ pA}$. Examples of dimer type A and B are marked. Black arrows indicate the $[2-1-10]$ directions and white arrows indicate the orientation of the dimers 30° off. (b) Close up of dimer A structure in top white circle in image (a). (c) Close up of dimer B structure in lower white circle in image (a).

dimer state, are observed to recombine via diffusion over this state. These results explain the structure observed in TPD spectra of molecular hydrogen desorption from graphite.

8.1.2 Results and discussion

Figure 8.1(a) shows an STM image of the graphite surface after a 1 min dose of D atoms at 2200 K onto a room temperature HOPG sample. A number of bright protrusions are observed in the image (the coverage is approximately 1%), which we identify as clusters of chemisorbed deuterium atoms, as they only appear after D dosing. As discussed below, their presence correlates with the D_2 desorption peaks observed in the TPD spectra. The deuterium atoms are not observed to diffuse at room temperature. In between the bright protrusions, the graphite lattice is observed. Associated to each bright D atom correlated protrusion, we find a wavelike electronic perturbation of the graphite lattice, which vanishes for distances larger than about 35 \AA . This is in good agreement with previous results for H implanted on HOPG by hydrogen plasma treatment [245]. In accordance with earlier observations, no well-ordered superstructure of the adsorbed deuterium atoms is observed. Two different characteristic structures, labeled dimer A

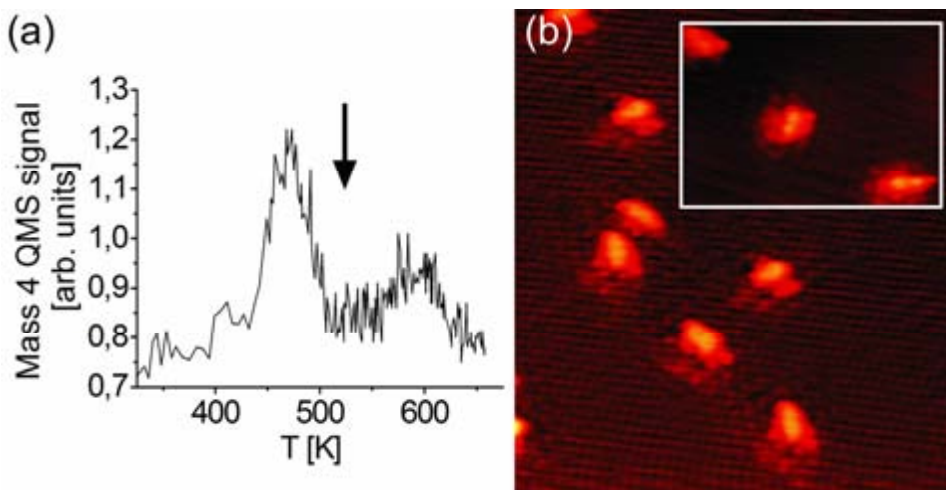


Figure 8.2: (a) A mass 4 amu, i.e., D₂, TPD spectrum from the HOPG surface after a 2 min D atom dose (ramp rate: 2 K/s below 450 K, 1 K/s above). The arrow indicates the maximum temperature of the thermal anneal performed before recording the STM image in (b) STM image (103 × 114 Å²) of dimer structures of hydrogen atoms on the graphite surface after a 1 min deposition at room temperature and subsequent anneal to 525 K (ramp rate: 1 K/s, 30 s dwell at maximum temperature). Imaging parameters: V_t = -884 mV, I_t = -190 pA. The inset shows a higher resolution STM image of dimer structures of hydrogen atoms on the graphite surface after a 6 min deposition at room temperature and subsequent anneal to 550 K. Imaging parameters: V_t = -884 mV, I_t = -210 pA.

and dimer B, are observed to be dominant, with the dimer B structure as the most numerous. Figs. 8.1(b) and (c) show close-ups of these two structures. Dimer A are slim elongated spheroids, while dimer B structures are more rectangular in shape. The long axis of both dimer A and dimer B structures is oriented along directions offset 30° with respect to the <2-1-10> directions. This results in three possible orientations separated 120° with respect to each other. A few larger, composite structures are also observed.

Figure 8.2(a) shows a D₂ TPD spectrum from the HOPG surface after a 2 min D atom dose. The spectrum shows the double peak structure discussed in the introduction. In order to investigate if the peaks correspond to different hydrogen adsorbate structures, we performed a thermal anneal to a temperature between the two peaks. The arrow indicates the maximum temperature (525 K) of the thermal anneal performed before recording the STM image shown in Fig. 8.2(b). After the 525 K anneal, the sample is cooled to room temperature before being placed in the STM. We find a significant decrease in the total coverage on the annealed sample, and now only dimer A structures are observed. Repeated experiments showed that annealing to temperatures of 500–600 K starting from a low coverage of D atoms leads to a surface where dimer A is the dominant structure. Hence, the experiment indicates that dimer A structures are stable against thermal annealing to 525 K, whereas dimer B structures are not. Since no D atoms are visible on the surface after anneals to 600 K, i.e., above the high temperature peak in the TPD spectrum, the interpretation is that dimer B structures contribute to the first peak in the desorption spectra while dimer A structures are associated with the second peak. Based on the Polanyi-Wigner equation for first order desorption and assuming a preexponential factor of 10¹³ s⁻¹, the two peaks at 490 K and 580 K observed

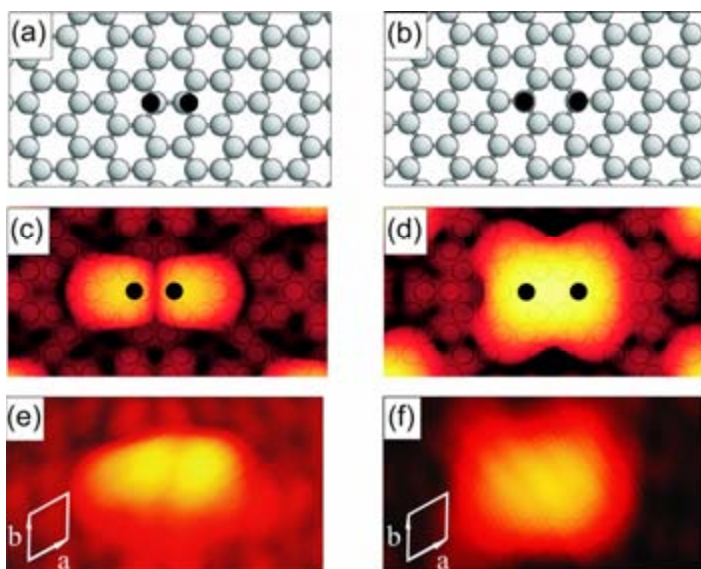


Figure 8.3: Calculated structure of the two most tightly bound dimer structures of hydrogen atoms on the graphite surface. (a) Dimer A structure of hydrogen atoms adsorbed on neighbor carbon atoms. (b) Dimer B structures of hydrogen adsorbed on carbon atoms at opposite sides of the graphite hexagon. (c) Simulated STM image of the dimer structure in (a). (d) Simulated STM image of the dimer structure in (b). Imaging parameters: $V_t = -0.9$ V, $\rho_0 = 1 \times 10^{-6}$ (eV) $^{-1}$ \AA^{-3} . The position of the hydrogen atoms is marked by black dots. (e) Experimental dimer A structure. (f) Experimental dimer B structure. The carbon unit cell is marked in white.

in TPD spectra for deuterium on graphite correspond to desorption barriers of 1.38 eV and 1.64 eV, respectively.

Density functional theory calculations of the lowest energy states of H dimers on a graphite surface show two states with an approximately identical binding energy of 2.51 eV with respect to the energy of the undisturbed carbon surface and 2 H atoms at infinite separation. Referring to two isolated adsorbed H atoms the binding energy is 1.18 eV. The two states are shown in Figs. 8.3(a) and (b). The two hydrogen atoms are adsorbed either on two neighbor carbon atoms or on carbon atoms at opposite sides of a carbon hexagon. Based on the structure and stability findings given below we assign the state shown in Fig. 8.3(a) to the experimentally observed dimer A and the state in Fig. 8.3(b) to the experimental dimer B state. The calculated binding energy of the dimer A state is in good agreement with earlier calculations [243,244]. However, the binding energy of the dimer B state differs from that reported in Miura et al. [244]. This difference can be ascribed to the fact that a smaller carbon unit cell was used in the previous calculations [244]. Figs. 8.3(c) and (d) show simulated STM images of the two dimer structures. In both cases the dimers and the long axis of the dimer structures in the simulated images are oriented at 30° with respect to the $\langle 2-1-10 \rangle$ directions, like the experimentally observed dimer structures. The dimer structure shown in Fig. 8.3(c) is an elongated spheroid with a thin dark central line structure along the minor axis. The simulated image is very reminiscent of the dimer A structure in the experimental images. However, due to tip smoothing effects the thin dark central line is only imaged in STM under very favorable imaging conditions as in the inset in Fig. 8.2(b) and in Fig. 8.3(e). The dimer

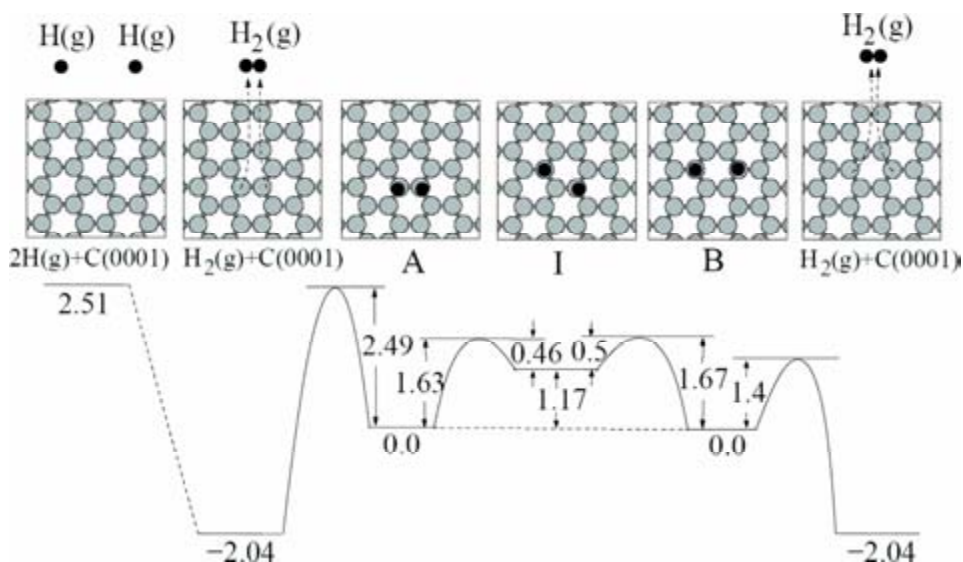


Figure 8.4: Energy barriers for atomic hydrogen diffusion and recombination from dimer A and B states on the graphite surface. The barrier to desorption of a single H atom out of structures A, I, and B are 2.08, 0.92, and 1.92 eV, respectively, and is hence energetically unfavorable in all three cases.

structure in Fig. 8.3(d) on the other hand is more rectangular in shape and resembles the dimer B structures observed in the STM images.

Since each dimer corresponds to a different peak in the TPD spectra, dimer A must be more stable than dimer B. Clearly, this difference in stability cannot be explained by binding energy considerations. Instead, the detailed kinetics of the desorption processes has to be considered and the recombination pathways for each of the two dimer states identified. Figure 8.4 shows the calculated binding energies, diffusion barriers and recombination barriers for 2 H atoms on the graphite surface. Based on the calculations, it becomes clear that recombination will take place out of the dimer B state with a barrier of 1.4 eV, in reasonable agreement with the barrier derived from the first peak in the TPD spectra. Direct recombination from the dimer A state into molecular hydrogen is prevented by a rather large energy barrier, similar to the energy cost to desorb both H atoms separately. A facile pathway for recombination of hydrogen atoms in the dimer A state can, however, be found, corresponding to diffusion over state I into state B and then direct recombination from B. The rate limiting step in this process is diffusion from state A to state I. The diffusion barrier is 1.6 eV, which is in excellent agreement with the barrier to desorption derived for the 2nd peak in the TPD spectra. Hence, direct recombination of dimers in a dimer B structure contribute to the low temperature peak in TPD, while diffusion mediated recombination from the dimer A state over the dimer B state contributes to the high temperature peak.

It has previously been suggested that recombination might occur via a physisorption state of H on graphite [246]. This suggestion was based on TPD experiments performed after H/D atom deposition at 150 K. Since the TPD spectra look identical for H/D atom deposition at 150 and 300 K [233] we expect recombination to proceed via the same pathway in the experiments reported on in [241,246] and the experiments reported on

here. A weak physisorption state of H on graphite has been observed experimentally in scattering experiments [247] and theoretically in DFT calculations [239,240]. The binding energy of this state is of the order of a few tens of meV. Hence, recombination of two chemisorbed H atoms via this state would require that a hydrogen atom desorbs from the strongly bound chemisorbed state involving severe surface reconstruction and is readsorbed in a very shallow (10–40 meV) physisorption well. Such a process does not seem likely. The self-consistent model presented here offers an alternative explanation for recombination of atomic hydrogen on graphite surfaces that does not invoke recombination via a weakly bound physisorbed state.

8.1.3 Conclusion

In conclusion, based on STM experiments and DFT calculations we have identified the recombination mechanisms of H atoms on the graphite surface and shown that direct recombination takes place out of only one of the two observed dimer states. The presented results explain the structure observed in TPD spectra of molecular hydrogen desorption from graphite. Furthermore, the determined recombination mechanism and diffusion and recombination barriers provide direct input to models of interstellar hydrogen formation on graphitic interstellar dust grain surfaces.

8.2 Clustering of H atoms on graphite(0001) surface

8.2.1 Introduction

Hydrogen adsorption and the structure of hydrogen adsorbates on surfaces have been studied extensively due to both its fundamental interest and its relevance in connection with numerous technological applications. Preparing and clustering of hydrogen atoms on surfaces have been reported for systems such as H on Si [248] and H on diamond C(111) [249]. For these systems the preparing mechanism is thought to be thermal or “hot precursor” mediated diffusion [249,250]. Here we report on a mechanism for H atom cluster formation on graphite surfaces which does not involve diffusion. The presented results have interesting implications for interstellar H₂ formation in photon dominated regions and in shocked interstellar gases.

Molecular hydrogen is the most abundant molecule in the interstellar medium featuring both in dense and diffuse interstellar molecular clouds, in photon dominated regions (PDRs) [251], and in regions with shocked gasses [252]. In all these regions molecular hydrogen is continuously dissociated by UV radiation and/or cosmic rays. To maintain the abundance of molecular hydrogen, an efficient formation mechanism is required. This mechanism is generally accepted to be H₂ formation on the surface of interstellar dust grains [253]. A substantial fraction of interstellar dust grains are anticipated to be carbonaceous, and onionlike graphite particles have been observed both in presolar dust grains in meteorites [254] and in experiments simulating interstellar grain formation [254,255]. The details of the H₂ formation process have been shown to significantly impact the thermal and chemical evolution in the interstellar medium [251,252,256-258]. It was previously perceived that the large barrier for chemisorption (~0.2 eV) [239,240] would make it unrealistic to obtain a sufficient coverage of H atoms on graphitic surfaces under interstellar conditions. The results presented here challenge this perception by identifying a new mechanism for the formation of H adsorbate clusters. Previous investigations have shown that molecular hydrogen can form on graphite [241] from such H clusters along two paths: either (i) from prepared H dimers on the surface [233,260] or (ii) via Eley-Rideal abstraction reactions [242,261] between adsorbed H atoms and incoming H atoms from the gas phase. In both cases, the identified mechanism for hydrogen cluster formation on graphitic surfaces provides a route for interstellar H₂ formation.

8.2.2 Results and discussion

Figure 8.5(a) shows an STM image of a 210 K graphite (HOPG) surface exposed to a very low dose of hot D atoms. The bright protrusions in the image are ascribed to chemisorbed D atoms since they only appear after D atom dosing and are correlated with molecular deuterium desorption. A close-up of one of these bright protrusions is shown in Fig. 8.6(a). The threefold symmetry of the structure is as expected for a D monomer adsorbed above a C atom on the graphite surface. By associating each bright protrusion with 1 D atom, a D monomer, we calculate a D atom coverage of 0.03%. After recording STM images like the one in Fig. 8.5(a), the HOPG sample was removed from the STM and heated to room temperature for 10 min before being put back into the cooled STM. The resulting STM image is shown in Fig. 8.5(b). As can be seen, the number of bright

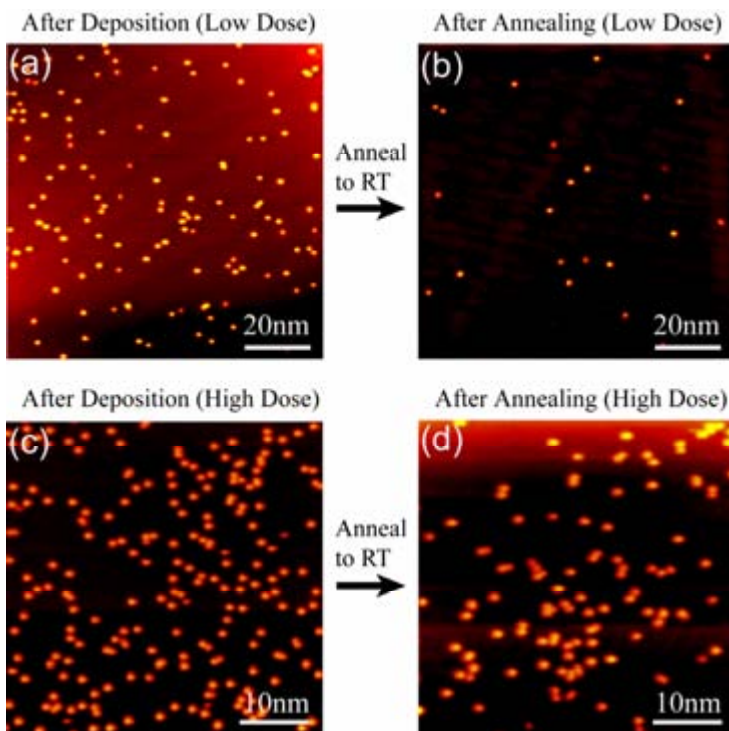


Figure 8.5: STM images of the graphite surface after D atom deposition. During deposition and in the STM the sample temperature is kept below 210 K. (a) STM image after deposition at low integrated flux ($F \sim 10^{12}$ atoms/cm² s). (b) STM image after heating the sample in (a) to room temperature (RT) for 10 min followed by recoiling in the STM. (c) STM image after D atom deposition at high integrated flux ($F \sim 10^{14}$ atoms/cm² s). (d) STM image after heating the sample in (c) to RT for 10 min followed by recoiling in the STM. Imaging parameters: (a) $I_t = -0.58$ nA, $V_t = -312$ mV, (b) $I_t = -0.45$ nA, $V_t = -1250$ mV, (c) $I_t = -0.43$ nA, $V_t = -1250$ mV, (d) $I_t = -0.26$ nA, $V_t = -1486$ mV.

protrusions is drastically reduced by 80%. By assuming that all the bright protrusions in Fig. 8.5(a) are D monomers, an upper limit on the lifetime of isolated D atoms on the graphite surface of 6 min can be obtained. This value is in good agreement with the one expected for hydrogen monomer desorption based on the theoretically derived desorption barrier of 0.9 eV [239,240].

Figure 8.5(c) shows an STM image after a D atom dose roughly a hundred times higher than in Fig. 8.5(a). Again we ascribe the bright protrusions to chemisorbed D atoms. A close-up on these bright protrusions show that the majority are more complex structures, similar to the ones shown in Fig. 8.6(b), which we associate with D atom clusters. We calculate the coverage of $0.2\% \times (\text{number of atoms per protrusion})$. Fig. 8.5(d) shows an STM image obtained after removing the sample from the STM, heating it to room temperature for 10 min. and then placing it back into the cooled STM. In this case a less drastic reduction of only 20% in the number of bright protrusions is observed. This finding indicates that at the higher integrated flux more stable adsorption complexes are formed on the surface. Based on the upper limit on the D monomer lifetime derived above, a lower limit on the percentage of more stable adsorption complexes can be

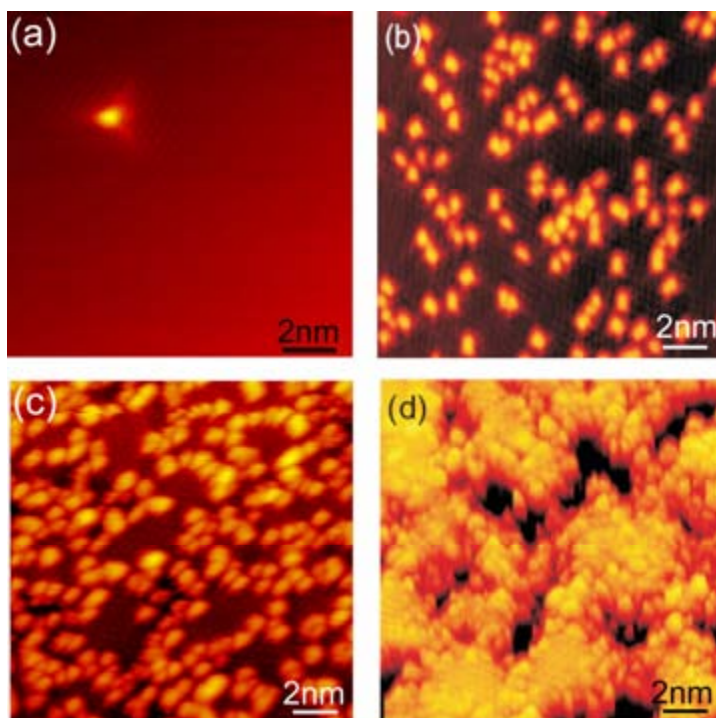


Figure 8.6: STM images of the graphite surface after increasing doses of D atoms showing the formation of increasingly more complex adsorption clusters. (a) Zoom in on one of the bright protrusions in Fig. 8.5(a). (b) STM image showing the formation of hydrogen dimer structures after a 1 min D atom dose at a flux of $F \sim 10^{15}$ atoms/cm² s. (c) STM image showing the formation of larger and more complex adsorption clusters after a 6 min D atom dose at a flux of $F \sim 10^{15}$ atoms/cm² s. (d) STM image showing the graphite surface at saturation coverage after a 24 min D atom dose at a flux of $F \sim 10^{15}$ atoms/cm² s. The underlying carbon lattice is no longer visible and the image is dominated by the electronic reconstruction induced by the hydrogen adsorbates. Imaging parameters: (a) $I_t = -0.71$ nA, $V_t = -156$ mV, (b) $I_t = -0.16$ nA, $V_t = -884$ mV, (c) $I_t = -0.15$ nA, $V_t = -743$ mV, (d) $I_t = -0.53$ nA, $V_t = -1050$ mV.

obtained. We find that at least 75% of the D atom adsorbate structures in Fig. 8.5(c) must be such complexes.

As will become apparent from our calculations it is a fair assumption that stable adsorption complexes consist of D atoms adsorbed within 4th nearest neighbor distance of each other (see discussion below). If the D atoms were distributed uniformly on all carbon surface atoms, then at an adsorbate cluster coverage of 0.2%, as in Fig. 8.5(c), at most 5% of the D atoms should be part of adsorption clusters containing more than 1 D atom adsorbed within 3rd nearest neighbor distance. This finding contradicts the experimental observation that 75% of the D atoms are associated with more stable structures and indicate that some mechanism favors formation of more stable adsorption clusters.

Figures 8.6(a)–(d) show high-resolution STM images of graphite after exposure to increasing doses of D atoms, demonstrating that the tendency to form clusters continues at higher total coverages. Fig. 8.6(a) is a close-up of an adsorption structure on the low

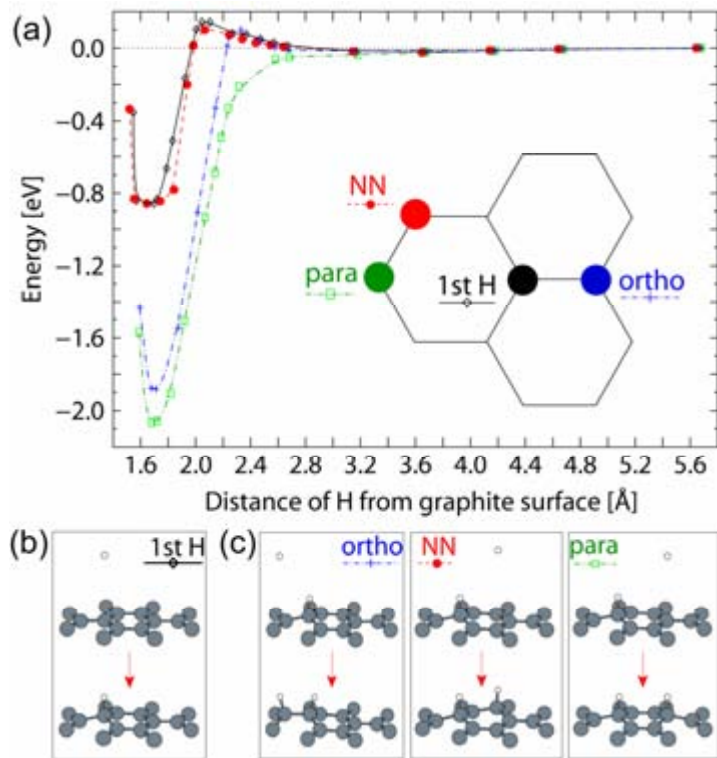


Figure 8.7: (a) Potential energy curves for adsorption of a single H atom monomer (solid line), shown in (b), and for the three dimer configurations shown in (c), the orthodimer (dash-dotted line), the next neighbor site (dashed line), and the paradimer (dash-double dotted line).

coverage surface shown in Fig. 8.5(a). The threefold symmetry of the bright protrusion is as expected for a D monomer adsorbed above a C atom on the graphite surface. Fig. 8.6(b) shows D adsorbate structures at slightly higher cluster coverage of $\sim 1\%$. The elongated bright protrusions, which dominate the image, have been identified as hydrogen (deuterium) dimers [260,262]. At an even higher coverage of $\sim 3\%$ as in Fig. 8.6(c), the majority of the D atoms are adsorbed in larger D atom clusters. Finally, at saturation coverage of $\sim 50\%$ [241], the carbon lattice is no longer visible, and the STM image is completely dominated by the electronic effects caused by the deuterium adsorbates.

To determine whether the observed hydrogen (deuterium) atom clusters could be a result of thermal diffusion, the diffusion barrier for an isolated chemisorbed H atom on the graphite surface was calculated, using first principles DFT calculations. The calculations predict a diffusion barrier of 1.14 eV. Since the desorption barrier is only around 0.9 eV this implies that an isolated H atom will desorb rather than diffuse upon heating. This prediction is in good agreement with the experimental findings. STM observations performed both at room temperature and at temperatures of ~ 200 K show that D atoms are immobile on the graphite surface at all coverages. This finding indicates that the reduction in the number of bright protrusions observed in the STM

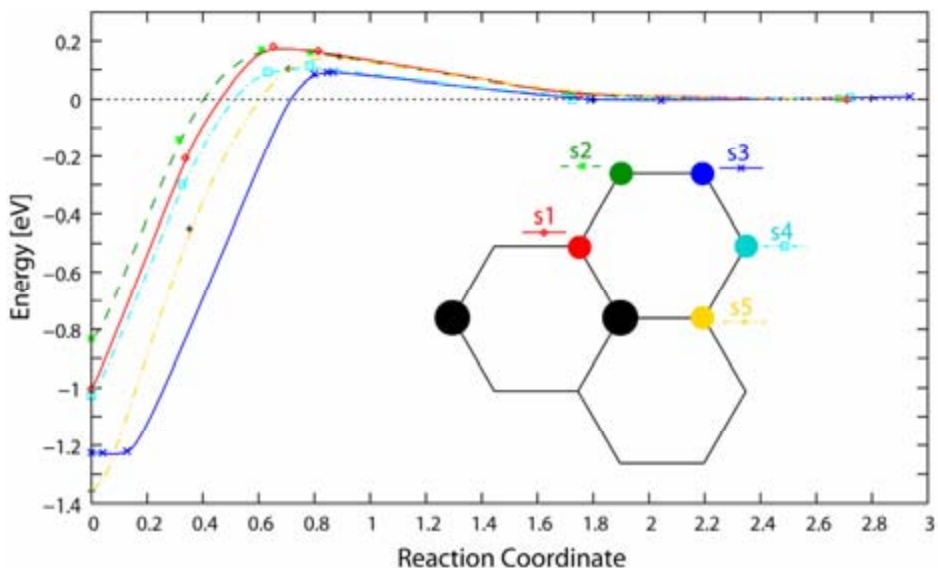


Figure 8.8: Potential energy curves for adsorption of a third H atom in the vicinity of a paradimer at sites s1–s5 shown in the inset. The reaction coordinate is a sum over all position changes of all atoms in the calculation.

images in Fig. 8.5 is due to H atom desorption and that at higher integrated hydrogen atom flux, adsorption complexes which are more stable against desorption are formed.

To investigate under what conditions hydrogen adsorbate clusters can be expected to give rise to increased stability against desorption, the binding energy of various configurations involving 2 H atoms adsorbed within 1st–6th nearest neighbor distances were investigated. Only the ortho- and para-dimer configurations shown in Fig. 8.7(c) show markedly increased binding energies. The next neighbor configuration, NN in Fig. 8.7(c), has been shown elsewhere to convert to either of the two with a barrier of only ~ 0.5 eV [260]. This finding justifies the above use of 4th nearest neighbor as the cutoff distance for increased stability of adsorbate clusters.

Since the observed clustering is not a result of diffusion, the influence of the sticking process on clustering was investigated. Figure 8.7(a) shows the potential energy curves for H atom sticking into the four configurations shown in Fig. 8.7(b) and (c). Two observations stand out: (i) the binding energy of the ortho- and para-dimers is much increased compared to the binding energy of 2 H monomers or the next neighbor (NN) dimer state [263], and (ii) the barrier to adsorption into the ortho-dimer and next neighbor dimer is reduced by roughly 50 meV compared to the sticking of an H atom into a monomer state, while no barrier to adsorption is observed for sticking into the para-dimer configuration [264]. The reduced and even vanishing barriers to hydrogen sticking into specific adsorption sites in the vicinity of already adsorbed H atoms will lead to preferential sticking. This observation implies that cluster configurations will become more abundant. According to these calculations, para-dimer structures should be the dominant structure at low coverage since no barrier exists for sticking into this state. Experimental observations show that this is indeed the case [260].

To investigate whether similar mechanisms control the formation of larger clusters at higher coverage, the potential energy curves for adsorption of a third H atom in the

vicinity of the hydrogen para-dimer were calculated. These are shown in Fig. 8.8. Reduced barriers to sticking are observed for a third H atom adsorbing into sites 3, 4, and 5 (marked in the figure inset). Further calculations with sticking of a fourth atom also reveal the existence of sites with reduced and even vanishing barriers to adsorption. This finding indicates that also larger clusters form as a result of preferential sticking due to reduced barriers to adsorption in the vicinity of already adsorbed H atoms. The existence of reduced barriers to adsorption into several different cluster structures is in good agreement with the experimental observation of more varied and complex adsorption structures at higher coverages.

8.2.3 Conclusion

The identified mechanism for hydrogen cluster formation differs from the preparing and clustering mechanisms reported on for other systems, e.g., H on Si [248] and H on diamond C(111) [249]. For these systems the preparing mechanism is thought to be thermal or “hot precursor” mediated diffusion [249,250]. In contrast, the mechanism presented here does not involve diffusion. Besides being of fundamental interest, the identified mechanism also has interesting implications for interstellar hydrogen formation. In PDRs and post-shock regions gas temperatures range from several hundred to thousand Kelvin [256,257,265], and hydrogen atoms in the high energy tail of the thermal Maxwell-Boltzmann distribution will have sufficient energy to populate the chemisorbed state on graphitic grain surfaces. Once a first hydrogen atom is adsorbed on the surface, the adsorption barriers for additional H atoms are much reduced or even vanishing, and larger clusters can form. This mechanism enables the buildup of non-negligible H atom coverages from which molecular hydrogen formation may occur either via recombinative desorption or via Eley-Rideal abstraction. Hence, the presented results at the same time reveal a new mechanism for adsorbate cluster formation on surfaces via preferential sticking and contribute to our understanding of interstellar hydrogen formation.

8.3 H trimer on graphite(0001) surface

8.3.1 Introduction

Low energy electron diffraction (LEED) experiments show that hydrogen atoms do not adsorb in ordered structures on the graphite surface [268]. Hydrogen dimer structures have been directly observed and identified on low coverage graphite surfaces in STM measurements [260,262]. Since the diffusion barrier for isolated H atoms chemisorbed on the graphite surface is larger than the desorption barrier and since DFT calculations show reduced and in some cases even vanishing atom sticking barriers in the vicinity of already adsorbed H atoms the formation of these dimer structures is believed to occur via preferential sticking directly into dimer configurations [269,270]. Based on the STM studies two dimer structures are inferred to be most abundant on the graphite surface, namely the ortho-dimer structure where two hydrogen atoms are adsorbed on nearest neighbor carbon atoms and the para-dimer structure where two H atoms are adsorbed on opposite sides of a carbon hexagon. The existence of hydrogen quartet structures has also been proposed [271]. Here we present new STM results which reveal that at higher coverage a new, complex, meta-stable hydrogen structure exists which is as stable as the ortho-dimer structure and co-exist with this structure at temperatures up to 600 K.

8.3.2 Results and discussion

Figure 8.9(a) shows an STM image of a HOPG surface after a 12 min D atom deposition. The bright protrusions in the images are ascribed to clusters of chemisorbed D atoms since they only appear after D atom deposition and since they are correlated with molecular deuterium desorption measured in TPD. Fig. 8.9(b) displays an STM image after a 12 min D atom deposition as in Fig. 8.9(a), followed by a thermal anneal to 525 K. Again, the bright protrusions in the images are ascribed to clusters of chemisorbed D atoms. Two different types of structures are visible in the image. One type is elongated ellipsoidal shapes with three different orientations while the other structure has a star like shape. Fig. 8.9(c) displays the statistical analysis of a larger series of STM images obtained by annealing the D covered HOPG surface depicted in Fig. 8.9(a) to subsequently higher temperature. Following 12 min D atom deposition at room temperature the surface was annealed to temperatures ranging from 500 to 570 K and the fraction of elongated ellipsoids and star structures was recorded as a percentage of the total number of D atom clusters on the surface. We find that as the annealing temperature increases, the total coverage decreases and the relative percentage of elongated ellipsoids and star structures is observed to increase until they become completely dominant. This indicates that the elongated ellipsoid and star structures are more stable than other hydrogen adsorbate structures observed on the graphite surface. The star and elongated ellipsoid structures are desorbed at temperatures above 550 K, coinciding with the high temperature D₂ peak observed in TPD experiments from atomic recombination of chemisorbed D atoms on graphite [241].

As discussed above a hydrogen dimer structure (the ortho-dimer) with high stability towards thermal anneals has previously been identified in STM experiments obtained following anneals of graphite surfaces with a lower coverage of D atoms [260]. This ortho-dimer state exhibited the same electronic characteristics and desorption kinetics as

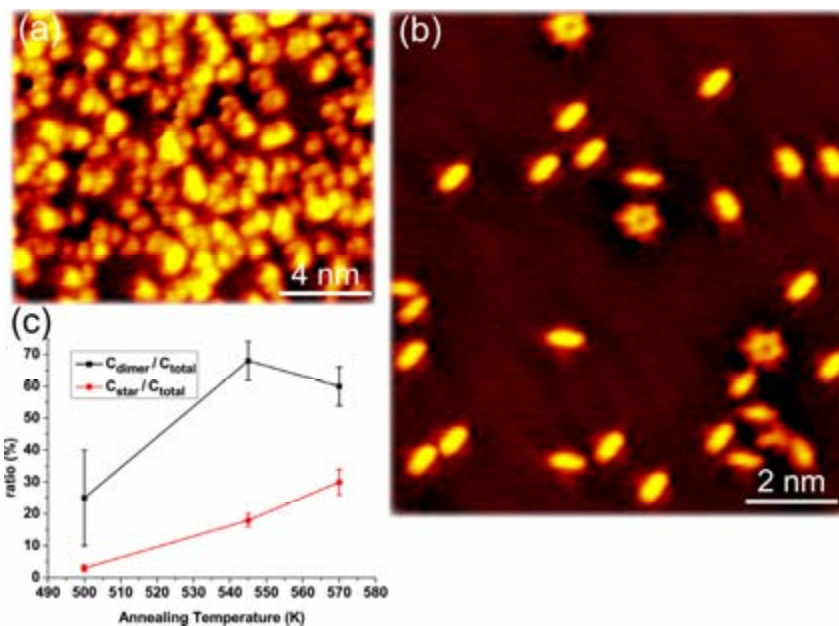


Figure 8.9: (a) STM image of the graphite surface after a 12 min D atom dose. Imaging parameters: $I_t = -0.2$ nA, $V_t = -743$ mV. (b) STM image of the graphite surface obtained after a 12 min D atom dose followed by an anneal to 525 K. Imaging parameters: $I_t = -0.18$ nA, $V_t = -1051$ mV. (c) The relative percentage of star and dimer clusters as a function of annealing temperature. Data were obtained following anneals to 500 K, 545 K and 570 K.

the elongated ellipsoids imaged by STM following anneal of the high-coverage surface displayed in Fig. 8.9(a). We therefore identify the elongated ellipsoids in Fig. 8.9(b) as hydrogen ortho-dimers. The star-like structures in Fig. 8.9(b) have not been observed previously and are only observed following high D exposures.

Figure 8.10 shows a series of STM images of a star like structure like the ones shown in Fig. 8.9(a) recorded at different tunneling voltages. At higher voltages, when the tip is far from the surface, the imaged structure is star like, while at lower voltages, when the tip is close to the surface the structure appears as a triangle.

Figure 8.11(a) shows a high-resolution zoom in on a star like structure. D atoms chemisorbed on the graphite surface give rise to a large perturbation of the local electronic density of states at the adsorption site and also give rise to long range electronic modifications in the form of a $(\sqrt{3} \times \sqrt{3}) R30^\circ$ superlattice at distances as far away as 35\AA from the adsorption site [245,260]. At the edges of the image the undisturbed carbon lattice is observed. STM only images every second carbon atom on the graphite surface and the consensus is that the imaged atoms are carbon atoms in β sites [272], i.e. carbon atoms with no neighbor in the underlying carbon layer vs. atoms that do have a neighbor in the underlying layer. In Fig. 8.11(a) a graphite lattice has been overlaid on top of the high-resolution STM image. The positions of the β carbon atoms are represented by big dots. The star structure in the image is observed to be centered on a β carbon atom. The positions of the α carbon atoms cannot be unequivocally determined based on the STM image, since two possible mirror-images of the graphite lattice exist, with interchanged α carbon atom and hollow site positions, which give rise

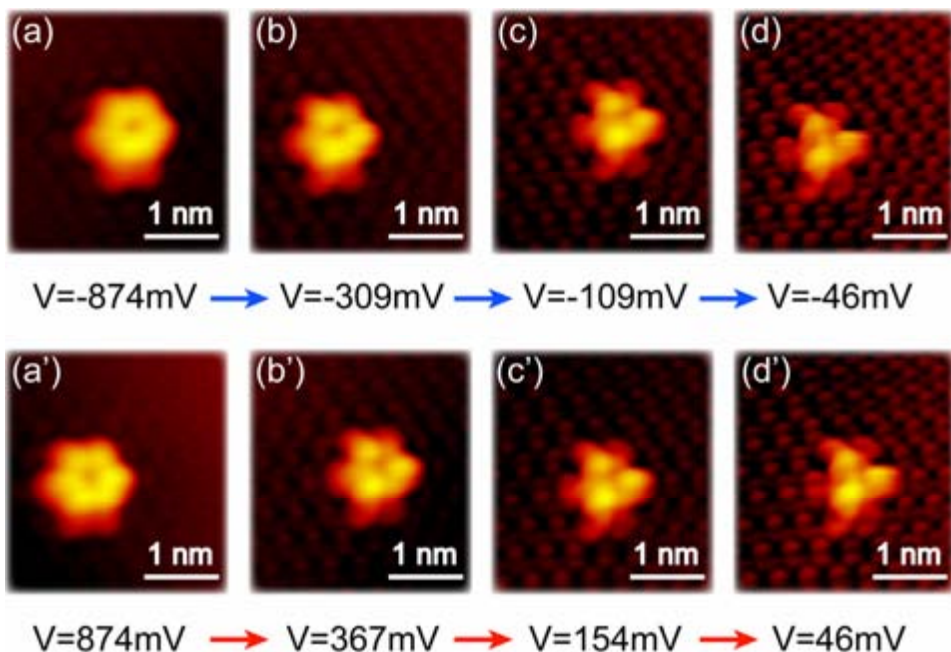


Figure 8.10: Star-structure imaged at varied bias voltage, $I_t = \pm 0.15$ nA. At low bias voltage, i.e. when the STM tip is in close proximity to the surface, the star-structure appears triangular in the STM images.

to the imaged carbon atom structures in Fig. 8.11(a). One of the two possible graphite lattices is superimposed on the image with the small dots representing one of the two possible positions of α carbon atoms. For either of the two possible graphite lattices, three of the bright bumps in the star-like structure are on top of α -atom positions, while three are in the hollow sites of the honeycomb lattice. The bright shape to the right of the star structure is ascribed to imperfections of the tip. The inset in Fig. 8.11(a) shows a star-like structure imaged without tip induced asymmetry. Three very bright and three slightly darker protrusions can be identified. In Fig. 8.11(b) a number of possible 3 and 4 H atom candidate structures for the underlying H atom configuration responsible for the star-like structure are shown. These are all centered on a β carbon atom and exhibit the same C_3 symmetry as the star-triangle-like feature in the STM images.

Fig. 8.12(a)–(c) shows a series of STM images where the star like structure is imaged at low tunneling voltage resulting in a triangular appearance. As can be seen from the images all the triangles within a given image are oriented in the same direction. Observations show that generally all triangles within a given area (micro-crystallite) of the HOPG surface are oriented in the same direction. Such an aligned orientation is rather surprising considering that the star structures are observed to be centered on a carbon atom. In Fig. 8.12(d) it is sketched how for any structure with the same symmetry as the observed star structure centered on a carbon atom another one must exist pointing in the opposite orientation (rotated 60°), the only difference with respect to the original being whether it is centered on a β or an α carbon atom. Thus our observation that all the triangle structures point in the same direction is equivalent to the fact that all of them are centered on β carbon atoms which seems to imply a significant energy difference

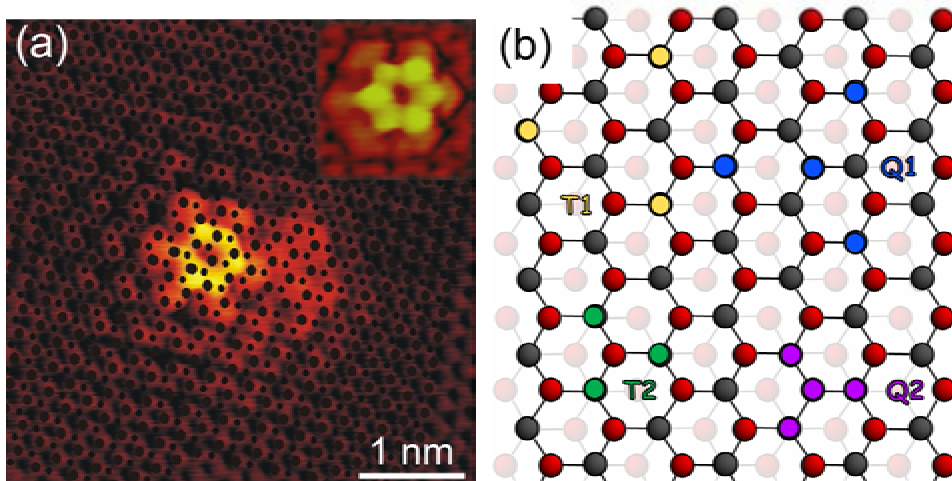


Figure 8.11: (a) STM image of a star-like structure with superimposed model graphite lattice. Imaging parameters: $I_t = -0.53$ nA, $V_t = -1051$ mV. The bright shape to the right of the star structure is ascribed to imperfections of the tip. The inset shows a star-like structure imaged without tip induced asymmetry. Imaging parameters: $I_t = -0.79$ nA, $V_t = -743$ mV. (b) 3 and 4H atom structures exhibiting the same symmetry as the observed star-like structure. H atom positions marked as: trimer structure: T1: yellow dots, T2: green dots, Quartets: Q1: blue dots, Q2: purple dots, α carbon atom are grey dots, while β carbon atoms are red.

between similar structures centered on α and β atoms. This observation is in contradiction to previous theoretical results according to which the adsorption energy for individual H-adatoms is only weakly dependent on the type of surface carbon atom onto which it is adsorbed [240]. However, calculated binding energy differences between hydrogen atoms on α and β sites of 10% have been reported in one instance [273]. One alternative explanation might be that the structures contain sub-surface hydrogen atoms. A larger binding energy difference between α and β sites is expected if the hydrogen atom is adsorbed sub-surface [274]. However, large barriers exist for an incoming hydrogen atom to go sub-surface and be intercalated between the graphite layers [275] making this explanation dubious. Previous studies of H atom dimer structures on graphite have shown that it is not the binding energies but rather the kinetics of the sticking, diffusion and recombination processes which determine what structures are formed and how stable these structures are [260,269]. Whether a more subtle difference between the α and β sites exist in the hydrogen adsorbate structure formation dynamics or in the kinetics of the hydrogen atom recombination and desorption remains unclear. It has also been suggested that the star-triangle-like structure could be a result of a hydrogen induced defect. Finally, an alternative explanation could be that the observed long range disturbance which the hydrogen adsorbates cause in the electronic density of states of the carbon lattice results in a real or apparent alignment of the star-triangle-like structures within a given area.

8.3.3 Conclusion

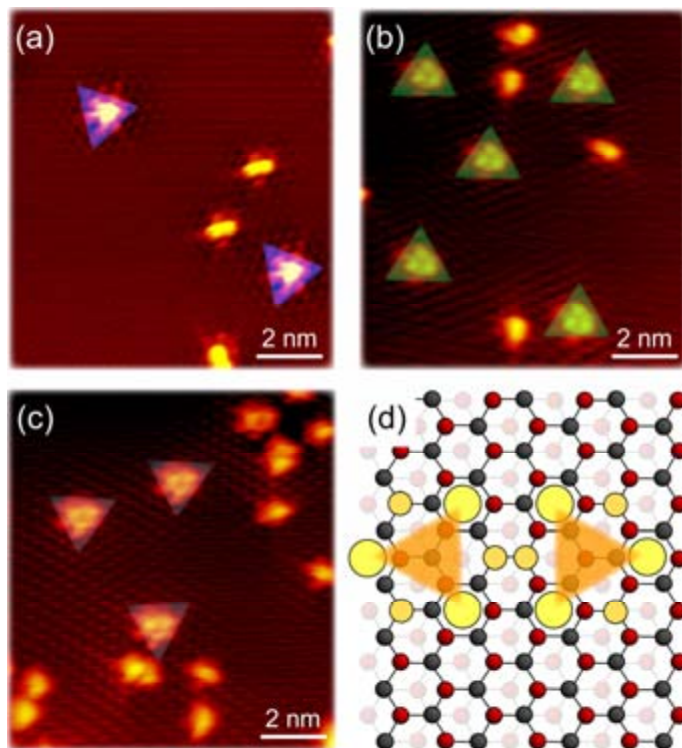


Figure 8.12: (a)–(c) STM images of different regions (different micro-crystallites) on the graphite surface recorded in an imaging mode where the star-structures appear triangular. All star structures, e.g. all the triangles, in a given region are seen to have the same orientation. For clarification highlighted triangles have been superimposed. Imaging parameters: (a) $I_t = -0.49$ nA, $V_t = -1051$ mV, (b) $I_t = -0.19$ nA, $V_t = -743$ mV, (c) $I_t = -0.14$ nA, $V_t = -743$ mV. (d) Schematic drawing of the two orientations expected for a triangular structure centered on either an α (grey) or a β (red) carbon atom.

In conclusion, we have observed that hydrogen atoms at high coverage forms two types of meta-stable structures with increased stability, namely dimer like structures, which were also observed at low coverage, and star/triangular-like structures, which are unique for the high coverage regime. These structures are stable against anneals up to 525 K and are expected to be responsible for the high temperature peak observed in TPD measurements of molecular hydrogen formation by atomic hydrogen recombination on the graphite surface. The star/triangular-like structures are observed to be centered on carbon atoms on the surface and are imaged either as stars or triangles depending on the imaging parameters. Imaged as triangles they are observed to exhibit the same orientation within a given micro-crystallite on the surface. The origin of this orientation and the exact hydrogen adsorbate structure which gives rise to the imaged star/triangular structure is not yet determined, thereby underlining the fact that we still do not fully understand the complex dynamics which underlie the H-graphite interaction.

CHAPTER 9

Summary and outlook

Molecules on surfaces play a fundamental role in diverse fields such as organic thin film growth, organic semiconductors, biomaterials interfaces, nano-mechanical biosensors, molecular electronics, nano-patterning, and so on. In all these fields the fundamental understanding of the delicate balance between intermolecular interactions and molecule-substrate interactions is of utmost relevance to be able to steer the above mentioned processes as desired. In this thesis a number of adsorption studies of organic molecules and H atoms on solid surfaces have been studied at the atomic scale by means of scanning tunneling microscopy (STM). The main systems studied in this thesis include biologically relevant molecules on Au(111) (chapter 3), small organic molecules and supramolecular complex on Au(111), Ag(110), and Cu(110) (chapter 4,5,6,7), and H atoms on HOPG (chapter 8).

In chapter 3 a systematic study of DNA bases and derivatives was presented. The main findings were that (i) two adenine (A) self-assembled 2D islands with well-ordered structures are experimentally observed by STM to co-exist on the Au(111) surface. Extensive calculations of A molecule and its pairs with the Au(111) surface show that the interaction of one or two molecules with the Au(111) is very weak. Moreover, the effect of the surface on the hydrogen bonding between molecules is also very small. However, we observed small redistribution of the electron density between the A molecules and the Au surface, which indicates that there may be some lateral registry with the underlying surface. This interaction perturbs the much stronger inter-molecular interactions binding the molecules together in the monolayer. (ii) The adsorption of thymine (T) molecules on the Au(111) surface showed that the multiple functionalities with which T molecules are endowed allow them to interact through both strong multiple hydrogen bonds and weak vdW interactions. This leads to a kinetically hierarchical self-assembly in which 1D T filaments stabilized by hydrogen bonds are formed initially at low coverages, after which the filaments, steered by the vdW interactions, self-assemble laterally into 2D T islands. Furthermore, by STM manipulation we can directly probe the hierarchy of bond-strengths involved in the self-assembled nanostructures. This is done by probing the different resistances that the bonds between neighboring molecules and supramolecules oppose to breaking under STM manipulation. The method of selective intermolecular STM-induced bond breaking can offer unique possibilities to determine

the position of the weaker bonds within a self-assembled organic monolayer, and can thus be used to help to identify particular features of the molecular architecture in the observed STM images. (iii) The adsorption of guanine (G) molecules on Au(111) demonstrated that the surface-induced chirality of the prochiral G molecule can be generated and amplified by room-temperature adsorption. Enantiomerically pure and racemic 2D well-ordered phases were observed. The latter was obtained by annealing to 400 K and subsequent cooling to 100 K prior to the STM analysis. The results may be of particular interest regarding the creation of functionalized surfaces for biosensor and heterocatalysis applications, as well as for specific applications in drug design based on the biologically relevant G quartets. (iv) The adsorption of cytosine (C) molecules on Au(111) resulted in a disordered filamentary structure. In spite of the lack of periodicity in the random C network, we have revealed that only a few elementary structural motifs exist through which C molecules bind to each other, and yet very complex structures can be formed from these structural building blocks. The present cytosine model system is kinetically trapped in a disordered state, similar to a glass trapped in the amorphous state, since it would need to overcome prohibitively large energy barriers to move away from it. The results presented here may reveal an interesting route for studying the structure of organic glasses, by performing a systematic search of particularly stable motifs and their possible interconnections. (v) Co-adsorption of G+C and A+C showed that the recognition between complementary NA base molecules adsorbed on solid surfaces is indeed feasible, and that the relatively small energy difference between A-C and G-C pairs allows us to choose a temperature range in which C binds preferentially to its complementary partner G and not to the non-complementary partner A. This recognition is aided by the balance between molecule-molecule interactions and the constraints to 3D molecular motion imposed by the surface, which restricts molecules mobility (both translational and rotational) to the 2D above-the-surface phase space. (vi) Co-adsorption of G+K⁺ revealed that, for the first time, the biologically relevant K⁺-embedded G-quartet metallosupramolecular network was observed on the surface in real space. Different metallosupramolecular nanoporous networks, which are dependent on the K⁺ ratio, are formed with various cavities in size and shape. These networks are found to be a result of balancing between hydrogen bonding and metal-to-ligand interaction. The current work might provide new insight into the G-quadruplex structure in biological community and thus into anti-cancer drug design. (vii) Adsorption of DNA base derivatives revealed dramatic changes of the self-assembled nanostructures formed on the Au(111) surface as compared with the original bases. Co-deposition of C_derivative and G_derivative resulted in an unexpected honeycomb network, which could provide useful information on the studies of molecular recognition between complementary base pairs.

In chapter 4 the so-called rosette system was studied. The main findings can be singled out as (i) we have systematically compared adsorption structures formed from a class of compounds that all display the same type of strong hydrogen bonding groups. The observed structures all appear to be dominated by the anticipated hydrogen-bonding interactions, but we surprisingly find that subtle changes to a side-group not directly involved in the H-bonding itself has a pronounced influence on the formed structures. This highlights the importance of obtaining an improved fundamental understanding of the interactional hierarchy that underlies the formation of well-defined nanostructures on surfaces and may guide future efforts to fine-tune intermolecular interactions to create desired self-assembled nanostructures. (ii) We have investigated adsorption and co-adsorption structures formed from CYA and M molecules at Au(111) surface. In

addition to the CYA_1M_1 structure found upon simultaneous deposition, our STM measurements show the existence of a novel CYA_1M_3 network upon sequential deposition of CYA after M and another novel CYA_3M_1 network, which is also found upon simultaneous codeposition. Theoretical modeling by the SCC-DFTB method explains the stability of the different observed networks and provides a detailed insight into the intermolecular interactions underlying their formation. By quantifying the hierarchy of homo- and heteromolecular interaction strengths, we have gained insight that can guide future efforts toward using this important complementary hydrogen-bonding motif in the synthesis of self-assembled surface nanostructures. (iii) By means of STM we showed that the stability against fragmentation of a large organic compound sublimated onto the Au(111) surface under UHV conditions can be significantly enhanced by coordinating it to gold atoms prior to deposition. The described results suggested a new route towards self-assembly of molecular nanoscale structures from large organic building blocks and warrants further experimental or theoretical studies into the origin and generality of this unanticipated stabilizing effect.

In chapter 5 we have studied Lander-type molecules and the main findings show that (i) by lateral STM manipulation various contact configurations of the DAT molecule at the step edge of Cu(110) are engineered in a controlled manner, through rotation, lateral translation, and hurdle over the step edge. (ii) Coadsorption of the triple components of DAT molecules together with PTCDI molecules and Ni atoms shows that the DAT molecules can be caged and aligned by PTCDI-Ni matrix.

In chapter 6 we have shown that even on defect-afflicted surfaces self-assembly by hydrogen bonding can be used to build 1D mesoscale structures from single molecular building blocks. The theoretical analysis shows that the primary key factor is a robust hydrogen bond. But self-assembly across step edges also depends crucially on the directionality mediated by the substrate, since the 1D chains would not cross the step edges, if there existed adsorbate geometries that are rotated away from the close-packed rows with energies not much smaller than those of the most stable terrace geometries. Also, the energy loss inflicted by the bending of the molecules at the step edges is smaller than that for the alternative geometry of open 1D chain ends. Thus, the flexibility of the molecular structure is an additional important ingredient needed for achieving the observed monatomic step tolerance.

In chapter 7 we have characterized the adsorption of iridium(III) phosphorescent emitter molecules on a partly oxidized Cu(110) surface. In doing so we provide convincing evidence that 50% of the emitters have dissociated upon adsorption at the substrate. Our findings suggest that the decrease in the lifetime of OLEDs, which are manufactured by vacuum vaporization technique, is due to the dissociation of emitter molecules present in the device. Therefore, to enhance the lifetime of OLEDs, careful design and development of more robust phosphorescent complexes are required.

In chapter 8 we have investigated H atoms on HOPG surface, which revealed that (i) based on STM experiments and DFT calculations we have identified the recombination mechanisms of H atoms on the graphite surface and shown that direct recombination takes place out of only one of the two observed dimer states. The presented results explain the structure observed in TPD spectra of molecular hydrogen desorption from graphite. Furthermore, the determined recombination mechanism and diffusion and recombination barriers provide direct input to models of interstellar hydrogen formation on graphitic interstellar dust grain surfaces. (ii) New mechanism of H atoms clustering on the surface has been identified showing that once a first H atom is adsorbed on the surface, the adsorption barriers for additional H atoms are reduced very much or even

vanish, and larger clusters can form. This mechanism enables the buildup of non-negligible H atom coverages from which molecular hydrogen formation may occur either via recombinative desorption or via Eley-Rideal abstraction. Hence, the presented results reveal a new mechanism for adsorbate cluster formation on surfaces via preferential sticking and contribute to our understanding of interstellar hydrogen formation. (iii) We have observed that hydrogen atoms at high coverage forms two types of meta-stable structures with increased stability, namely dimer like structures, which were also observed at low coverage, and star/triangular-like structures, which are unique for the high coverage regime. These structures are stable against anneals up to 525 K and are expected to be responsible for the high temperature peak observed in TPD measurements of molecular hydrogen formation by atomic hydrogen recombination on the graphite surface. The star/triangular-like structures are observed to be centered on carbon atoms on the surface and are imaged either as stars or triangles depending on the imaging parameters. Imaged as triangles they are observed to exhibit the same orientation within a given micro-crystallite on the surface. The origin of this orientation and the exact hydrogen adsorbate structure which gives rise to the imaged star/triangular structure is not yet determined. This underlines the fact that we still do not fully understand the complex dynamics which underlie the H-graphite interaction.

Bibliography

- [1] J. V. Barth, G. Costantini, K. Kern, *Nature* 437, 671 (2005).
- [2] T. Yokoyama, S. Yokoyama, T. Kamikado, Y. Okuno, S. Mashiko, *Nature* 413, 619 (2001).
- [3] L. A. Bumm et al, *Science* 271, 1705 (1996).
- [4] L. J. Prins, F. De Jong, P. Timmerman, D. N. Reinhoudt, *Nature* 408, 181 (2000).
- [5] J. V. Barth et al, *J. Am. Chem. Soc.* 124, 7991 (2002).
- [6] T. A. Jung, R. R. Schlittler, J. K. Gimzewski, *Nature* 386, 696 (1997).
- [7] Q. Chen, N. V. Richardson, *Nat. Mater.* 2, 324 (2003).
- [8] A. Schiffrin et al, *PNAS* 104, 5279 (2003).
- [9] M. E. Anderson et al, *Adv. Mater.* 18, 3258 (2006).
- [10] R. K. Smith, P. A. Lewis, P. S. Weiss, *Prog. Surf. Sci.* 75, 1 (2004).
- [11] J. Weckesser, A. De Vita, J. V. Barth, C. Cai, K. Kern, *Phys. Rev. Lett.* 87, 096101 (2001).
- [12] J. Weckesser, J. V. Barth, C. Z. Cai, B. Muller, K. Kern, *Surf. Sci.* 431, 168 (1999).
- [13] J. V. Barth et al, *Angew. Chem.-Int. Ed.* 39, 1230 (2000).
- [14] J. I. Pascual et al, *J. Chem. Phys.* 120, 11367 (2004).
- [15] M. De Wild et al, *Chemphyschem* 3, 881 (2002).
- [16] H. J. Van Manen et al, *Nano Lett.* 4, 441 (2004).
- [17] A. G. Bielejewska et al, *J. Am. Chem. Soc.* 123, 7518 (2001).
- [18] H. Schonherr, M. Crego-Calama, G. J. Vancso, D. N. Reinhoudt, *Adv. Mater.* 16, 1416 (2004).
- [19] M. Arduini et al, *J. Org. Chem.* 68, 1097 (2003).
- [20] L. J. Prins et al, *J. Org. Chem.* 67, 4808 (2002).
- [21] M. Schunack et al, *Phys. Rev. Lett.* 86, 456 (2001).
- [22] M. Schunack, E. Laegsgaard, I. Stensgaard, F. Besenbacher, *J. Chem. Phys.* 117, 8493 (2002).
- [23] F. Rosei et al, *Science* 296, 328 (2002).
- [24] R. Otero et al, *Angew. Chem.-Int. Ed.* 43, 2092 (2004).
- [25] R. Otero et al, *Nano Lett.* 4, 75 (2004).
- [26] A. Kuhnle, T. R. Linderoth, M. Schunack, F. Besenbacher, *Langmuir* 22, 2156 (2006).

- [27] A. Kuhnle, T. R. Linderoth, F. Besenbacher, *J. Am. Chem. Soc.* 128, 1076 (2006).
- [28] A. Kuhnle et al, *Phys. Rev. Lett.* 93, 086101 (2004).
- [29] A. Kuhnle, T. R. Linderoth, F. Besenbacher, *J. Am. Chem. Soc.* 125, 14680 (2003).
- [30] A. Kuhnle, T. R. Linderoth, B. Hammer, F. Besenbacher, *Nature* 415, 891 (2002).
- [31] R. Otero et al, *Nat. Mater.* 3, 779 (2004).
- [32] L. J. Wan, *Acc. Chem. Res.* 39, 334 (2006).
- [33] S. De Feyter, F. C. De Schryver, *Chem. Soc. Rev* 32, 139 (2003).
- [34] Z. Ma et al, *ACS Nano* 1, 160 (2007).
- [35] W. Xu et al, *J. Am. Chem. Soc.* 129, 10624 (2007).
- [36] H. Gersen et al, *Appl. Phys. Lett.* 89, 264102 (2006).
- [37] Y. Shirai, A. J. Osgood, Y. Zhao, K. F. Kelly, J. M. Tour, *Nano Lett.* 5, 2330 (2005).
- [38] G. Binning, H. Rohrer, C. Gerber, E. Weibel, *Phys. Rev. Lett.* 49, 57 (1982).
- [39] J. Tersoff, D. R. Hamann, *Phys. Rev. Lett.* 50, 1998 (1983).
- [40] J. Bardeen, *Phys. Rev. Lett.* 6, 57 (1961).
- [41] J. Tersoff, D. R. Hamann, *Phys. Rev. B* 31, 805 (1985).
- [42] N. D. Lang, *Phys. Rev. Lett.* 55, 230 (1985).
- [43] N. D. Lang, *Phys. Rev. Lett.* 56, 1164 (1986).
- [44] E. Laegsgaard, F. Besenbacher, K. Mortensen, I. Stensgaard, *J. Microscop.* 152, 663 (1988).
- [45] P. Hohenberg, W. Kohn, *Phys. Rev. B* 136, 864 (1964).
- [46] W. Kohn, L. J. Sham, *Phys. Rev.* 140, 1133 (1965).
- [47] L. Petersen et al, *Rev. Sci. Instrum.* 72, 1438 (2001).
- [48] E. Laegsgaard et al, *Rev. Sci. Instrum.* 72, 3537 (2001).
- [49] J. V. Barth, *Annu. Rev. Phys. Rev.* 58, 375 (2007).
- [50] D. L. Keeling et al, *Nano. Lett.* 3, 9 (2003).
- [51] J. A. Theobald et al, *Nature* 424, 1029 (2003).
- [52] S. De Feyter et al, *Nano. Lett.* 5, 77 (2005).
- [53] R. E. A. Kelly, L. N. Kantorovich, *J. Mater. Chem.* 16, 1894 (2006).
- [54] W. M. Heckl et al, *Proc. Nat. Acad. Sci.* 88, 8003 (1991).
- [55] T. Kawai, H. Tanaka, T. Nakagawa, *Surf. Sci.* 386, 124 (1997).
- [56] M. Furukawa, H. Tanaka, T. Kawai, *Surf. Sci.* 392, L33 (1997).
- [57] M. Furukawa, H. Tanaka, T. Kawai, *Surf. Sci.* 445, 1 (2000).
- [58] M. Furukawa, H. Tanaka, T. Kawai, *J. Chem. Phys.* 115, 3419 (2001).
- [59] S. J. Sowerby, W. M. Heckl, G. B. Petersen, *J. Mol. Evol.* 43, 419 (1996).
- [60] S. J. Sowerby, M. Edelwirth, W. M. Heckl, *J. Phys. Chem. B* 102, 5914 (1998).
- [61] M. Edelwirth, J. Freund, S. J. Sowerby, W. M. Heckl, *Surf. Sci.* 417, 201 (1998).
- [62] S. J. Sowerby, M. Edelwirth, M. Reiter, W. M. Heckl, *Langmuir* 14, 5195 (1998).

- [63] J. E. Freund, M. Edelwirth, P. Krobel, W. M. Heckl. *Phys. Rev. B* 55, 5394 (1997).
- [64] L. M. A. Perdigão et al, *Phys. Rev. B* 73, 195423 (2006).
- [65] Q. Chen, D. J. Frankel, N. V. Richardson, *Langmuir* 18, 3219 (2002).
- [66] R. Otero et al, *Angew. Chem. Int. Ed.* 44, 2270 (2005).
- [67] W. Mamdouh et al, *J. Phys. Chem. B* 111, 12048 (2007).
- [68] W. Xu et al, *Small* 3, 2011 (2007).
- [69] R. Otero et al, *Science* 319, 312 (2008).
- [70] W. Mamdouh et al, *J. Am. Chem. Soc.* 130, 695 (2008).
- [71] S. J. Sowerby, W. M. Heckl, *Orig. Life and Evol. Biosp.* 28, 283 (1998).
- [72] S. Piana, A. Bilic, *J. Phys. Chem. B* 110, 23467 (2006).
- [73] F. Ortmann, W. G. Schmidt, F. Bechstedt, *Phys. Rev. Lett.* 95, 186101 (2005).
- [74] M. Preuss, W. G. Schmidt, F. Bechstedt, *Phys. Rev. Lett.* 94, 236102 (2005).
- [75] To be detailed elsewhere.
- [76] P. Ordejon, E. Artacho, J. M. Soler, *Phys. Rev. B* 53, 10441 (1996).
- [77] J. M. Soler et al, *J. Phys.-Condens. Mat.* 14, 2745 (2002).
- [78] S. F. Boys, F. Bernardi, *Mol. Phys.* 19, 553 (1970).
- [79] R. E. A. Kelly, Y. J. Lee, L. N. Kantorovich. *J. Phys. Chem. B* 109, 11933 (2005).
- [80] R. E. A. Kelly, L. N. Kantorovich. *J. Phys. Chem. B* 110, 2249 (2006).
- [81] R. E. A. Kelly, Y. J. Lee, L. N. Kantorovich. *J. Phys. Chem. B* 109, 22045 (2005).
- [82] R. E. A. Kelly, L. N. Kantorovich. *J. Phys. Chem. C* 111, 3883 (2007).
- [83] J. Sponer, P. Jurecka, P. Hobza. *J. Am. Chem. Soc.* 126, 10142 (2005).
- [84] P. Jurecka, J. Sponer, J. Cerny, P. Hobza. *Phys. Chem. Chem. Phys.* 8, 1985 (2006).
- [85] P. Hobza, J. Sponer. *Chem. Rev.* 99, 3247 (1999).
- [86] J. Sponer, J. Leszczynski, P. Hobza. *J. Phys. Chem.* 100, 1965 (1996).
- [87] A. P. M. Camargo, H. Baumgartel, C. Donner, *Phys. Chem. Comm.* 5, 151 (2002).
- [88] R. E. A. Kelly, L. N. Kantorovich, *Surf. Sci.* 589, 139 (2005).
- [89] K. Shinoda et al, *Surf. Sci.* 556, 109 (2004).
- [90] C. D. Dimitrakopoulos, P. R. L. Malenfant, *Adv. Mater.* 14, 99 (2002).
- [91] S. E. Shaheen et al, *Appl. Phys. Lett.* 78, 841 (2001).
- [92] J. Fritz et al, *Science* 288, 316 (2000).
- [93] Q. M. Xu et al, *Langmuir* 17, 6203 (2001).
- [94] Z. T. Deng et al, *Phys. Rev. Lett.* 96, 156102 (2006).
- [95] J. Kuntze et al, *Phys. Rev. B* 65, 233405 (2002).
- [96] W. Xu et al, *Small* 3, 854 (2007).
- [97] R. Otero, F. Rosei, F. Besenbacher, *Annu. Rev. Phys. Chem.* 57, 497 (2006).
- [98] P. R. Tulip, S. J. Clark, *Phys. Rev. B* 71, 195117 (2005).

- [99] D. R. Allan et al, *Phys. Rev. B* 58, 11809 (1998).
- [100] S. J. Sowerby, G. B. Petersen, *J. Electroanal. Chem.* 433, 85 (1997).
- [101] I. W. Lyo, P. Avouris, *J. Chem. Phys.* 93, 4479 (1990).
- [102] B. C. Stipe et al, *Phys. Rev. Lett.* 78, 4410 (1997).
- [103] R. S. Becker, G. S. Higashi, Y. J. Chabal, A. J. Becker, *Phys. Rev. Lett.* 65, 1917 (1990).
- [104] E. Winfree, F. R. Liu, L. A. Wenzler, N. C. Seeman, *Nature* 394, 539 (1998).
- [105] H. Yan et al, *Science* 301, 1882 (2003).
- [106] A. Chworos et al, *Science* 306, 2068 (2004).
- [107] W. M. Heckl, *Adv. Eng. Mater.* 6, 843 (2004).
- [108] A. Schiffrin et al, *PNAS* 104, 5279 (2007).
- [109] G. P. Lopinski, D. J. Moffatt, D. D. Wayner, R. A. Wolkow, *Nature* 392, 909 (1998).
- [110] M. O. Lorenzo, C. J. Baddeley, C. Muryn, R. Raval, *Nature* 404, 376 (2000).
- [111] S. Weigelt et al, *Nat. Mater.* 5, 112 (2006).
- [112] F. Vidal et al, *J. Am. Chem. Soc.* 127, 10101 (2005).
- [113] J. V. Barth, H. Brune, G. Ertl, R. J. Behm, *Phys. Rev. B* 42, 9307 (1990).
- [114] M. Mons et al, *J. Phys. Chem. A* 106, 5088 (2002).
- [115] M. Y. Choi, R. E. Miller, *J. Am. Chem. Soc.* 128, 7320 (2006).
- [116] C. Colominas, F. J. Luque, M. Orozco, *J. Am. Chem. Soc.* 118, 6811 (1996).
- [117] J. L. Mergny, C. Helene, *Nat. Med.* 4, 1366 (1998).
- [118] R. Zallen, *The Physics of Amorphous Solids* (Wiley-VCH, Weinheim, ed. 1, 2004).
- [119] S. C. Moss, J. F. Graczyk, *Phys. Rev. Lett.* 23, 1167 (1969).
- [120] A. van Blaaderen, P. Wiltzius, *Science* 270, 1177 (1995).
- [121] E. R. Weeks, J. C. Crocker, A. C. Levitt, A. Schofield, D. A. Weitz, *Science* 287, 627 (2000).
- [122] F. Rosei et al., *Prog. Surf. Sci.* 71, 95 (2003).
- [123] M. Schunack et al., *Phys. Rev. Lett.* 86, 456 (2001).
- [124] M. Schunack et al., *Phys. Rev. Lett.* 88, 156102 (2002).
- [125] N. J. Tao, J. A. DeRose, S. M. Lindsay, *J. Phys. Chem.* 97, 910 (1993).
- [126] M. A. Ramos et al., *Phys. Rev. Lett.* 78, 82 (1997).
- [127] L. E. Orgel, *Nature* 358, 203 (1992).
- [128] J. Sutherland, J. Whitfield, *Tetrahedron* 53, 11493 (1997).
- [129] J. D. Watson, F. H. C. Crick, *Nature* 171, 737 (1953).
- [130] E. T. Kool, *Annu. Rev. Biophys. Biomol. Struct.* 30, 1 (2001).
- [131] D. H. Turner et al, *J. Am. Chem. Soc.* 109, 3783 (1987).
- [132] Th. Henning, F. Salama, *Science* 282, 2204 (1998).
- [133] R. E. A. Kelly et al, To be submitted.
- [134] M. Edelwirth et al, *Surface Science* 417, 201 (1998).

- [135] C. F. Guerra et al, *Chem. Eur. J.* 5, 3581 (1999).
- [136] S. Xu et al, *Nano Lett.* 6, 1434 (2006).
- [137] E. Nir, K. Kleiner, M. S. de Vries, *Nature* 408, 949 (2000).
- [138] L. H. Hurley, *Nat. Rev. Cancer* 2, 188 (2002).
- [139] S. Neidle, G. Parkinson, *Nat. Rev. Drug Discov.* 1, 383 (2002).
- [140] J. T. Davis, *Angew. Chem. Int. Ed.* 43, 668 (2004).
- [141] A. T. Phan, K. N. Luu, D. J. Patel, *Nucl. Acids Res.* 34, 5715 (2006).
- [142] G. N. Parkinson, M. P. H. Lee, S. Neidle, *Nature* 417, 876 (2002).
- [143] J. Y. Lee, B. Okumus, D. S. Kim, T. J. Ha, *PNAS* 102, 18938 (2005).
- [144] W. Eimer, T. Dorfmueller, *J. Phys. Chem.* 96, 6790 (1992).
- [145] A. A. Lipanov, J. Quintana, R. E. Dickerson, *J. Biomol. Struct. Dyn.* 8, 483 (1990).
- [146] K. J. Koch, T. Aggerholm, S. C. Nanita, R. G. Cooks, *J. Mass Spectrom.* 37, 676 (2002).
- [147] G. Wu, A. Wong, *Chem. Commun.*, 2658 (2001).
- [148] T. J. Pinnavaia et al, *J. Am. Chem. Soc.* 100, 3625 (1978).
- [149] S. L. Forman et al, *J. Am. Chem. Soc.* 122, 4060 (2000).
- [150] F. W. Kitch, J. C. Fettinger, J. T. Davis, *Org. Lett.* 2, 3277 (2000).
- [151] X. Shi, J. C. Fettinger, J. T. Davis, *Angew. Chem. Int. Ed.* 40, 2827 (2001).
- [152] X. D. Shi, J. C. Fettinger, J. T. Davis, *J. Am. Chem. Soc.* 123, 6738 (2001).
- [153] A. Wong et al, *J. Am. Chem. Soc.* 124, 742 (2002).
- [154] G. Pawin, K. L. Wong, K. Y. Kwon, L. Bartels, *Science* 313, 961 (2006).
- [155] S. Stepanow, N. Lin, J. V. Barth, K. Kern, *J. Phys. Chem. B* 110, 23472 (2006).
- [156] M. A. Lingenfelder et al, *Chem. Eur. J.* 10, 1913 (2004).
- [157] S. Stepanow et al, *Nat. Mater.* 3, 229 (2004).
- [158] A. Dmitriev et al, *Angew. Chem. Int. Ed.* 42, 2670 (2003).
- [159] S. Stepanow et al, *Angew. Chem. Int. Ed.* 46, 710 (2007).
- [160] K. Tahara et al, *J. Am. Chem. Soc.* 128, 16613 (2006).
- [161] S. Furukawa et al, *J. Am. Chem. Soc.* 128, 3502 (2006).
- [162] L. M. Ying et al, *PNAS* 100, 14629 (2003).
- [163] Y. Ke, S. Lindsay, Y. Chang, Y. Liu, H. Yan, *Science* 319, 180 (2008).
- [164] C. J. Baddeley, *Top. Catal.* 25, 17 (2003).
- [165] S. Lei et al, *Chem. Commun.* 703 (2008).
- [166] X. H. Kong et al, *J. Phys. Chem. C* 111, 17382 (2007).
- [167] K. G. Nath et al, *J. Am. Chem. Soc.* 128, 4212 (2006).
- [168] M. Schöck et al, *J. Phys. Chem. B* 110, 12835 (2006).
- [169] N. Wintjes et al, *Angew. Chem. Int. Ed.* 46, 4089 (2007).
- [170] H. Spillmann et al, *Adv. Mater.* 18, 275 (2006).

- [171] S. Vázquez-Campos et al, *Langmuir* 23, 10294 (2007).
- [172] J.-M. Lehn, *Science* 295, 2401 (2002).
- [173] D. N. Reinhoudt, M. Crego-Calama, *Science* 295, 2403 (2002).
- [174] D. C. Sherrington, K. A. Taskinen, *Chem. Soc. Rev.* 30, 83 (2001).
- [175] T. Steiner, *Angew. Chem. Int. Ed.* 41, 48 (2002).
- [176] J. A. Theobald et al, *Langmuir* 21, 2038 (2005).
- [177] J. C. Swarbrick et al, *J. Phys. Chem. B* 110, 6113 (2006).
- [178] M. Stçhr et al, *Angew. Chem. Int. Ed.* 44, 7394 (2005).
- [179] C. T. Seto, G. M. Whitesides, *J. Am. Chem. Soc.* 112, 6409 (1990).
- [180] J. A. Zerkowski, C. T. Seto, G. M. Whitesides, *J. Am. Chem. Soc.* 114, 5473 (1992).
- [181] G. M. Whitesides et al, *Acc. Chem. Res.* 28, 37 (1995).
- [182] C. Thalacker et al, *Org. Biomol. Chem.* 3, 414 (2005).
- [183] L. M. A. Perdigão, N. R. Champness, P. H. Beton, *Chem. Commun.* 538 (2006).
- [184] Y. Wang, B. Wei, Q. Wang, *J. Crystallogr. Spectrosc. Res.* 20, 79 (1990).
- [185] A. Ranganathan, V. R. Pedireddi, C. N. R. Rao, *J. Am. Chem. Soc.* 121, 1752 (1999).
- [186] S. Stepanow et al, *J. Phys. Chem. B* 108, 19392 (2004).
- [187] L. J. Prins et al, *J. Org. Chem.* 67, 4808 (2004).
- [188] C. T. Seto, G. M. Whitesides, *J. Am. Chem. Soc.* 115, 1330 (1993).
- [189] Y. Qiu, L. Gao, *Mater. Res. Bull.* 40, 794 (2005).
- [190] S. E. Grillo, H. Tang, C. Coudret, S. Gauthier, *Chem. Phys. Lett.* 355, 289 (2002).
- [191] L. Grill, I. Stass, K.-H. Rieder, F. Moresco, *Surf. Sci.* 600, L143 (2006).
- [192] J. C. Swarbrick, J. Ben Taylor, J. N. O'Shea, *Appl. Surf. Sci.* 252, 5622 (2006).
- [193] H. J. Rader et al, *Nat. Mater.* 5, 276 (2006).
- [194] L. Grill et al, *Nat. Nanotech.* 2, 95 (2007).
- [195] K. L. Wong et al, *Science* 315, 1391 (2007).
- [196] L. Gross et al, *Nat. Mater.* 4, 892 (2005).
- [197] P. Sautet, C. Joachim, *Chem. Phys. Lett.* 185, 23 (1991).
- [198] J. V. Barth et al., *Appl. Phys. A* 76, 645 (2003).
- [199] A. Schiffrin et al., *Proc. Natl. Acad. Sci.* 104, 5279 (2007).
- [200] A. Dmitriev et al., *J. Phys. Chem. B* 106, 6907 (2002).
- [201] S. Griessl et al., *Single Mol.* 3, 25 (2002).
- [202] S. De Feyter et al., *Nano Lett.* 3, 1485 (2003).
- [203] M. Lackinger et al., *J. Phys. Chem. B* 108, 13652 (2004).
- [204] S. Clair et al., *J. Phys. Chem. B* 108, 14582 (2004).
- [205] M. Lackinger et al., *Small* 1, 532 (2005).
- [206] J. C. Swarbrick et al., *J. Phys. Chem. B* 109, 12167 (2005).

- [207] M. E. Canas-Ventura et al., *Angew. Chem. Int. Ed.* 46, 1814 (2007).
- [208] B. Xu et al., *J. Am. Chem. Soc.* 128, 8493 (2006).
- [209] H. Li et al., *J. Phys. Chem. C* 111, 2102 (2007).
- [210] N. Zhu, T. Osada, T. Komeda, *Surf. Sci.* 601, 1789 (2007).
- [211] L. Patthey et al., *J. Chem. Phys.* 110, 5913 (1999).
- [212] A. Dmitriev et al., *Chem. Phys. Chem.* 7, 2197 (2006).
- [213] A. Bilic et al., *J. Chem. Theory Comput.* 2, 1093 (2006).
- [214] P. S. Bagus, K. Hermann, C. Wöll, *J. Chem. Phys.* 123, 184109 (2005).
- [215] In this calculation the DACAPO code was extended with a London-type dispersion term.
- [216] For the deprotonated and covalently bonded molecules the H atoms are assumed to end up in H₂ at 0 K.
- [217] M. Gross et al, *Nature* 405, 661 (2000).
- [218] G. Parthasarathy, J. Liu, A. R. Duggal, *Electrochem. Soc. Interface* 12, 42 (2003).
- [219] C. Adachi, M. A. Baldo, M. E. Thompson, S. R. Forrest, *J. Appl. Phys.* 90, 5048 (2001).
- [220] M. A. Baldo et al, *Appl. Phys. Lett.* 75, 4 (1999).
- [221] M. Ikai, S. Tokito, Y. Sakamoto, T. Suzuki, Y. Taga, *Appl. Phys. Lett.* 79, 156 (2001).
- [222] H. Aziz, Z. D. Popovic, N. X. Hu, A. M. Hor, G. Xu, *Science* 283, 1900 (1999).
- [223] W. Brütting, H. Riel, T. Beierlein, and W. Riess, *J. Appl. Phys.* 89, 1704 (2001).
- [224] A. Curioni, W. Andreoni, *IBM J. Res. Dev.* 45, 101 (2001).
- [225] S. F. Alvarado et al, *IBM J. Res. Dev.* 4, 89 (2001).
- [226] M. S. Xu et al, *J. Nanosci. Nanotechnol.* 2, 139 (2002).
- [227] A. Sasahara, C. L. Pang, H. Onishi, *J. Phys. Chem. B* 110, 4751 (2006).
- [228] Md. K. Nazeeruddin et al, *J. Am. Chem. Soc.* 125, 8790 (2003).
- [229] F. Jensen, F. Besenbacher, E. Laegsgaard, and I. Stensgaard, *Phys. Rev. B* 41, 10233 (1990).
- [230] P. Sautet, *Surf. Sci.* 374, 406 (1997).
- [231] S. E. Grillo, H. Tang, C. Coudret, S. Gauthier, *Chem. Phys. Lett.* 355, 289 (2002).
- [232] L. Schlapbach, A. Züttel, *Nature* 414, 353 (2001).
- [233] S. Baouche et al, (to be published).
- [234] N. Katz, I. Furman, O. Biham, V. Pironello, G. Vidali, *Astrophys. J.* 522, 305 (1999).
- [235] G. Manico, G. Raguni, V. Pironello, J. Roser, G. Vidali, *Astrophys. J.* 548, L253 (2001).
- [236] L. Hornekær, A. Baurichter, V. Petrunin, D. Field, A. C. Luntz, *Science* 302, 1943 (2003).
- [237] S. Cazaux, A. Tielens, *Astrophys. J.* 604, 222 (2004).
- [238] D. Neumann et al, *Appl. Phys. A* 55, 489 (1992).
- [239] L. Jeloica, V. Sidis, *Chem. Phys. Lett.* 300, 157 (1999).
- [240] X. Sha, B. Jackson, *Surf. Sci.* 496, 318 (2002).
- [241] T. Zecho, A. Güttler, X. Sha, B. Jackson, J. Küppers, *J. Chem. Phys.* 117, 8486 (2002).

- [242] T. Zecho et al, Chem. Phys. Lett. 366, 188 (2002).
- [243] Y. Ferro, F. Marinelli, A. Allouche, Chem. Phys. Lett. 368, 609 (2003).
- [244] Y. Miura, H. Kasai, W. Dino, H. Nakanishi, T. Sugimoto, J. Appl. Phys. 93, 3395 (2003).
- [245] P. Ruffieux et al, Phys. Rev. Lett. 84, 4910 (2000).
- [246] T. Zecho, A. Güttler, J. Küppers, Carbon 42, 609 (2004).
- [247] E. Ghio, L. Mattera, C. Salvo, F. Tommasini, U. Valbusa, J. Chem. Phys. 73, 556 (1980).
- [248] M. Durr, A. Biedermann, Z. Hu, U. Höfer, T. F. Heinz, Science 296, 1838 (2002).
- [249] C. Su et al., J. Chem. Phys. 107, 7543 (1997).
- [250] W. Widdra et al., Phys. Rev. Lett. 74, 2074 (1995).
- [251] M. G. Burton et al., Mon. Not. R. Astr. Soc. 257, 1p (1992).
- [252] D. Hollenbach, C. F. McKee, Astrophys. J. Suppl. Ser. 41, 555 (1979).
- [253] D. Hollenbach, E. E. Salpeter, Astrophys. J. 163, 155 (1971).
- [254] T. Henning, F. Salama, Science 282, 2204 (1998).
- [255] A. Rotundi et al., Astron. Astrophys. 329, 1087 (1998).
- [256] D. Hollenbach, C. F. McKee, Astrophys. J. 342, 306 (1989).
- [257] D. A. Neufeld, A. Dalgarno, Astrophys. J. 340, 869 (1989).
- [258] D. R. Flower, G. P. des Forêts, Mon. Not. R. Astr. Soc. 247, 500 (1990).
- [259] M. Elitzur, D. Hollenbach, C. F. McKee, Astrophys. J. 346, 983 (1989).
- [260] L. Hornekær et al., Phys. Rev. Lett. 96, 156104 (2006).
- [261] X. Sha, B. Jackson, and D. Lemoine, J. Chem. Phys. 116, 7158 (2002).
- [262] A. Andree, M. L. Lay, T. Zecho, and J. Küppers, Chem. Phys. Lett. 425, 99 (2006).
- [263] The reported binding energy of the ortho and next neighbor dimer states are in good agreement with earlier findings [243,244,260], while the binding energy of the para-dimer state differs from that reported in Miura et al. [244]. This difference can be ascribed to the fact that a smaller carbon unit cell was used in these calculations.
- [264] The potential energy curve shown is for adsorption of an incoming H atom with antiparallel spin to the spin of the already adsorbed H atom. In the case of parallel spin, calculations predict a small barrier to adsorption.
- [265] K. N. Allers et al., Astrophys. J. 630, 368 (2005).
- [266] S. Baouche et al, J. Chem. Phys. 125, 084712 (2006).
- [267] G. Federici et al., Nucl. Fusion 41, 1972 (2001).
- [268] A. Güttler, T. Zecho, J. Küppers, Chem. Phys. Lett. 395, 171 (2004).
- [269] L. Hornekær et al., Phys. Rev. Lett. 97, 186102 (2006).
- [270] N. Rougeau, D. Tiellet-Billy, V. Sidis, Chem. Phys. Lett. 431, 135 (2006).
- [271] A. Allouche et al, J. Chem. Phys. 123, 124701 (2005).
- [272] D. Tomanek et al, Phys. Rev. B 35, 7790 (1987).
- [273] Y. Ferro, F. Marinelli, A. Allouche, J. Chem. Phys. 116, 8124 (2002).
- [274] Z. Sljivancanin, et al., in preparation.

- [275] Y. Ferro, F. Marinelli, A. Jelea, A. Allouche, *J. Chem. Phys.* 120, 11882 (2004).
- [276] A. J. Heinrich, C. P. Lutz, J. A. Gupta, D. M. Eigler, *Science* 298, 1381 (2002).
- [277] M. F. Crommie, C. P. Lutz, D. M. Eigler, *Science* 262, 218 (1993).
- [278] H. C. Manoharan, C. P. Lutz, D. M. Eigler, *Nature* 403, 512 (2000).
- [279] S-W. Hla, K-H. Rieder, *Annu. Rev. Phys. Chem.* 54, 307 (2003).

List of publications

Papers not included in the thesis

- [I] *Supramolecular nanoporous networks formed by guanine on Au(111)*
W. Xu, H. Gersen, R. E. A. Kelly, E. Lægsgaard, I. Stensgaard, L. N. Kantorovich, F. Besenbacher, In manuscript.
- [II] *Adenine monolayers on the Au(111) surface: structure identification by STM experiment and ab initio theory*
M. Lukas, R. E. A. Kelly, L. N. Kantorovich, R. Otero, W. Xu, E. Lægsgaard, I. Stensgaard, F. Besenbacher, In manuscript.
- [III] *Molecular self-assembly on a thin insulating film*
Ch. Bombis, N. Kalashnyk, W. Xu, E. Lægsgaard, F. Besenbacher, T. R. Linderoth, In manuscript.
- [IV] *Energetics and kinetics of extended atomic hydrogen dimer configurations on the graphite(0001) surface*
E. Rauls, Z. Slijvancanin, L. Hornekaer, W. Xu, F. Besenbacher, B. Hammer, In manuscript.
- [V] *UHV-STM Studies of Lander-type molecular moulds on Au(111) and Cu(110)*
M. Yu, W. Xu, N. Kalashnyk, E. Laegsgaard, I. Stensgaard, X. Bouju, A. Gourdon, C. Joachim, F. Besenbacher, T. R. Linderoth, In preparation.
- [VI] *Photochromic oxazine on Au(111) studied by UHV-STM*
W. Xu, H. Gersen, E. Laegsgaard, I. Stensgaard, F. Besenbacher, In preparation.
- [VII] *Photochromic oxazine on Cu(110) studied by UHV-STM*
H. Gersen, W. Xu, E. Laegsgaard, I. Stensgaard, F. Besenbacher, In preparation.
- [VIII] *Studies on the interplay of adsorbate-substrate and adsorbate-adsorbate interactions in self-assembled surface nanostructures*
J. Schnadt, E. Rauls, W. Xu, R. T. Vang, J. Knudsen, Z. Li, E. Laegsgaard, B. Hammer, F. Besenbacher, In preparation.

[IX] *C₆₀ on Au(111) studied by UHV-STM*

W. Xu, Z. Sljivancanin, L. Nilsson, E. Laegsgaard, B. Hammer, L. Hornekaer, F. Besenbacher, In preparation.

[X] *Storage of D atoms on C₆₀ revealed by UHV-STM*

W. Xu, Z. Sljivancanin, L. Nilsson, E. Laegsgaard, B. Hammer, L. Hornekaer, F. Besenbacher, In preparation.

Acknowledgements

During the course of my PhD studies in the SPM group I have cooperated and interacted with a large number of people. I would like to offer my sincere thanks and acknowledgements to those people, who were involved in different projects and gave me help and advice, as the results in this thesis were not obtained by me alone. First of all, I would like to offer my sincere gratitude to my supervisor Flemming Besenbacher for giving me the opportunity to work in the SPM group and proposing the project to me. He has always been an optimistic and inspiring support, even when things were not working well. Special gratitude is also extended to Roberto Otero, Joachim Schnadt and Maya Lukas for introducing me into the STM world and for collaboration on the projects of DNA bases (chapter 3) and NDCA molecule (chapter 6). Many thanks are also due to Liv Hornekær for collaboration on the project of hydrogen on HOPG (chapter 8). Also, I am deeply indebted to Henkjan Gersen and Trolle Linderøth for the collaboration on the 'Rosette' project and OLED molecule (chapter 4 and 7). Mingdong Dong, Sailong Xu, and Socorro Vazquez-Campos are thanked deeply for numerous fruitful discussions on 'Rosette' project as well. Special thanks are also extended to Miao Yu and Nataliya Kalashnyk for the collaboration on the Pico Inside project (chapter 5).

Ross Kelly, Lev Kantorovich, Eva Rauls and Bjørk Hammer are thanked very much for theoretical calculations on the relevant projects. Mikkel Fog Jacobsen and Kurt Vesteraager Gothelf are thanked very much for collaboration on DNA base derivatives. I would like to thank Zheshen Li for providing the K source. I am grateful for Jakob Kibsgaard's nice cover for this PhD thesis. Also, I want to thank Renald Schaub, Stefan Wendt and Ivan Stensgaard for helping with the UHV Chamber. In particular I would like to thank Erik Lægsgaard for solving many technical problems with STM. Without Erik my studies would not always have gone through smoothly. In the writing stage of the thesis Liv and Trolle gave a lot of advices and suggestions so special thanks are extended to them. Marie Louise Bro Pold is deeply thanked for proofreading this thesis.

Last but not least, my scientific endeavors would not have been possible without the continuous understanding and support from my lovely wife, Huilin. In particular I am very grateful for her uncomplaining support and for always taking care of our pretty daughter by herself most of the time, to give me as much freedom as possible to devote myself to science. In the end, I would like to thank my parents for their education and encouragement throughout my life.